MEASUREMENT OF ABSOLUTE HADRONIC BRANCHING FRACTIONS OF *D* MESONS

A Dissertation

Presented to the Faculty of the Graduate School

of Cornell University

in Partial Fulfillment of the Requirements for the Degree of

Doctor of Philosophy

by

Xin Shi

August 2011

MEASUREMENT OF ABSOLUTE HADRONIC BRANCHING FRACTIONS OF D MESONS

Xin Shi, Ph.D.

Cornell University 2011

Using 818 pb^{-1} of e^+e^- collisions recorded at the $\psi(3770)$ resonance with the CLEO-c detector at CESR, we determine absolute hadronic branching fractions of charged and neutral D mesons using a double tag technique. Among measurements for three D^0 and six D^+ modes, we obtain reference branching fractions $\mathcal{B}(D^0 \to K^-\pi^+) = (3.906 \pm 0.021 \pm 0.062)\%$ and $\mathcal{B}(D^+ \to K^-\pi^+\pi^+) = (9.157 \pm 0.059 \pm 0.125)\%$, where the first uncertainty is statistical, the second is systematic errors. Using an independent determination of the integrated luminosity, we also extract the cross sections $\sigma(e^+e^- \to D^0\overline{D}^0) = (3.650 \pm 0.017 \pm 0.083)$ nb and $\sigma(e^+e^- \to D^+D^-) = (2.920 \pm 0.018 \pm 0.062)$ nb at a center of mass energy, $E_{\rm cm} = 3774 \pm 1$ MeV.

BIOGRAPHICAL SKETCH

Xin Shi was born on the 2nd of February 1979 in Linfen – the capital of a Chinese legendary ruler Yao more than 4000 years ago. He enjoyed his childhood life reading the detective stories of Sherlock Holmes and *A Hundred Thousand Whys* – a popular science series in China. He tried to understand so many "whys" by majoring in physics at Shandong University and gradually realized that to answer *a* "what" question is more challenging: "What is the world made of?".

With this question in mind, he enrolled in the Master of Science program in particle physics at Peking University in 2001. A year later, he had an opportunity to participate in an experiment at the Institute of High Energy Physics on the subject of studying charm quark – one of the fundamental building blocks of our world. It turned out that the properties of *charm* quark was so attractive that he decided to obtain a Ph.D degree in the subject at Cornell University.

The road towards the Ph.D is never straight. Originally planned for five years, he ended up with two more years due to a detour in another experiment at Large Hadron Collider (LHC). In addition, he was constantly "distracted" by activities such as teaching in outreach, playing tennis, sailing boats and learning French. For him, such "distractons" were part of the Ph.D education which builds the unique personality for a human being.

Upon getting his Ph.D, Xin is looking forward to the next stage of his life at LHC and continue to find the answer for the question "What is the world made of?". Looking back to the 10 years after his graduation from college, nothing is more appropriate to describe his feeling than the poem by Zhou Enlai:

大江歌罢掉头东，邃密群科济世穷。
面壁十年图破壁，难酬蹈海亦英雄。

To those who have contributed to CLEO in the past 30 years.

ACKNOWLEDGEMENTS

First of all, I would like to thank my advisor Jim Alexander who have been always supportive in the past 7 years for my work and beyond. I enjoyed every conversation we had and they will shape me in the rest of my life.

It is my great pleasure to work with Anders Ryd and David Cassel in the *D* Hadronic group. Without their patient guidance and constant encouragement, this analysis will never be done. I got tremendous help from Peter Onyisi and Steve Stroiney even after they had left Cornell. For this work, I benefit from conversations with Werner Sun, Brian Heltsley and David Kreinick.

My appreciation to CLEOn's who had helped me at various point: Jie Chen, Kaiyan Gao, Steve Gray, Laura Fields, Qing He, Dan Hertz, Guangshun Huang, Ji Li, Chul Su Park, Bo Xin, and Fan Yang.

Beyond my academic life, I am fortunate to have wonderful classmates in Physics department who complets my life at Cornell: Jiajun, Peijun, Sharon, John, Matt, and Nathan.

Throughout out my student life, I am always cheered by my family members: father Jimin, mother Yulan, brother Jian, and sister Zheng. A special hug to my dear wife Yunxia who had been accompanying me in the last one and a half years at Ithaca to enable me to concentrate on my dissertation.

TABLE OF CONTENTS

LIST OF TABLES

LIST OF FIGURES

CHAPTER 1

INTRODUCTION

1.1 Standard Model and Quark Mixing

What is the world made of? – This is a fundamental question that has been asked by the humankind for centuries. One of the most ambitious and most organized effort to answer this question may be represented by the research in particle physics. In its current view, all matter is made of three kinds of elementary particles: leptons, quarks, and mediators. There are six types of leptons and quarks that can be classified into three generations as illustrated in Figure 1.1. Mediators are the force carriers for the four kinds of fundamental interactions, i.e. electromagnetic (photon), weak ($Z^0, W^{\pm}$), strong (gluon), and gravity (graviton).

Currently, the most successful theory of describing these constituents of matter and of the interactions is the Standard Model (SM). It has a unified description of the weak and electromagnetic interactions and characterization of strong interaction with Quantum Chromodynamics (QCD). Since it reached full maturity with the observation of the W and Z bosons in the early 1980s [1], the verification of the Standard Model has dominated experimental particle physics for over three decades.

One of these SM tests involves the quark sector. Unlike the leptons, which couple to $W^{\pm}$ only within a particular generation, the quarks can couple to $W^{\pm}$ across genrations. There are interactions of the form $d \to uW^-$ but also relatively weaker process $s \to uW^-$. This phenomenon of quark flavor mixing was first explained by Cabibbo [2] in the 1960s by introducing a factor of $\sin\theta_C$ to the $s \to$

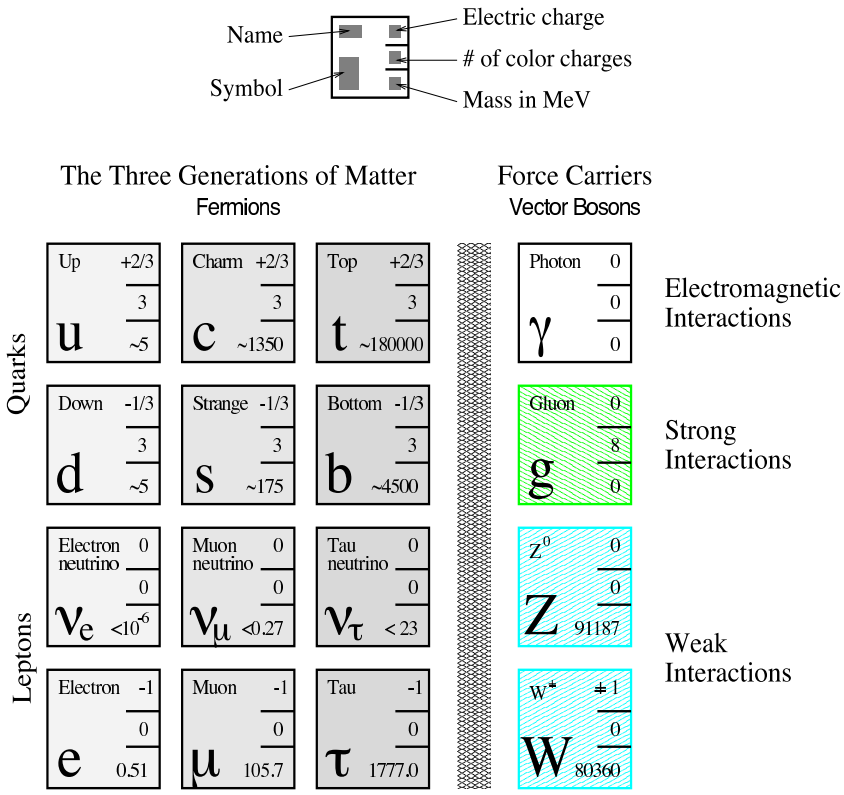

Figure 1.1: Particles in the Standard Model

uW^- process, where θ_C is the "Cabibbo angle" and determined experimentally to be around 13°.

Although the Cabbibo angle successfully explained several decay rates, it could not explain the small decay rate of $K^0(d\bar{s}) \rightarrow \mu^+\mu^-$. The theoretical prediction was proportional to "$\sin\theta_C \cos\theta_C$", but the observed rate was too small. A solution to this paradox was proposed by Glashow, Iliopoulos, and Maiani (GIM) [3]. They introduced a new fourth quark (c), which also participates in the same process, contributing a term proportional to "$-\sin\theta_C \cos\theta_C$" which cancels the corresponding diagram. The GIM mechanism was confirmed four years later by the discovery of $J/\psi(c\bar{c})$ [4, 5] in 1974. Thus, the weak interaction of the four quarks in the first two generation is described by the Cabibbo-GIM

scheme in terms of matrix form:

$$\begin{pmatrix} d' \\ s' \end{pmatrix} = \begin{pmatrix} \cos\theta_C & \sin\theta_C \\ -\sin\theta_C & \cos\theta_C \end{pmatrix} \begin{pmatrix} d \\ s \end{pmatrix}. \tag{1.1}$$

At the same time, in order to explain CP violation within the Cabibbo-GIM scheme, Kobayashi and Maskawa [6] had generalized the matrix for *three* generations of quarks:

$$\begin{pmatrix} d' \\ s' \\ b' \end{pmatrix} = \begin{pmatrix} V_{ud} & V_{us} & V_{ub} \\ V_{cd} & V_{cs} & V_{cb} \\ V_{td} & V_{ts} & V_{tb} \end{pmatrix} \begin{pmatrix} d \\ s \\ b \end{pmatrix}. \tag{1.2}$$

where V_{ub}, for example, specifies the coupling of u to $b(b \to uW^-)$, the process underlying the discovery of b quark [7] and t quark [8]. There are nine entries in the CKM matrix, but not all of them are independent. It can be reduced to a "canonical form," in which there remain just three "generalized Cabibbo angles," $(\theta_1, \theta_2, \theta_3)$ and one phase factor (δ) [9]:

$$V_{CKM} = \begin{pmatrix} c_1 & s_1c_3 & s_1s_3 \\ -s_1c_2 & c_1c_2c_3 - s_2s_3e^{i\delta} & c_1c_2s_3 + s_2c_3e^{i\delta} \\ -s_1s_2 & c_1s_2c_3 + c_2s_3e^{i\delta} & c_1s_2s_3 - c_2c_3e^{i\delta} \end{pmatrix}. \tag{1.3}$$

Here c_i stands for $\cos\theta_i$, and s_i for $\sin\theta_i$.

The CKM matrix is unitary by construction in the Standard Model, however, its elements can be only determined by experiments. Consequently, any violation of the unitarity of the CKM matrix is an indication of new physics beyond the Standard Model.

Experimental programs making measurements of many elements of the CKM matrix involve D and B meson branching fractions. For instance, the determination of the CKM matrix element V_{cb} is via the exclusive decay $B \to D^* \ell \nu$ using full D^* reconstruction which requires knowledge of the absolute D meson branching fractions [10]. Thus, precise knowledge of an absolute branching fraction scale for charm particles is very important for issues in both charm and beauty physics.

1.2 Hadronic D Meson Decays

Due to the quark confinement in strong interaction, charm quarks are are always observed bound with an antiquark to form a meson, or with two other quarks to form a baryon. D mesons are the ground state combinations of a charm quark with a lighter antiquark: $D^0(c\bar{u})$ [11] and $D^+(c\bar{d})$ [12]. The Feynman diagrams of D^0 decays to $K^-\pi^+$ and D^+ decays to $K^-\pi^+\pi^+$ is illustrated in Figures 1.2 and 1.3 respectively. As the calculation for these decay processes involve the nonperturbative QCD, theoretical predications for the related branching fractions are still not available. Therefore, the only way to obtain these decay branching fractions is through experiment.

Essentially all other D^0 and D^+ branching fractions have been determined from ratios to one of these two branching fractions $D^0 \to K^-\pi^+$ and $D^+ \to K^-\pi^+\pi^+$ [10], these two modes are also called "reference" modes. Previously, both CLEO [13] and ALEPH [14] have measured the $D^0 \to K^-\pi^+$ branching fraction with fractional error above 3.6%. For the $D^+ \to K^-\pi^+\pi^+$ channel, the measurements from CLEO [15] and Mark III [16] gave with even larger fractional error – 10.8%

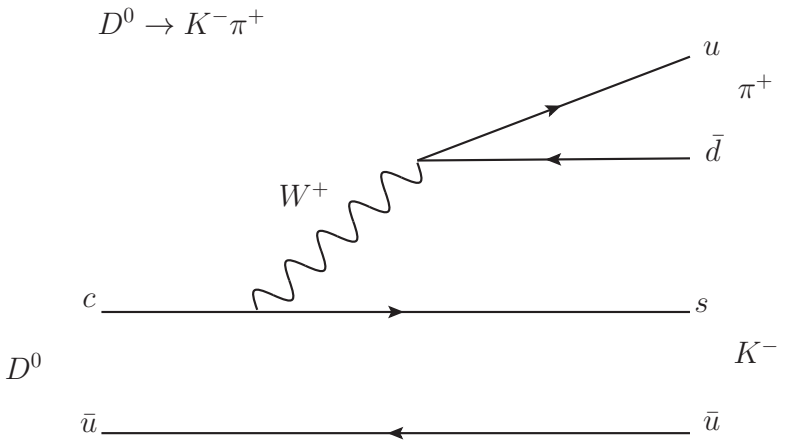

Figure 1.2: Feynman diagram for the D^0 decays to $K^-\pi^+$.

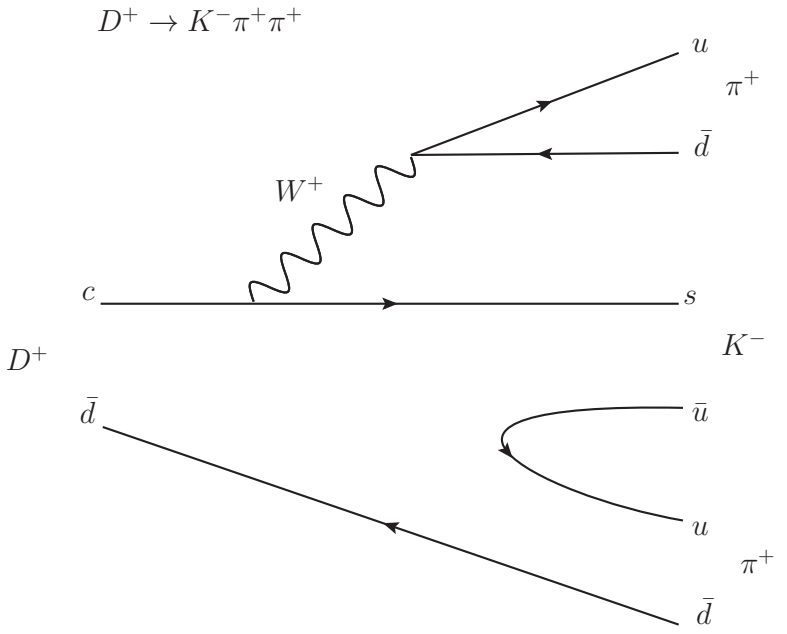

Figure 1.3: Feynman diagram for the D^+ decays to $K^-\pi^+\pi^+$.

and 14.9% respectively.

At CLEO-c, we aim at measuring the absolute D meson branching fractions listed in Table 1.1 including the two "reference" modes. Our goal is to reach the 1-2% level of precision.

Table 1.1: Modes considered in this analysis.

Mode
$D^0 \to K^-\pi^+$
$D^0 \to K^-\pi^+\pi^0$
$D^0 \to K^-\pi^+\pi^+\pi^-$
$D^+ \to K^-\pi^+\pi^+$
$D^+ \to K^-\pi^+\pi^+\pi^0$
$D^+ \to K^0_S\,\pi^+$, $K_S \to \pi^+\pi^-$
$D^+ \to K^0_S\,\pi^+\pi^0$, $K_S \to \pi^+\pi^-$
$D^+ \to K^0_S\,\pi^+\pi^+\pi^-$, $K_S \to \pi^+\pi^-$
$D^+ \to K^+K^-\pi^+$

1.3 Measurement Techniques

To measure these D branching fractions, we employ a "double tagging" technique pioneered by the MARK III Collaboration [17, 18]. This technique takes advantage of the unique feature of the data taken at the center-of-mass energy near the peak of the $\psi(3770)$ resonance in e^+e^- collider in which only pure $D^0\overline{D}^0$ and D^+D^- pairs are produced. Since there is no additional hadron accompany-

ing the $D\overline{D}$ final states, we select "single tag" (ST) events in which either a D or $\overline{D}$ is reconstructed without reference to the other particle, and "double tag" (DT) events in which both the D and $\overline{D}$ are reconstructed. Absolute branching fractions for D^0 or D^+ decays can then be obtained from the fraction of ST events that are DT.

Consider $N_{D\overline{D}}$ as the number of $D\overline{D}$ events (either $D^0\overline{D}^0$ or D^+D^- events) produced in the experiment, then for the decays $D \to i$ and $\overline{D} \to \bar{\jmath}$, the observed yields y_i and $y_{\bar{\jmath}}$ of reconstructed single tag events will be

$$y_i = N_{D\overline{D}}\mathcal{B}_i\epsilon_i \text{ and } y_{\bar{\jmath}} = N_{D\overline{D}}\mathcal{B}_j\epsilon_{\bar{\jmath}}, \tag{1.4}$$

where $\mathcal{B}_j$ and $\mathcal{B}_j$ are branching fractions for $D \to j$ and $\overline{D} \to \bar{\jmath}$, under the assumption that CP violation is negligible so that $\mathcal{B}_j = \mathcal{B}_{\bar{\jmath}}$. However, the efficiencies ϵ_j and $\epsilon_{\bar{\jmath}}$ for detection of these modes may not be the same due to the different cross sections for scattering of pions and kaons on the nuclei of the detector material depend on the charge of these particles.

On the other hand, the double tag yield with $D \to i$ (signal mode) and $\overline{D} \to \bar{\jmath}$ (tagging mode) will be

$$y_{i\bar{\jmath}} = N_{D\overline{D}}\mathcal{B}_i\mathcal{B}_j\epsilon_{i\bar{\jmath}}, \tag{1.5}$$

where $\epsilon_{i\bar{\jmath}}$ is the efficiency for detecting double tag events in modes i and $\bar{\jmath}$. Hence, combining the Eq. (1.4) and Eq. (1.5) gives an absolute measurement of the branching fraction $\mathcal{B}_i$,

$$\mathcal{B}_i = \frac{y_{i\bar{\jmath}}}{y_{\bar{\jmath}}}\frac{\epsilon_{\bar{\jmath}}}{\epsilon_{i\bar{\jmath}}}. \tag{1.6}$$

We can see that the branching fractions is obtained without needing to know independently the integrated luminosity or the total number of $D\overline{D}$ events produced which is usually difficult to measure accurately.

Because of the high segmentation and large solid angle of the CLEO-c detector and the low multiplicities of hadronic D decays, the double tag efficiency is approximate to the product of the two corresponding single tag efficiences, i.e. $\epsilon_{i\bar{j}} \approx \epsilon_i \epsilon_{\bar{j}}$. Therefor, the ratio $\epsilon_{\bar{j}}/\epsilon_{i\bar{j}}$ is insensitive to most systematic effects associated with the $\bar{j}$ decay mode, and a signal branching fraction $\mathcal{B}_i$ obtained using this procedure is nearly independent of the efficiency of the tagging mode.

We can also obtain the number of $D\overline{D}$ pairs by

$$N_{D\overline{D}} = \frac{y_i y_{\bar{j}}}{y_{i\bar{j}}} \frac{\epsilon_{i\bar{j}}}{\epsilon_i \epsilon_{\bar{j}}}. \tag{1.7}$$

Again, since $\epsilon_{i\bar{j}} \approx \epsilon_i \epsilon_{\bar{j}}$, the systematic error for $N_{D\overline{D}}$ is nearly independent of systematic uncertainties in the efficiencies.

In addition, we calculate the production cross sections for $D^0\overline{D}^0$ and D^+D^- by combining $N_{D^0\overline{D}^0}$ and $N_{D^+D^-}$, which are determined in the branching fraction fit, with a separate measurement of the integrated luminosity $\int \mathcal{L}dt$.

CHAPTER 2

THE CLEO-C DETECTOR

The CLEO-c detector is a general purpose facility designed to detect particles produced from the collisions of electrons and positions in the Cornell Electron Storage Ring (CESR). The name CLEO is short for Cleopatra accompanying with CESR (pronounced same as Caesar) [19] and the subscript "c" stands for charm quark in order to distinct from previous generations of the detectors. CLEO I is the first version started in October 1979, and CLEO-c is the final update which completed the data taking on March 3, 2008.

CLEO-c is a hermetic detector with different layers of subsystems for identifying charged and energetic particles. A cutaway view of CLEO-c is shown in Figure 2.1. The very inner part of the component around the interaction point is the inner stereo drift chamber (ZD) and it is surrounded by the drift chamber (DR). Both the ZD and DR are used for tracking purpose. Outside the DR is the Ring Imaging Cherenkov (RICH) counter for particle identification. Next is the crystal calorimeter (CC) to measure the energy of electromagnetic showers. The very outside are the muon chambers which is not quite useful for this analysis due to the low energetic muons produced in the D decays. A quarter view of these subdetectors is shown in Figure 2.2.

2.1 Tracking System (ZD and DR)

The innermost part of the CLEO-c detector is the ZD [20] with a radius of 5.3 to 10.5 cm. It has six layers wired with a stereo angle between 10.3° and 15.4° and covers 95% of the solid angle. Outside of the ZD is the drift chamber (DR)

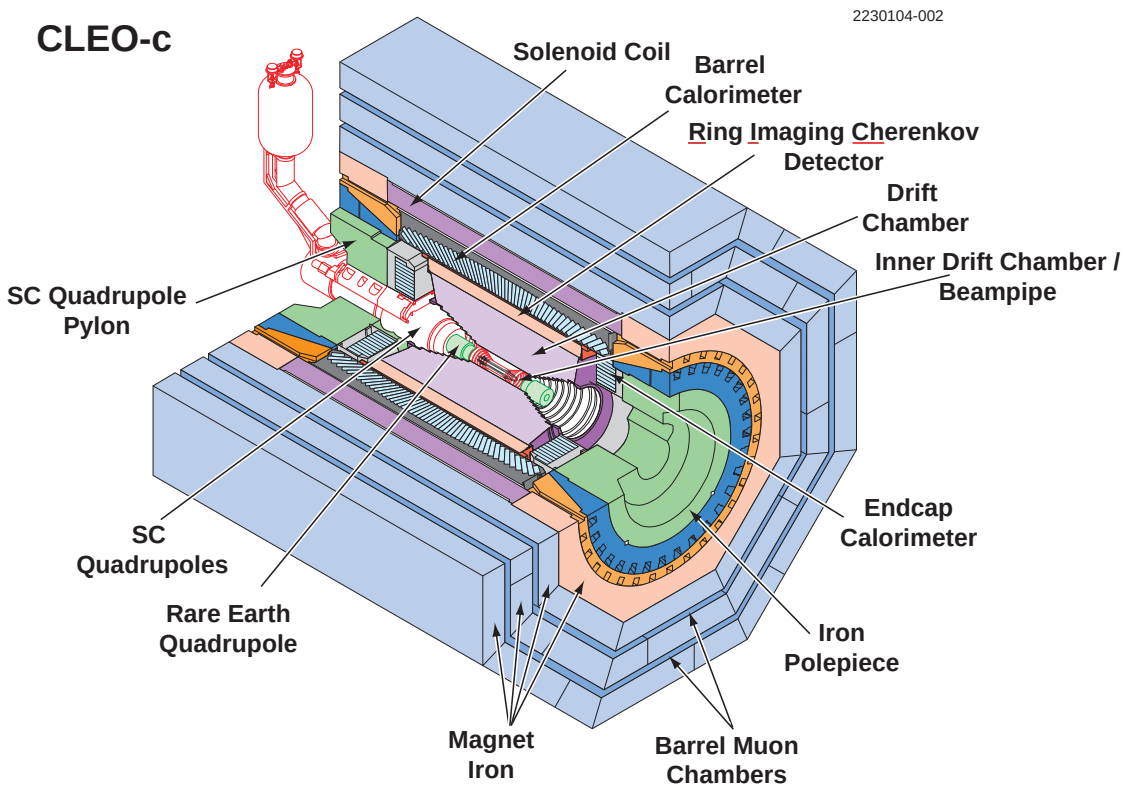

Figure 2.1: The CLEO-c detector

[20] which has radial range from 12 to 82 cm. DR consists of 47 layers where the first 16 are axial (wires parallel to the beam axis) and the remaining layers are grouped into super-layers of 4 layers each, with the super-layers alternating in stereo angle. The chambers are filled with a helium-propane gas mixture and are enclosed in an axial 1 Tesla magnetic field.

The basic unit of the ZD and DR is called "cell", which is composed with two types of wires: a "sense" wire is surrounded by parallel "field" wires. The sense wire has a positive high voltage relative to the field wires. As the cells are filled with helium-propane gas, when a charged particle passes through the cell, it ionized the gas so that the free electrons from the gas will "drift" to the

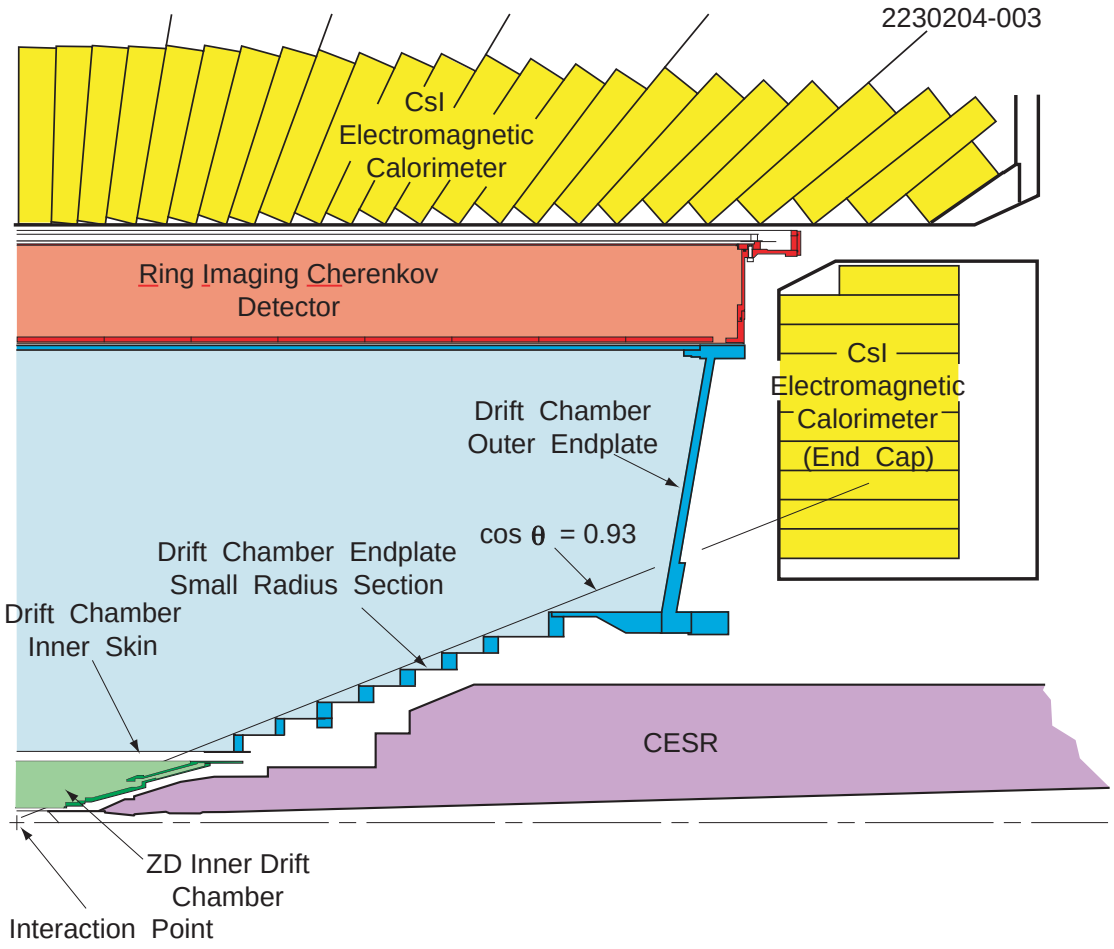

Figure 2.2: Side view of a quadrant of the CLEO-c detector

positive charged sense wires. As these electrons approach a sense wire, they will cause more ionization in the nearby gas and produce more electrons. The sense wire collect all of these electrons and record the time and charge information digitally.

The tracking system provides information about the trajectory of a charged particle, its momentum and the energy it loses per distance (dE/dx) for particle identification. The precision of the reconstructed momentum is 0.6% at 1 GeV.

2.2 Ring Imaging Cherenkov Detector (RICH)

The RICH sub-detector [21] sits outside the DR and covers 80% of the solid angle. It helps in particle identification with dE/dx information provided from the tracking system. A section of the RICH detector is shown in Figure 2.3.

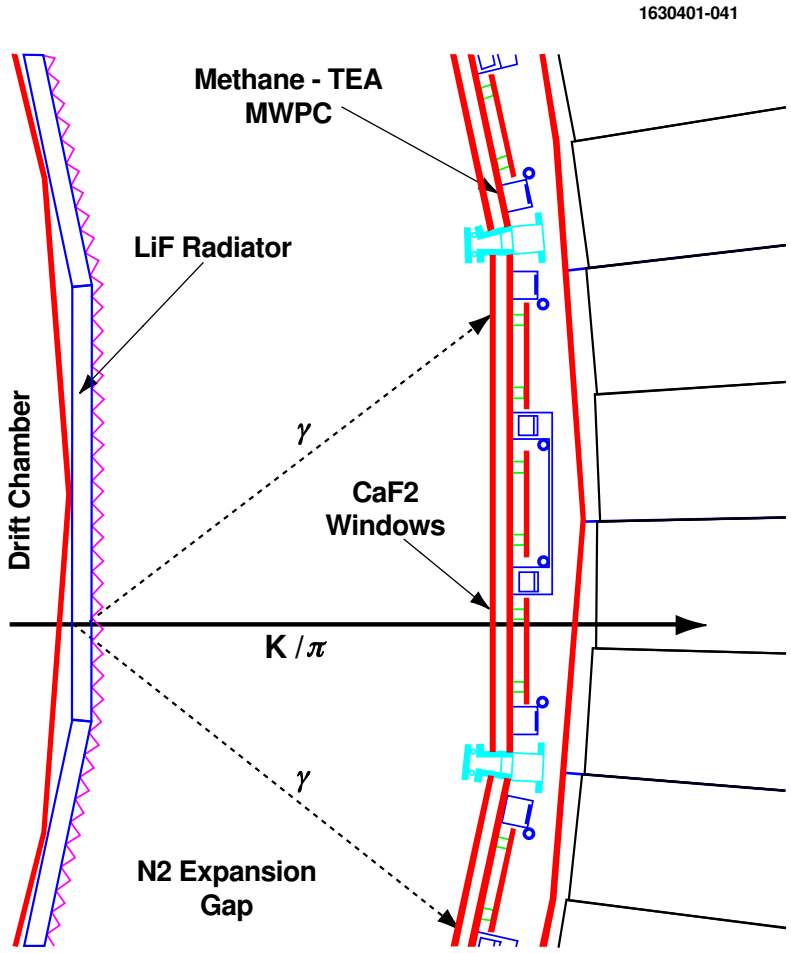

Figure 2.3: Section of the RICH detector.

Charged particles pass through a 1 cm thick lithium fluoride (LiF) radiator located at the inner radius will generate the Cherenkov light. These Cherenkov photons then travel through a 16 cm long region filled with inert nitrogen gas, where the cone expands to measurable size. They pass through a calcium fluo-

ride (CaF2) window into region filled with a methane-thriethylamine gas mixture. The gas is ionized by the photons and emit electrons which are then amplified in a multi-wire chambers. Hits in the multi-wire chambers form an ellipse segment for each Cherenkov cone. Then a likelihood based on the track path, photon positions, and their uncertainties is computed for each particle hypothesis. These likelihoods for different particles are compared to determine the most likely identity of a given track in the analysis.

2.3 Crystal Calorimeter

The Crystal Calorimeter (CC) sits outside the RICH detector and is designed for electromagnetic shower energy measurement [22]. It is made of 7800 cesium iodide (CsI) scintillating crystals which covers 95% of the solid angle including both the barrel and endcap regions. The crystals are 5 cm $\times$ 5 cm $\times$ 30 cm, with the long axis pointing in line towards the interaction point. The length of the crystal covers over 16 CsI radiation lengths which can effectively absorb all of the energy of an incident electron or photon. On the back end of each crystal mounted four photodiodes to measure the scintillation light.

Since the Molière radius of the crystals is 3.8 cm, most of the energy deposited in the calorimeter will not just be hold inside of the 5 cm $\times$ 5 cm cross section. In stead, they will spread over many adjacent crystals. Thus, a pattern recognition based on the amount of energy deposited in each crystal can be made to determine the position of the shower better than 5 cm of the crystal size. In addition, the pattern of energy deposition can be used to distinguish electromagnetic showers from hadronic ones which are usually wider than the

electromagnetic showers.

The CC provides shower energy resolution (σ_E/E) of 2.2% at 1 GeV and about 5% at 100 MeV.

CHAPTER 3

PARTICLE RECONSTRUCTION

Because the D meson decays very fast, there is no way to see them in the CLEO-c detector directly. Instead, the decay daughters from D mesons are relatively long-lived stable particles which can be measured by the detector. In this analysis, these daughters are $\pi^{\pm}$, $K^{\pm}$, π^0, and K^0_S. In addition, some daughters are still non-stable, for example π^0 will decay to two photons ($\gamma\gamma$) in less than 10^{-16} seconds ($c\tau \sim 25$ nm), thus the final state daughters are actually their "grand-children". In fact, strictly speaking, there are only two types of signal we can directly detect, the charged tracks and electromagnetic showers. From bottom to up, we can trace back (i.e. "reconstruct") to their parent particle.

3.1 Charged Particle Reconstruction

Charged particle reconstruction starts with selecting well-measured charged tracks. We require the track momentum in the range $50\ \mathrm{MeV}/c \leq p \leq 2.0\ \mathrm{GeV}/c$; the angle relative to the beam line satisfy $|\cos\theta| < 0.93$; and the hits in the drift chamber must be at least half of the layers traversed by the track. Track candidates are also required to come from interaction region in three dimensions: namely 0.5 cm close to xy plane and 5.0 cm in the z direction. These position requirements are approximately five standard deviation for the corresponding parameter. However, these track quality requirements are not applied to the $K^0_S \to \pi^+\pi^-$ reconstruction, because K^0_S usually decays several centimeters away from the interaction point. We will address this later in section 3.3.

Once we have good charged tracks, we need to identify the particle types

associated with them. In this analysis, we need to identify charged pions and kaons. Two pieces of information are used for particle identification (PID): the energy loss (dE/dx) from drift chamber and Cherenkov photons from RICH. If neither of these information is available (which is very rare), we assume the track as both a pion and a kaon candidate for later use.

If dE/dx information is available, we calculate the χ^2 from the dE/dx measurements, the expected dE/dx for pions and kaons of that momentum, and the measured resolution (σ) at that momentum:

$$\chi^2_E(\pi \text{ or K}) = \left(\frac{(\text{dE/dx})_{\text{measured}} - (\text{dE/dx})_{\text{expected}}}{\sigma} \right)^2 . \tag{3.1}$$

We reject tracks as pion or kaon candidates when the corresponding $\chi_E(\pi)$ or $\chi_E(K)$ is greater than 9. If dE/dx information is not available, we will set the χ^2 difference $\Delta\chi^2_E \equiv \chi^2_E(\pi) - \chi^2_E(K)$ equal to 0.

RICH information is only used for high-momentum tracks ($p > 700$ MeV/c) and within its acceptance ($|\cos\theta| < 0.8$). The momentum requirement is guaranteed to be above the Cherenkov threshold where we expect good efficiency for kaons and pions. We also require at least three photons associate with each track when formulating the hypothesis. Then we obtain a χ^2 difference for the RICH, $\Delta\chi^2_R \equiv \chi^2_R(\pi) - \chi^2_R(K)$, from a likelihood ratio using the locations of Cherenkov photons and the track parameters [21]. If RICH information is not available, similar as dE/dx, we set $\Delta\chi^2_R$ equal to 0.

The final charged particle identification requires a combined method using both the dE/dx and RICH information. We sum the two χ^2 differences: $\Delta\chi^2 = \Delta\chi^2_E + \Delta\chi^2_R \equiv \chi^2_E(\pi) + \chi^2_R(\pi) - \chi^2_E(K) - \chi^2_R(K)$. For each track, if $\Delta\chi^2 > 0$, we consider

it a kaon candidate; if $\Delta\chi^2 < 0$ we consider it a pion candidate; while if $\Delta\chi^2 = 0$, we utilize the track as both a kaon and a pion candidate.

3.2 π^0 Reconstruction

The neutral pion (π^0) candidates are reconstructed from the two photons they decay into, which represents 98.8% of all π^0 decays [23]. The photons create electromagnetic showers in the crystals of the calorimeter either from the barrel or endcap regions. In order to reject hadronic showers, we require the showers to be narrow by using the E9/E25 cut, which is the ratio of the deposit energy inside a 3×3 block of crystals around the cluster center to the energy in a 5×5 block. Further more, we reject showers which are very close to a track ("track-matched"). These shower are usually created by the secondary particles produced from the hadronic interactions.

To reconstruct π^0, we also require the showers to have energies greater than 30 MeV. An unconstrained invariant mass of the two photons $M(\gamma\gamma)$ is calculated under the assumption that the photons originated at the center of the detector. The uncertainty of the invariant mass $\sigma_{M(\gamma\gamma)}$ is also calculated based on the error matrices of the two photons which constitutes the variation of the location, energy, and shape of the two showers. The values of $\sigma_{M(\gamma\gamma)}$ is typically in the range 5 – 7 MeV/c^2. Then we define the "pull mass" Δ using the nominal π^0 mass M_{π^0} along with the unconstrained mass $M(\gamma\gamma)$ and $\sigma_{M(\gamma\gamma)}$:

$$\Delta \equiv \frac{M(\gamma\gamma) - M_{\pi^0}}{\sigma_{M(\gamma\gamma)}}. \tag{3.2}$$

The π^0 candidate is accepted if the invariant mass is within three standard deviations ($|\Delta| \leq 3$) of a nominal π^0 mass. Due to the energy leakage in the calorimeter for some energetic showers, we vary the nominal mass slightly with the total momentum of the π^0 candidate. For each π^0 candidate, we then perform a kinematic fit of the two photons to the mass M_{π^0} from the PDG [24]. The fitting result determines the energy and momentum of π^0, which can be handled as a single object for the proceeding analysis.

3.3 K_S^0 Reconstruction

About 69.2% of the K_S^0 decay into two opposite charged pions [23]. However we do not use the same track quality requirement for reconstruction. The main reason is that its decay length is around 2.7 cm which is quite significant apart from the interaction point. Therefore, we perform a constrained vertex fit for each pair of opposite charged tracks. If a vertex is found, we use the track parameters from the fitting result to calculate the invariant mass, $M(\pi^+\pi^-)$. Candidates with the $M(\pi^+\pi^-)$ within 12 MeV/c^2 of the mass of K_S^0 from the PDG [23] are accepted. After the selection, there is very little combinatoric peaking background in the $M(\pi^+\pi^-)$ distribution. No further requirements such as track quality or particle identification of the daughters are imposed in order to avoid unnecessary additional systematic uncertainties.

3.4 D Reconstruction

Now, as we have reconstructed $\pi^{\pm}$, $K^{\pm}$, π^0 and K^0_S candidates, we are ready to build D and $\overline{D}$ candidates in the three D^0 and six D^+ decay modes. We use energy and momentum conservation to identify valid D candidates.

First, we take advantage of the fact that the total energy of e^+e^- collision is right equal to the mass of $\psi(3770)$ which decays to D and $\overline{D}$. At one hand, we can get the energy of D or $\overline{D}$ from its daughters; on the other hand, we could determine the beam energy from accelerator parameters. Thus, we can use the energy difference as a constraint: $\Delta E \equiv E - E_0$, where E is the measured energy of D candidate and E_0 is the mean value of the beam energies. ΔE is centered around zero for D candidates. For each decay mode, we require different selection criteria of ΔE shown in Table 3.1.

Second, we formulate a momentum related variable called beam-constrained mass $M_{\rm BC}$, defined as:

$$M^2_{\rm BC}\, c^4 \equiv E^2_0 - p^2 c^2, \tag{3.3}$$

where p is the measured total momentum of the particles in the D candidate and E_0 is the beam energy as mentioned above. The $M_{\rm BC}$ peaks at the mass of the D candidates. The reason we use the beam energy is that it is measured more accurately from the accelerator, thus the mass is more "constrained" by the beam.

To get the valid D candidates yields, we fit the $M_{\rm BC}$ greater than 1.83 GeV/c^2. In the case of single tag analysis, where we only construct one D or $\overline{D}$ from the

Table 3.1: Requirements on ΔE for D candidates. The limits are set at approximately 3 standard deviations of the resolution.

Mode	Requirement (GeV)
$D^0 \to K^-\pi^+$	$\lvert\Delta E\rvert < 0.0294$
$D^0 \to K^-\pi^+\pi^0$	$-0.0583 < \Delta E < 0.0350$
$D^0 \to K^-\pi^+\pi^+\pi^-$	$\lvert\Delta E\rvert < 0.0200$
$D^+ \to K^-\pi^+\pi^+$	$\lvert\Delta E\rvert < 0.0218$
$D^+ \to K^-\pi^+\pi^+\pi^0$	$-0.0518 < \Delta E < 0.0401$
$D^+ \to K^0_S\,\pi^+$	$\lvert\Delta E\rvert < 0.0265$
$D^+ \to K^0_S\,\pi^+\pi^0$	$-0.0455 < \Delta E < 0.0423$
$D^+ \to K^0_S\,\pi^+\pi^+\pi^-$	$\lvert\Delta E\rvert < 0.0265$
$D^+ \to K^+K^-\pi^+$	$\lvert\Delta E\rvert < 0.0218$

decay process, if there is more than one candidate in a particular decay mode, we choose the one with the smallest $|\Delta E|$. Multiple candidates are common in mode like $D^+ \to K^0_S\,\pi^+\pi^+\pi^-$, where approximately 18% of the events have more than one candidate. In modes with less daughters such as $D^0 \to K^-\pi^+$ and $D^+ \to K^-\pi^+\pi^+$, the multiple candidates are very rare.

For mode $D^0 \to K^-\pi^+$ where the two charged tracks can be contaminated by $e^+e^- \to e^+e^-\gamma\gamma$, $e^+e^- \to \mu^+\mu^-\gamma\gamma$, or cosmic ray muon events, we impose additional lepton veto requirements. The events from $e^+e^- \to e^+e^-\gamma\gamma$ and $e^+e^- \to \mu^+\mu^-\gamma\gamma$ tend to populate the $M_{\rm BC}$ distribution more uniformly, while the cosmic ray events are more likely to peak in $M_{\rm BC}$ when the muon has the same momentum as the pion or kaon in the signal. Removing these events simplifies the description of the background shape in the $M_{\rm BC}$ fits. Since our double

tag modes all have at least four charged particles, the lepton veto requirements only affect the single tag yields.

In the $D^+ \to K^0_S \pi^+\pi^+\pi^-$ mode, one type of backgrounds is from Cabibbo suppressed decays $D^+ \to K^0_S K^0_S \pi^+$, where one K^0_S can decay into $\pi^+\pi^-$. To suppress this background, we veto events where the invariant mass of any pair of oppositely-charged pions (excluding those from the K^0_S decay) falls within the range $0.491 < M(\pi^+\pi^-) < 0.504$ GeV/c^2. This veto is applied for both single tag and double tag events.

For the double tag selection, we use the same ΔE criteria from Table 3.1 to obtain the the $D\overline{D}$ candidate. If there is more than one candidate in an event, we calculate the average of $M_{\rm BC}(D)$ and $M_{\rm BC}(\overline{D})$ with combination of the possible candidates and choose the one with closest value to D mass.

CHAPTER 4

ANALYSIS PROCEDURE

In this chapter, we will elucidate the main analysis procedure. We start with the description of the data and Monte Carlo samples we used for this analysis. Then we will discuss how to formulate the fitting function for signal and background shape in order to get the efficiencies and data yields for double tag and single tag events.

4.1 Data Samples

The data sample used in this analysis corresponds to an integrated luminosity of $\int \mathcal{L}dt$ = 818 pb^{-1} of e^+e^- collisions at center-of-mass energy ($E_{\rm cm}$) near 3.774 GeV. The data were produced by the symmetric e^+e^- Cornell Electron Storage Ring (CESR). The root mean square (rms) spread in the $E_{\rm cm}$ is σ_E = 2.1 MeV. The datasets are data31–33, data35–37, and data43-46.

4.2 Monte Carlo Samples

Monte Carlo simulations are widely used in this analysis to understand the detector response, determine the fitting parameters, determine selection efficiencies, and estimate backgrounds. The Monte Carlo samples are generated with the `EvtGen` program [25], and the detector response of the decay particles are simulated with GEANT [26]. Both the initial-state-radiation (ISR) and final-state-radiation (FSR) have been incorporated in the simulation process. Three types of Monte Carlo samples are mainly used:

- single tag signal Monte Carlo events, in which either the D or the $\overline{D}$ always decays in our measured nine modes, while the other side $\overline{D}$ or D decays generically,
- double tag signal Monte Carlo events, in which both the D and the $\overline{D}$ decay in measured modes, and
- generic Monte Carlo events, in which both the D and the $\overline{D}$ decay in all possible modes based on PDG [27] averages, as well as modes not listed.

In addition to the above three types, we also use continuum, tau-pair production, and ψ(2S) radiative-return events for the peaking background study.

4.3 Signal and Background Shapes

We use the same procedure to reconstruct particles and select events in data and Monte Carlo. After selection, for each D decay mode, we have a distribution of the $M_{\rm BC}$ for single tag events, and a two diminutional distribution of $M_{\rm BC}(\overline{D})$ *vs.* $M_{\rm BC}(D)$ for double tag events. To separate the signal from the background, we formulate the signal and background shape function and perform unbinned likelihood fits to extract the yields for data and Monte Carlo. Since the number of generated Monte Carlo events is known for each decay mode, we can determine the efficiencies accordingly.

Signal line shapes in the $M_{\rm BC}$ distributions have four main contributors: the beam energy spread, initial state radiation (ISR), the $\psi(3770)$ resonance line shape, and momentum resolution. The beam energy spread is determined by the properties of the accelerator, being operated here in its CESR-c configura-

tion. At E_{cm} of 3.774 GeV, the spread in the beam is σ_E = 2.1 MeV, which is less than one tenth of the $\psi(3770)$ width. The ISR photons produced before the e^+e^- collision reduce the center-of-mass energy slightly and cause a tail in the higher mass side of the M_{BC}.

The line shape of the $\psi(3770)$ resonance is described by [28]:

$$f_{BW}(E) = \frac{\Gamma(E)}{[E^2 - M_\psi^2]^2 + [M_\psi \Gamma_T(E)]^2}. \tag{4.1}$$

The numerator $\Gamma(E)$ is dependent on the $D\overline{D}$ kinematics:

$$\Gamma(E) = \Gamma_\psi \mathcal{B} \frac{q^3}{q_M^3} \frac{1 + (rq_M)^2}{1 + (rq)^2}, \tag{4.2}$$

where Γ_ψ is the measured width of the $\psi(3770)$, $\mathcal{B}$ is the branching fraction of $\psi(3770)$ decays to $D^0\overline{D}^0$ (D^+D^-) pairs, q is the momentum of D^0 (D^+) of energy $E/2$, q_M is the momentum of a D^0 (D^+) of energy $M_\psi/2$, and r is the Blatt-Weisskopf interaction radius. In the denominator of Eq. (4.1), M_ψ is the mass of the $\psi(3770)$, $\Gamma_T(E)$ is the total width for neutral and charged $D\overline{D}$ pairs, $\Gamma_T(E) \equiv \Gamma_{D^0\overline{D}^0}(E) + \Gamma_{D^+D^-}(E)$. In our fits, we use Γ_ψ = 25.2 MeV, $\mathcal{B}(D^0\overline{D}^0) = 0.57$, $\mathcal{B}(D^+D^-) = 0.43$, and $r = 12.7\ \text{GeV}^{-1}$.

The last contribution to the signal line shape is the momentum resolution of the detector, which can be described by the sum of three Gaussian resolution functions:

$$\begin{aligned} G(\mathbf{p}; \mathbf{q}, \sigma_p, f_a, s_a, f_b, s_b) = & \frac{1}{(2\pi)^{3/2}\sigma_p^3}\Bigg[(1 - f_a - f_b)e^{-(\mathbf{p}-\mathbf{q})^2/(2\sigma_p^2)} + \frac{f_a}{s_a^3}e^{-(\mathbf{p}-\mathbf{q})^2/(2(s_a\sigma_p)^2)} \\ & + \frac{f_b}{(s_a s_b)^3}e^{-(\mathbf{p}-\mathbf{q})^2/(2(s_a s_b \sigma_p)^2)}\Bigg]. \end{aligned} \tag{4.3}$$

where $\mathbf{q}$ is the true momentum of the D meson, $\mathbf{p}$ is the reconstructed momentum, and σ_p is the width of the core Gaussian, $s_a\sigma_p$ is the width of the second Gaussian; f_a is the fraction of candidates that are smeared with the width of the

second Gaussian, $s_a s_b \sigma_p$ is the width of a third Gaussian, and f_b is the fraction of candidates that are smeared with the width of the third Gaussian. All values of s_a and s_b determined from our fits are greater than 2, so the second Gaussian is significantly wider than the first and the third is significantly wider than the second.

Combinatorial backgrounds are described by a modified ARGUS function [29]:

$$a(m; m_0, \xi, \rho) = A\, m \left(1 - \frac{m^2}{m_0^2}\right)^{\rho} e^{\xi\left(1 - m^2/m_0^2\right)}, \tag{4.4}$$

where in the original form, the power parameter ρ is a constant ($\rho = 0.5$). In the function, m is the candidate mass (the $M_{\rm BC}$ in our fits), m_0 is the endpoint given by the beam energy, A is a normalization constant, and ξ is a factor in the exponential term that governs the shape of the distribution away from the endpoint region.

For the double tag fits, we plot the $M_{\rm BC}(\overline{D})$ *vs.* $M_{\rm BC}(D)$ distribution for data as shown in Figure 4.1. We can see that the signal is concentrated in the $M_{\rm BC}(\overline{D}) = M_{\rm BC}(D) = M_D$ region where the resolution is dominated by beam energy smearing [$\sigma(E_0)$ in the diagonal direction] and the momentum resolution of the $D\overline{D}$ [$\sigma(D^0)$ and $\sigma(\overline{D}^0)$ in the perpendicular directions]. The signal resolution has been included in the signal line shape functions as described above. Another feature evident in the figure is the tail of ISR events extending from the signal in the high mass side for both D and $\overline{D}$.

Also visible are the horizontal and vertical bands (Bad D^0 and Bad $\overline{D}^0$) that arise when only one D is reconstructed correctly. To account for this feature, we add two background terms where one of the D mesons is correctly reconstructed and the other one is incorrectly reconstructed. More specifically, the terms are

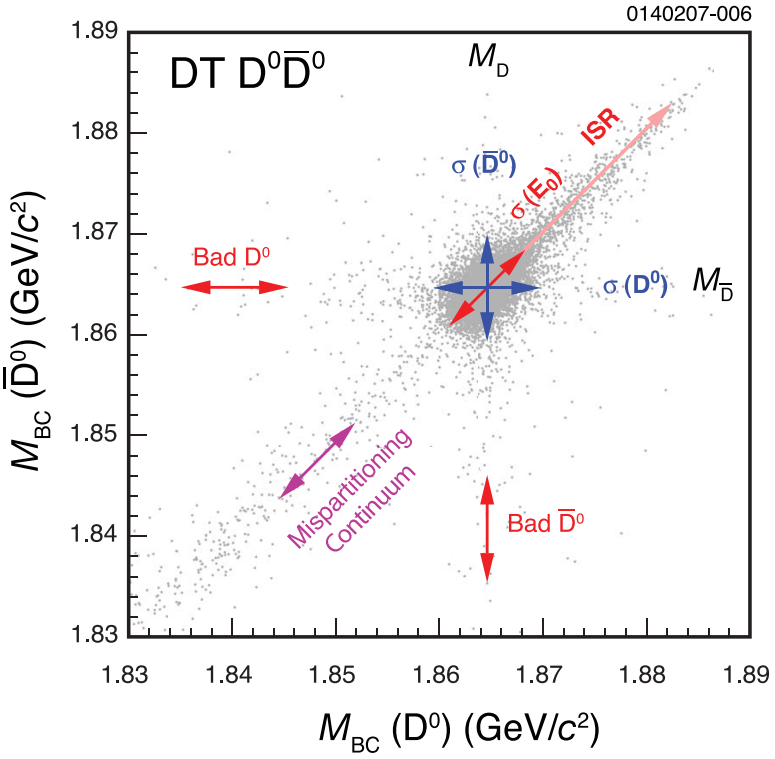

Figure 4.1: Scatter plot of $M_{\rm BC}(\overline{D})$ *vs.* $M_{\rm BC}(D)$ for $D^0\overline{D}^0$ double tag candidates in data. The descriptions of each component can be found in text.

composed of a signal function of $M_{\rm BC}(D)$ or $M_{\rm BC}(\overline{D})$ multiplied by an ARGUS function of $M_{\rm BC}(\overline{D})$ or $M_{\rm BC}(D)$.

Another feature is the diagonal band that starts from the lower corner of the $M_{\rm BC}$ and continues through the signal region and the ISR tail. As labeled in the figure, this band is populated by two sources of background - Mispartitioning and Continuum. "Mispartitioning" means one or more daughters from D are interchanged with corresponding daughters from $\overline{D}$. For example, π^0s are interchanged between the two D mesons. "Continuum" means the e^+e^- collide into lighter quark paris ($u\bar{u}$, $d\bar{d}$, and $s\bar{s}$). To include these two background sources, we add one term defined by an ARGUS background shape in $\widehat{M}_{\rm BC} \equiv$

$[M_{\rm BC}(D) + M_{\rm BC}(\overline{D})]/2$ multiplied by a Gaussian in $\Delta M_{\rm BC} \equiv [M_{\rm BC}(\overline{D}) - M_{\rm BC}(D)]/2$, where the width of the Gaussian depends linearly on $\widehat{M}_{\rm BC}$. We add the last term to account for small combinatorial backgrounds represented by the product of two ARGUS functions of $M_{\rm BC}(D)$ and $M_{\rm BC}(\overline{D})$ respectively.

Finally, we determine the momentum resolution parameters in Eq. (4.3) by fitting the charge-conjugate (also referred as "diagonal" in the text) double tag modes from signal Monte Carlo events. The fitted parameters are shown in Table 4.1. The parameters (f_a, f_b, s_a, and s_b) controlling the two wide Gaussians in the resolution function are fixed to these values in later analysis. The derivation and implementation of the fitting for $M_{\rm BC}$ is documented in [30].

Table 4.1: The momentum resolution parameters in Eq. (4.3) obtained from fits to the charge-conjugate double tag signal Monte Carlo: σ_p is the width of the core Gaussian, f_a and f_b are the fractions of the two wider Gaussians in the resolution function, $s_a\,\sigma_p$ is the width of the second Gaussian, and $s_a s_b\,\sigma_p$ is the width of the third Gaussian.

Mode	σ_p (MeV/c)	f_a	f_b	s_a	s_b
$D^0 \to K^-\pi^+$	3.94 ± 0.10	0.195 ± 0.026	0.0059 ± 0.0017	2.33 ± 0.07	3.43 ± 0.41
$D^0 \to K^-\pi^+\pi^0$	6.71 ± 0.21	0.212 ± 0.027	0.0260 ± 0.0049	2.53 ± 0.12	3.02 ± 0.31
$D^0 \to K^-\pi^+\pi^+\pi^-$	4.37 ± 0.20	0.168 ± 0.061	0.0115 ± 0.0040	2.08 ± 0.19	3.27 ± 0.43
$D^+ \to K^-\pi^+\pi^+$	4.25 ± 0.12	0.121 ± 0.030	0.0060 ± 0.0012	2.30 ± 0.14	4.00 ± 0.16
$D^+ \to K^-\pi^+\pi^+\pi^0$	6.03 ± 0.46	0.277 ± 0.083	0.0501 ± 0.0099	2.18 ± 0.18	3.32 ± 0.34
$D^+ \to K^0_S\,\pi^+$	3.98 ± 0.12	0.158 ± 0.028	0.0046 ± 0.0011	2.48 ± 0.11	4.00 ± 0.47
$D^+ \to K^0_S\,\pi^+\pi^0$	7.22 ± 0.67	0.169 ± 0.098	0.0396 ± 0.0498	2.20 ± 0.76	2.17 ± 0.41
$D^+ \to K^0_S\,\pi^+\pi^+\pi^-$	4.39 ± 0.17	0.148 ± 0.034	0.0161 ± 0.0028	2.52 ± 0.18	4.00 ± 0.17
$D^+ \to K^+K^-\pi^+$	4.68 ± 0.16	0.143 ± 0.046	0.0092 ± 0.0021	2.05 ± 0.15	3.59 ± 0.39

The fitting plots are shown in Figure A.1 where we use a square-root scale

for the y-axis. One property of the square-root scales is that the errors proportional to $\sqrt{N}$ are the same size everywhere in the figure. This results in a better visual balance between emphasizing signal (linear scale) or background details (logarithmic scale). The error bars are asymmetric and correspond to a Poisson confidence interval equivalent to 1σ for each bin content [31]. Most of the figures in the rest of this document are plotted in the square-root scale.

4.4 Double Tag Efficiencies and Data Yields

We determine double tag yields in data and Monte Carlo samples from unbinned maximum likelihood fits to $M_{\rm BC}(\overline{D})$ *vs.* $M_{\rm BC}(D)$ distributions using the signal and background functions described in the previous section. As there are 3 neutral and 6 charged decay modes, the number of combinations for the double tag decay modes are 9 for neutral and 36 for charged. For each decay mode, we plot the projection of the $M_{\rm BC}$ for D and $\overline{D}$ respectively. To demonstrate, we select 9 fitting plots out of the 45×2 from data where the other side are their charge-conjugate modes as shown in the Figure A.2. We can see that the fitting function describes the data very well with very small backgrounds.

For the signal Monte Carlo, since we know the number of generated events and there are no backgrounds, we can calculate the efficiencies for each decay mode. For the data yields, there are still some events counted as signal in the fitting which are actually backgrounds; we will discuss the measurement of these peaking backgrounds in the section on backgrounds. The efficiencies, yields from data, and those separately determined peaking backgrounds are given in Table 4.2.

Table 4.2: Double tag efficiencies, yields from data, and peaking background expectations for $D\overline{D}$ events. The efficiencies include the branching fractions for $\pi^0 \to \gamma\gamma$ and $K^0_S \to \pi^+\pi^-$ decays. The entries in the "Background" column are peaking backgrounds which are not included in the background shape function. The yields from "Data yield" are actually included the "Background" events. See Section Backgrounds for more detail.

Double tag mode	Efficiency(%)	Data yield	Background
$D^0 \to K^-\pi^+\ \overline{D}^0 \to K^+\pi^-$	42.99 ± 0.20	1825 ± 43	< 0.1
$D^0 \to K^-\pi^+\ \overline{D}^0 \to K^+\pi^-\pi^0$	24.73 ± 0.18	3886 ± 64	< 0.1
$D^0 \to K^-\pi^+\ \overline{D}^0 \to K^+\pi^-\pi^-\pi^+$	31.57 ± 0.19	2987 ± 55	10.0 ± 2.2
$D^0 \to K^-\pi^+\pi^0\ \overline{D}^0 \to K^+\pi^-$	24.40 ± 0.18	3964 ± 64	21.9 ± 10.1
$D^0 \to K^-\pi^+\pi^0\ \overline{D}^0 \to K^+\pi^-\pi^0$	13.62 ± 0.14	7600 ± 90	37.2 ± 15.4
$D^0 \to K^-\pi^+\pi^0\ \overline{D}^0 \to K^+\pi^-\pi^-\pi^+$	17.40 ± 0.16	5760 ± 78	< 0.1
$D^0 \to K^-\pi^+\pi^+\pi^-\ \overline{D}^0 \to K^+\pi^-$	31.58 ± 0.19	2895 ± 54	< 0.1
$D^0 \to K^-\pi^+\pi^+\pi^-\ \overline{D}^0 \to K^+\pi^-\pi^0$	17.32 ± 0.16	5723 ± 78	< 0.1
$D^0 \to K^-\pi^+\pi^+\pi^-\ \overline{D}^0 \to K^+\pi^-\pi^-\pi^+$	22.88 ± 0.17	4559 ± 69	3.1 ± 0.7

Continued on the next page ...

4.5 Single Tag Efficiencies and Data Yields

We select single tag events for D and $\overline{D}$ separately but combine the charge-conjugate mode when performing the $M_{\rm BC}$ fitting to extract the $D\overline{D}$ yields simultaneously in data and Monte Carlo. We use the signal and background shapes as described in Section 4.3 for the unbinned likelihood fits.

The momentum resolution parameters are fixed to the values in Table 4.1, with the exception of the core Gaussian σ_p. The core Gaussian σ_p, along with

Table 4.2 continued:

Double tag mode	Efficiency(%)	Data yield	Background
$D^+ \to K^-\pi^+\pi^+$ $D^- \to K^+\pi^-\pi^-$	30.21 ± 0.19	5951 ± 78	< 0.1
$D^+ \to K^-\pi^+\pi^+$ $D^- \to K^+\pi^-\pi^-\pi^0$	15.67 ± 0.15	1908 ± 45	< 0.1
$D^+ \to K^-\pi^+\pi^+$ $D^- \to K^0_S\pi^-$	25.02 ± 0.18	862 ± 30	10.0 ± 2.2
$D^+ \to K^-\pi^+\pi^+$ $D^- \to K^0_S\pi^-\pi^0$	13.30 ± 0.14	2032 ± 46	21.9 ± 10.1
$D^+ \to K^-\pi^+\pi^+$ $D^- \to K^0_S\pi^-\pi^-\pi^+$	16.91 ± 0.15	1067 ± 33	37.2 ± 15.4
$D^+ \to K^-\pi^+\pi^+$ $D^- \to K^-K^+\pi^-$	23.55 ± 0.17	483 ± 22	< 0.1
$D^+ \to K^-\pi^+\pi^+\pi^0$ $D^- \to K^+\pi^-\pi^-$	15.82 ± 0.15	1839 ± 44	< 0.1
$D^+ \to K^-\pi^+\pi^+\pi^0$ $D^- \to K^+\pi^-\pi^-\pi^0$	8.26 ± 0.11	644 ± 29	< 0.1
$D^+ \to K^-\pi^+\pi^+\pi^0$ $D^- \to K^0_S\pi^-$	13.03 ± 0.14	295 ± 18	3.1 ± 0.7
$D^+ \to K^-\pi^+\pi^+\pi^0$ $D^- \to K^0_S\pi^-\pi^0$	6.88 ± 0.10	601 ± 26	6.8 ± 3.2
$D^+ \to K^-\pi^+\pi^+\pi^0$ $D^- \to K^0_S\pi^-\pi^-\pi^+$	8.50 ± 0.11	369 ± 21	11.6 ± 4.8
$D^+ \to K^-\pi^+\pi^+\pi^0$ $D^- \to K^-K^+\pi^-$	12.08 ± 0.13	160 ± 14	< 0.1
$D^+ \to K^0_S\pi^+$ $D^- \to K^+\pi^-\pi^-$	25.15 ± 0.18	828 ± 29	10.0 ± 2.2
$D^+ \to K^0_S\pi^+$ $D^- \to K^+\pi^-\pi^-\pi^0$	13.14 ± 0.14	294 ± 17	3.1 ± 0.7
$D^+ \to K^0_S\pi^+$ $D^- \to K^0_S\pi^-$	20.76 ± 0.17	109 ± 11	2.7 ± 0.6
$D^+ \to K^0_S\pi^+$ $D^- \to K^0_S\pi^-\pi^0$	10.87 ± 0.13	260 ± 17	6.0 ± 1.5
$D^+ \to K^0_S\pi^+$ $D^- \to K^0_S\pi^-\pi^-\pi^+$	14.24 ± 0.14	147 ± 12	6.9 ± 2.1
$D^+ \to K^0_S\pi^+$ $D^- \to K^-K^+\pi^-$	19.45 ± 0.16	72 ± 9	0.8 ± 0.2
$D^+ \to K^0_S\pi^+\pi^0$ $D^- \to K^+\pi^-\pi^-$	13.49 ± 0.14	1851 ± 44	21.9 ± 10.1
$D^+ \to K^0_S\pi^+\pi^0$ $D^- \to K^+\pi^-\pi^-\pi^0$	6.68 ± 0.10	632 ± 26	6.8 ± 3.2
$D^+ \to K^0_S\pi^+\pi^0$ $D^- \to K^0_S\pi^-$	11.04 ± 0.13	257 ± 16	6.0 ± 1.5
$D^+ \to K^0_S\pi^+\pi^0$ $D^- \to K^0_S\pi^-\pi^0$	5.79 ± 0.10	645 ± 27	13.4 ± 6.2
$D^+ \to K^0_S\pi^+\pi^0$ $D^- \to K^0_S\pi^-\pi^-\pi^+$	7.17 ± 0.11	361 ± 20	15.6 ± 5.1
$D^+ \to K^0_S\pi^+\pi^0$ $D^- \to K^-K^+\pi^-$	10.35 ± 0.12	144 ± 13	1.8 ± 0.8
$D^+ \to K^0_S\pi^+\pi^+\pi^-$ $D^- \to K^+\pi^-\pi^-$	17.31 ± 0.15	1145 ± 34	37.2 ± 15.4
$D^+ \to K^0_S\pi^+\pi^+\pi^-$ $D^- \to K^+\pi^-\pi^-\pi^0$	8.86 ± 0.12	339 ± 20	11.6 ± 4.8
$D^+ \to K^0_S\pi^+\pi^+\pi^-$ $D^- \to K^0_S\pi^-$	14.31 ± 0.14	160 ± 13	6.9 ± 2.1
$D^+ \to K^0_S\pi^+\pi^+\pi^-$ $D^- \to K^0_S\pi^-\pi^0$	7.21 ± 0.11	359 ± 20	15.6 ± 5.1
$D^+ \to K^0_S\pi^+\pi^+\pi^-$ $D^- \to K^0_S\pi^-\pi^-\pi^+$	9.62 ± 0.12	205 ± 16	14.5 ± 5.2
$D^+ \to K^0_S\pi^+\pi^+\pi^-$ $D^- \to K^-K^+\pi^-$	13.20 ± 0.14	91 ± 10	3.0 ± 1.2
$D^+ \to K^+K^-\pi^+$ $D^- \to K^+\pi^-\pi^-$	23.72 ± 0.17	485 ± 22	< 0.1
$D^+ \to K^+K^-\pi^+$ $D^- \to K^+\pi^-\pi^-\pi^0$	12.33 ± 0.14	166 ± 13	< 0.1
$D^+ \to K^+K^-\pi^+$ $D^- \to K^0_S\pi^-$	19.39 ± 0.16	62 ± 8	0.8 ± 0.2
$D^+ \to K^+K^-\pi^+$ $D^- \to K^0_S\pi^-\pi^0$	10.19 ± 0.12	180 ± 14	1.8 ± 0.8
$D^+ \to K^+K^-\pi^+$ $D^- \to K^0_S\pi^-\pi^-\pi^+$	13.36 ± 0.14	96 ± 11	3.0 ± 1.2
$D^+ \to K^+K^-\pi^+$ $D^- \to K^-K^+\pi^-$	18.45 ± 0.16	42 ± 8	< 0.1

other parameters such as the D mass and the background ARGUS parameters ρ and ξ are constrained to be equal for D and $\overline{D}$ and determined in the fits. One minor notice for the parameter ρ is that we fixed it to 0.5 only in the two reference modes $D^0 \to K^-\pi^+$ and $D^+ \to K^-\pi^+\pi^+$ for signal Monte Carlo to make the fitting more stable due to the very small backgrounds. The fitting plots for data are shown in Figure A.3. The efficiencies, yields from data, and the similarly separately determined peaking backgrounds (see Section Backgrounds) are given in Table 4.3.

Table 4.3: Single tag efficiencies, yields from data, and peaking background expectations for $D\overline{D}$ events. The efficiencies include the branching fractions for $\pi^0 \to \gamma\gamma$ and $K^0_S \to \pi^+\pi^-$ decays. The entries in the "Background" column are peaking backgrounds which are not included in the background shape function. The yields from "Data yield" are actually include the "Background" events. See Section Backgrounds for more detail.

Single tag mode	Efficiency(%)	Data yield	Background
$D^0 \to K^-\pi^+$	65.17 ± 0.11	75177 ± 281	289 ± 14
$\overline{D}^0 \to K^+\pi^-$	65.88 ± 0.11	75584 ± 282	289 ± 14
$D^0 \to K^-\pi^+\pi^0$	35.28 ± 0.07	144710 ± 439	300 ± 17
$\overline{D}^0 \to K^+\pi^-\pi^0$	35.62 ± 0.07	145798 ± 441	300 ± 17
$D^0 \to K^-\pi^+\pi^+\pi^-$	46.82 ± 0.09	114222 ± 366	2633 ± 265
$\overline{D}^0 \to K^+\pi^-\pi^-\pi^+$	47.19 ± 0.09	114759 ± 368	2633 ± 265
$D^+ \to K^-\pi^+\pi^+$	54.92 ± 0.10	116545 ± 354	< 1
$D^- \to K^+\pi^-\pi^-$	55.17 ± 0.10	117831 ± 356	< 1
$D^+ \to K^-\pi^+\pi^+\pi^0$	28.13 ± 0.10	36813 ± 260	< 1
$D^- \to K^+\pi^-\pi^-\pi^0$	28.21 ± 0.10	37143 ± 261	< 1
$D^+ \to K^0_S\,\pi^+$	45.63 ± 0.10	16844 ± 137	197 ± 43
$D^- \to K^0_S\,\pi^-$	45.33 ± 0.10	17087 ± 138	197 ± 43
$D^+ \to K^0_S\,\pi^+\pi^0$	23.95 ± 0.11	38329 ± 262	433 ± 201
$D^- \to K^0_S\,\pi^-\pi^0$	24.10 ± 0.11	38626 ± 263	433 ± 201
$D^+ \to K^0_S\,\pi^+\pi^+\pi^-$	32.29 ± 0.14	23706 ± 224	735 ± 305
$D^- \to K^0_S\,\pi^-\pi^-\pi^+$	32.60 ± 0.14	23909 ± 225	735 ± 305
$D^+ \to K^+K^-\pi^+$	42.73 ± 0.21	10115 ± 123	< 1
$D^- \to K^-K^+\pi^-$	42.47 ± 0.20	10066 ± 123	< 1

CHAPTER 5

PEAKING BACKGROUNDS

Although the ARGUS background shape we described in Section "Signal and Background Shapes" provides a good description for the combinatorial background in fitting the $M_{\rm BC}$ distributions, there are still some small backgrounds that peak in the signal region in $M_{\rm BC}$. These backgrounds are included in the signal yields from the $M_{\rm BC}$ fitting and we have to exclude them when calculating the branching fractions. In this chapter, we describe the different types of peaking backgrounds and how to estimate their contributions for single tag and double tag cases.

5.1 "Internal" and "External" Backgrounds

The basic idea to calculate the number of backgrounds is:

$$N_{\rm background} = N_{D\overline{D}} \times \mathcal{B}_b \times p_{b\to i}, \tag{5.1}$$

where $N_{D\overline{D}}$ is the total number of $D\overline{D}$ that can be obtained from branching fraction fitter; $\mathcal{B}_b$ is the branching fraction for a D meson to decay to the background-contributing mode b; and $p_{b\to i}$ is the probability that a D that decays to the mode b is reconstructed as an i signal candidate. The probability $p_{b\to i}$ can be determined from Monte Carlo simulations. There are slight complications in determining the $\mathcal{B}_b$ based on the source of the backgrounds, which will be discussed below.

There are two types of peaking backgrounds depending on whether they are among our measured 9 modes or not: "internal" backgrounds and "external" backgrounds. "Internal" backgrounds come from the D mesons that decay

into one of the 9 signal modes (including the charge-conjugate modes) and are accepted as candidates for a different signal mode. For this reason, these backgrounds are also called "cross-feeds" in our analysis. "External" backgrounds are the decays not measured in our 9 signal modes, which feed down to contaminate our signal yields.

For "internal" backgrounds, we use the values of $\mathcal{B}_b$ obtained from the branching fraction fitter, while for "external" backgrounds, we use fixed values of $\mathcal{B}_b$ for some modes from the PDG [23] or use a data-driven technique to determine the absolute subtraction numbers. During each iteration of the fitter, since the values of $N_{D\overline{D}}$ and $\mathcal{B}_b$ will be calculated by the fitter, the backgrounds will also be updated accordingly. The dependence of the subtracted backgrounds on the fit parameters is accounted for by the fitter in its χ^2 minimization. For external backgrounds, we include the uncertainties in the PDG values of $\mathcal{B}_b$ to estimate the associated systematic errors.

To identify the major sources of external backgrounds we study generic $D\overline{D}$ Monte Carlo samples. For the internal backgrounds study, we use single tag signal Monte Carlo samples. In a single tag signal Monte Carlo event, the non-signal tag side D or $\overline{D}$ decays generically, so some external backgrounds can also be present in signal Monte Carlo simulations. We therefore remove the external backgrounds contribution when studying the internal backgrounds. In the next two subsections, we will discuss different peaking backgrounds based on single tag and double tag situations.

5.2 Single Tag Backgrounds

5.2.1 Doubly Cabibbo suppressed modes (external)

Monte Carlo study indicates that for the neutral D mesons, the doubly Cabibbo suppressed decays (DCSD) $\overline{D}^0 \to K^-\pi^+$ and $\overline{D}^0 \to K^-\pi^+\pi^0$ are the largest peaking backgrounds for D^0 decays to these final states. The decay $\overline{D}^0 \to K^-\pi^+\pi^+\pi^-$ contributes significantly to the background for that D^0 final state, but this contribution is smaller compared with the two singly Cabibbo suppressed decays (SCSD), $D^0 \to K^-K^0_S\,\pi^+$ and $D^0 \to K^+K^0_S\,\pi^-$, which will be discussed separately.

On the other hand, for the charged D decays to $D^+ \to K^-\pi^+\pi^+$ or $D^+ \to K^-\pi^+\pi^+\pi^0$, DCSD could contribute to the peaking backgrounds only if a double misidentification – misidentify a π^+ as a K^+ and the K^- as a π^- – happens, which is very rare. Even if that happend, this background will mostly be rejected by the ΔE requirement. For the modes in which the decay daughter contains K^0_S (such as $D^+ \to K^0_S\,\pi^+$, $D^+ \to K^0_S\,\pi^+\pi^0$, and $D^+ \to K^0_S\,\pi^+\pi^+\pi^-$) there are contributions from DCSD [32], but we do not regard them as backgrounds since we are measuring the decays to K^0_S rather than K^0 or $\overline{K}^0$.

The resonant substructure of $D^0 \to K^+\pi^-\pi^0$ is slightly different for Cabibbo favored decays (CFD) and DCSD modes [33], and a similar difference can be present in $D^0 \to K^+\pi^-\pi^+\pi^-$. The differences in resonant substructure may lead to different values of $p_{b\to i}$ for these modes. We simulate these decays with kinematic distributions flat in phase space and compare the efficiencies in these samples with the nominal Cabibbo-allowed efficiencies as a gauge of the size of these effects. We find no statistically significant difference between the two val-

ues of $p_{b\to i}$ in either mode. So, we use the values of $p_{b\to i}$ for the flat distribution when estimating backgrounds.

5.2.2 $D^0 \to K^- K^0_S \pi^+$ and $D^0 \to K^+ K^0_S \pi^-$ (external)

The two external SCSD modes $D^0 \to K^- K^0_S \pi^+$ and $D^0 \to K^+ K^0_S \pi^-$ can contribute to the decays $D^0 \to K^-\pi^+\pi^+\pi^-$ and $\overline{D}^0 \to K^+\pi^-\pi^-\pi^+$ respectively when the K^0_S decays to $\pi^+\pi^-$. Since we require the pion tracks originate near the interaction region as described in Chapter "Particle Reconstruction", these SCSD decays are less likely to appear in our signal due to the long decay length of the K^0_S. However, the requirement of pion tracks may cause the $p_{b\to i}$ to be dependent on the K^0_S momentum spectrum. To test this effect, we use mixtures of resonant ($K^{*\pm}K^{\mp}$) and non-resonant contributions based on PDG averages [24]; we found no statistically significant discrepancies in the efficiency of the two mixtures.

5.2.3 $D^+ \to$ multipions (external)

The SCSD decays into multipions can fake our signal modes with K^0_S mesons if the invariant mass of a pair of pions ($\pi^+\pi^-$) happens to fall within the K^0_S mass window. We estimate the size of this background through a data-driven approach by using K^0_S mass sidebands. We require that the reconstructed K^0_S candidate have a mass in one of the ranges $0.470 < M(\pi^+\pi^-) < 0.482$ GeV/c^2 or $0.5134 < M(\pi^+\pi^-) < 0.5254$ GeV/c^2, and that the D^+ candidate using this K^0_S otherwise satisfies all standard requirements. The $M_{\rm BC}$ spectra of these candidates are then fit with the standard line shapes for the mode being faked, as shown in

Figure A.4. The momentum resolutions are set to the values obtained from the charge-conjugate double tag fits for these modes in data.

The yields obtained in the sidebands have a significant contribution from the tails of the K^0_S mass resolution, so some signal is counted in our sidebands. To disentangle this effect, we use Monte Carlo to obtain efficiencies for events with real K^0_S mesons to be reconstructed in the sideband region. The efficiencies are shown in Table 5.1. The efficiency to be reconstructed in the signal region is just the signal efficiency in Table 4.3. The sidebands are assumed to have the same number of background events as the signal region. We write an efficiency matrix E, with entries giving the efficiencies for real and background events to be found in signal and sideband regions, and invert it to obtain the number of real and background events:

$$\begin{pmatrix} N_{sig} \\ N_{bkg} \end{pmatrix} = \begin{pmatrix} E_{sig\to sig} & E_{bkg\to sig} \\ E_{sig\to sb} & E_{bkg\to sb} \end{pmatrix}^{-1} \begin{pmatrix} Y_{sig} \\ Y_{sb} \end{pmatrix}.$$

In addition we test this procedure on generic MC by reconstructing events with the signal K^0_S mass region that arose from multipion events and using the fractional difference between the sideband prediction and the observed yield to set a fractional systematic error. The raw sideband yield from data and the final corrected backgrounds are shown in Table 5.2. Since these background estimates are determined directly from data, they do not depend on an input branching fraction or $N_{D\overline{D}}$.

Table 5.1: Efficiency for signal events to be reconstructed in K^0_S sidebands, taken from signal MC. Uncertainties are statistical only.

Mode	$E_{sig\to sb}$ (10^{-3})
$D^+ \to K^0_S \pi^+$	7.8 ± 0.2
$D^+ \to K^0_S \pi^+\pi^0$	9.5 ± 0.3
$D^+ \to K^0_S \pi^+\pi^+\pi^-$	33.0 ± 0.6

Table 5.2: External backgrounds for multipions measured as absolute subtractions to data yields. Raw yield uncertainty is statistical only; corrected background uncertainties are statistical, efficiency uncertainty, and generic MC agreement.

Background	Raw sideband yield	Corrected background
$D^+ \to \pi^+\pi^-\pi^+$ fakes $D^+ \to K^0_S\pi^+$	482 ± 33	$198 \pm 34 \pm 21 \pm 18$
$D^+ \to \pi^+\pi^-\pi^+\pi^0$ fakes $D^+ \to K^0_S\pi^+\pi^0$	1965 ± 108	$463 \pm 113 \pm 69 \pm 169$
$D^+ \to 3\pi^+2\pi^-$ fakes $D^+ \to K^0_S\pi^+\pi^+\pi^-$	2647 ± 153	$250 \pm 172 \pm 57 \pm 125$

5.2.4 $D^+ \to K^0_S K^0_S \pi^+$ (external)

This SCSD mode can be reconstructed as $D^+ \to K^0_S \pi^+\pi^+\pi^-$ if the $\pi^+\pi^-$ pair from one of the two K^0_Ss fails the K^0_S reconstruction criteria. The probability of this faking background is limited by two factors: we veto $K^0_S \pi^+\pi^+\pi^-$ candidates in which either of the $\pi^+\pi^-$ combinations satisfied $0.491 < M(\pi^+\pi^-) < 0.504$ GeV/c^2; and we require that the pion tracks originated near the interaction region to prevent K^0_S faking $\pi^+\pi^-$ as mentioned in Section "K^0_S Reconstruction".

This final state is dominated by the two-body intermediate state $K^{*+}K^0_S$, and thus it is modeled well in `EvtGen`. We use the value of $\mathcal{B}(D^+ \to K^{*+}K^0_S)$ obtained

by the E687 Collaboration [34].

5.2.5 Particle swap (internal)

"Swapping" a pion and a kaon during particle identification, e.g., reconstructing a K^+ as a π^+ and a π^- as a K^-, can result in a $\overline{D}^0$ decay being reconstructed as a D^0 decay. This double misidentification is suppressed relative to correct reconstruction by a factor of $\approx 10^{-3}$ for $D^0 \to K^-\pi^+$ due to the high momentum of the two tracks. It is not observable in any of the other modes, where more than two particles are in the final state and they have lower momentum and better dE/dx discrimination.

We obtain the efficiency for this process by using the signal Monte Carlo for $D^0 \to K^-\pi^+$. Events with genuine $\overline{D}^0 \to K^+\pi^-$ on the other side are rejected, and the yield of candidates reconstructed in the remaining events as having $\overline{D}^0 \to K^+\pi^-$ is measured. The yield fits to signal Monte Carlo are shown in Figure A.5.

5.2.6 Other peaking backgrounds check

To estimate the possible remaining peaking backgrounds, we remove the signals and the above mentioned backgrounds in generic Monte Carlo, then look at the $M_{\rm BC}$ spectra for the D candidates, as shown in Figure A.6. The largest peaking is less than 0.02% in $D^0 \to K^-\pi^+$ due to bad modeling of the non-peaking background. There is no evidence of peaking background in other modes.

We also check the peaking background in continuum, radiative return, and τ-pair Monte Carlo samples with their corresponding $M_{\rm BC}$ spectra shown in Figures A.7, A.8, and A.9. We found no evidence for peaking background in any of the signal D decay modes.

5.3 Double Tag Backgrounds

We consider the same potential sources of background in double tag as in single tag backgrounds for both the D and $\overline{D}$ candidates. However, we calculate double tag background rates separately from single tag rates. For example, including a rate for $D^0 \to K^- K^0_S \pi^+$ to fake $D^0 \to K^- \pi^+ \pi^+ \pi^-$ does not automatically give a rate for $D^0 \to K^- K^0_S \pi^+$ to create fake double tags. We can categorize the double tag backgrounds into two cases: one tag side faking and both tag sides faking.

In the one tag side faking case where $D \to i$ is correctly reconstructed but $\overline{D} \to \bar{k}$ is misreconstructed as a $\overline{D} \to \bar{\jmath}$ decay, we predict the background event count $n_{i,\bar{k}\to\bar{\jmath}}$ using

$$n_{i,\bar{k}\to\bar{\jmath}} = N_{D\overline{D}}\, \epsilon_i\, \mathcal{B}_i\, p_{\bar{k}\to\bar{\jmath}}\, \mathcal{B}_{\bar{k}}. \tag{5.2}$$

In this equation, $p_{\bar{k}\to\bar{\jmath}}$ is the probability for a $\overline{D} \to \bar{k}$ decay to be reconstructed as a single tag $\overline{D} \to \bar{\jmath}$ decay. The branching fractions $\mathcal{B}_i$ and $\mathcal{B}_{\bar{k}}$ are taken from the previous CLEO-c branching fraction result [35], or the PDG [24] for external modes not included in the earlier CLEO-c measurement. Charge conjugate DT backgrounds are set to equal.

On the other hand, the chance of having a fake on both tag sides is usually very small and we just ignore it. The exceptions are the neutral DCSD

modes and the "wrong-sign" mode $D^0 \to K^+ K^0_S \pi^-$. If one side produces such a decay, it is impossible to produce a double tag unless the other side undergoes a wrong-sign decay too. This severely suppresses these backgrounds in the double tags, so for example the background due to DCSD decays for $D^0 \to K^-\pi^+\pi^0/\overline{D}^0 \to K^+\pi^-\pi^0$ is expected to be less than 10^{-2} event in data. We included these decays by choosing a particular wrong-sign background mode i, using ϵ_i and $\mathcal{B}_i$ as expected for mode i to fake single tags, and then summing Eq. (5.2) over the wrong-sign background modes $\bar{k}$ for the other side.

CHAPTER 6

SYSTEMATIC UNCERTAINTIES

Systematic uncertainties are accounted for in the branching fraction fit, by including them directly in the χ^2 minimization. We will discuss different contributions for the systematic uncertainties in the following sections.

6.1 Signal Shape Parameterization

To gauge the sensitivity of the single tag and double tag yields to variations in the $M_{\rm BC}$ fit functions, we vary the parameter values of the signal line shape. The main parameters here are the mass (M) and width (Γ) of the $\psi(3770)$ as well as the Blatt-Weisskopf radius (R). We vary these parameters by ± 0.5 MeV/c^2, ± 2.5 MeV, and ± 4 GeV^{-1} respectively and fit data. Since the differences in the double tags are negligible compared with single tags, we only consider the single tags, as shown in Tables B.1, B.2, and B.3 for the three variations respectively.

Among two charge-conjugate decays in each mode, we choose the larger difference for that mode and then add in quadrature the three differences (mass, width, and R) to get the systematic uncertainties for the line shape parameters as shown in Table 6.1.

6.2 Double DCSD Interference

In the neutral double tag modes, the CFD amplitudes can interfere with amplitudes where both D^0 and $\overline{D}^0$ undergo DCSD. If we denote the final states as $f_1\bar{f}_2$,

Table 6.1: Systematic uncertainties of line shape parameters.

Mode	Difference(%)			Total
	M(±0.5) MeV/c^2	Γ(±2.5) MeV	R(±4) GeV^{-1}	(%)
$D^0 \to K^-\pi^+$	0.14	−0.36	−0.12	0.40
$\overline{D}^0 \to K^+\pi^-\pi^0$	0.18	−0.45	−0.12	0.50
$D^0 \to K^-\pi^+\pi^+\pi^-$	0.20	−0.46	−0.10	0.51
$D^+ \to K^-\pi^+\pi^+$	−0.12	−0.29	−0.13	0.34
$D^- \to K^+\pi^-\pi^-\pi^0$	0.21	−0.41	−0.15	0.48
$D^+ \to K^0_S\,\pi^+$	0.15	−0.33	−0.14	0.39
$D^+ \to K^0_S\,\pi^+\pi^0$	0.20	−0.41	−0.15	0.48
$D^+ \to K^0_S\,\pi^+\pi^+\pi^-$	0.26	−0.46	−0.15	0.55
$D^+ \to K^+K^-\pi^+$	−0.24	−0.46	−0.15	0.54

the two transition amplitudes are CFD ($D^0 \to f_1$, $\overline{D}^0 \to \bar{f}_2$) and DCSD ($D^0 \to \bar{f}_2$, $\overline{D}^0 \to f_1$). The interference [36, 37] between these two processes is governed by two amplitude ratios:

$$\langle f_1|\overline{D}^0\rangle/\langle f_1|D^0\rangle \equiv -r_1 e^{-i\delta_1} \tag{6.1}$$

and

$$\langle f_2|\overline{D}^0\rangle/\langle f_2|D^0\rangle \equiv -r_2 e^{-i\delta_2}, \tag{6.2}$$

where the r_i are magnitudes and therefore strictly positive, and the δ_i are mode-dependent strong phases. The size of the interference effect is:

$$\Delta = 2r_1 r_2 \cos(\delta_1 + \delta_2) - r_1^2 r_2^2. \tag{6.3}$$

For the input values in Eq. (6.3), we take the r_i and δ_i from [38] and apply for decay $D^0 \to K^-\pi^+$ directly. For $D^0 \to K^-\pi^+\pi^0$ and $D^0 \to K^-\pi^+\pi^+\pi^-$ decays, we

take the r_i from PDG [23] and δ_i from [39] by rotating 180° due to a difference in the phase convention. We also need to substitue $\cos\delta$ as $R\cos\delta$ to use in Eq. (6.3), where R is the coherence factor and is also measured in [39]. The correction factors for the yields, i.e. $1/(1 - \Delta)$, are shown in Table 6.2.

Table 6.2: DCSD interference corrections

Mode	Yield correction factor
$D^0 \to K^-\pi^+\ \overline{D}^0 \to K^+\pi^-$	1.005 ± 0.002
$D^0 \to K^-\pi^+\ \overline{D}^0 \to K^+\pi^-\pi^0$	1.002 ± 0.002
$D^0 \to K^-\pi^+\ \overline{D}^0 \to K^+\pi^-\pi^-\pi^+$	1.005 ± 0.003
$D^0 \to K^-\pi^+\pi^0\ \overline{D}^0 \to K^+\pi^-$	1.002 ± 0.002
$D^0 \to K^-\pi^+\pi^0\ \overline{D}^0 \to K^+\pi^-\pi^0$	1.000 ± 0.002
$D^0 \to K^-\pi^+\pi^0\ \overline{D}^0 \to K^+\pi^-\pi^-\pi^+$	1.005 ± 0.002
$D^0 \to K^-\pi^+\pi^+\pi^-\ \overline{D}^0 \to K^+\pi^-$	1.005 ± 0.003
$D^0 \to K^-\pi^+\pi^+\pi^-\ \overline{D}^0 \to K^+\pi^-\pi^0$	1.005 ± 0.002
$D^0 \to K^-\pi^+\pi^+\pi^-\ \overline{D}^0 \to K^+\pi^-\pi^-\pi^+$	0.996 ± 0.004

6.3 Detector Simulation

6.3.1 Tracking and K^0_S Efficiencies

Based on the study of tracking efficiencies for pions and kaons in [40], there is good agreement between data and Monte Carlo and no need to make corrections to efficiency. We therefore use the suggested value of a systematic uncertainty of 0.3% per pion track and 0.6% per kaon track for all modes. These track-

ing systematics are treated as correlated between all particles. We apply a 0.8% K^0_S reconstruction efficiency systematic uncertainty to K^0_S candidates according to [41]. This uncertainty is correlated among K^0_S candidates.

6.3.2 π^0 Efficiency

The π^0 finding efficiencies in data and Monte Carlo have been studied in [42]. The efficiency correction and its uncertainty can be written as following:

$$\epsilon_{\text{data}}/\epsilon_{\text{MC}} = a_1 \bar{p}_{\pi^0} + a_0 \tag{6.4}$$

$$\sigma_{\epsilon_{\text{data}}/\epsilon_{\text{MC}}} = \sqrt{\sigma^2_{a_1} \bar{p}^2_{\pi^0} + \sigma^2_{a_0} + 2\rho_{01}\sigma_{a_0}\sigma_{a_1}\bar{p}_{\pi^0}} \tag{6.5}$$

where $\bar{p}_{\pi^0}$ is the average π^0 momentum for data, and other fitting parameters are [42]: $a_0 = 0.939 \pm 0.022$, $a_1 = 0.001 \pm 0.021$, $\rho_{01} = -0.947$. We obtain the $\bar{p}_{\pi^0}$ in data for the decays $D^0 \to K^-\pi^+\pi^0$, $D^+ \to K^-\pi^+\pi^+\pi^0$, and $D^+ \to K^0_S\pi^+\pi^0$ based on the π^0 momentum distributions as shown in Figure A.10.

Putting it all together, we get the corrections for the three modes in Table 6.3. We correct the efficiencies based on the average π^0 momentum in double tag and single tag by a factor of 0.939 for these three modes, and take systematic uncertainties of 1.3%, 1.5%, and 1.3% for each mode respectively.

6.3.3 Particle Identification Efficiencies

Particle identification efficiencies are studied [43] by reconstructing decays with unambiguous particle content, such as $D^0 \to K^0_S\pi^+\pi^-$ and $\phi \to K^+K^-$. The decay of $D^0 \to K^-\pi^+\pi^0$ is also used for the study as the K^- and π^+ can be distinguished

Table 6.3: π^0 efficiency correction. $\bar{p}_{\pi^0}$ is the average momentum for π^0.

Mode	$\bar{p}_{\pi^0}$ (GeV)	$\epsilon_{\text{data}}/\epsilon_{\text{MC}}$
$D^0 \to K^-\pi^+\pi^0$	0.478	0.939 ± 0.013
$D^+ \to K^-\pi^+\pi^+\pi^0$	0.339	0.939 ± 0.015
$D^+ \to K^0_S\,\pi^+\pi^0$	0.498	0.939 ± 0.013

kinematically. There is good agreement between data and Monte Carlo with small discrepancies. In each final state, we apply the suggested efficiency correction factor 0.995 per PID-identified $\pi^\pm$s and 0.990 per PID-identified $K^\pm$s. We also assign correlated uncertainties of 0.25% and 0.3% to each $\pi^\pm$ and $K^\pm$, respectively. Since the K^0_S daughters are not selected with the $\pi^\pm$ PID requirements, we do not assign these corrections and uncertainties to them.

6.4 Lepton Veto

As discussed in Section *D* Reconstruction, we imposed additional lepton veto requirements for $D^0 \to K^-\pi^+$ single tag candidates in order to eliminate $e^+e^- \to e^+e^-\gamma\gamma$, $e^+e^- \to \mu^+\mu^-\gamma\gamma$, and cosmic ray muon events. We compared the number of events before and after using this requirement, and found the number of events after using this veto decreased approximately 0.1%. We therefore assign a systematic uncertainty of 0.1% to $D^0 \to K^-\pi^+$ single tag yields to account for this effect.

6.5 Trigger Simulation

We use events that are accepted by any trigger line. In practice most of our events are flagged by the two-track trigger, which has some inefficiency for soft tracks. Based on the Monte Carlo trigger simulation, there is no significant deviations from 100% efficiency for all modes as shown in Table 6.4. Consequently, we do not assign systematic uncertainty on trigger simulation.

Table 6.4: Trigger efficiencies derived from signal MC.

Mode	Trigger efficiency (%)
$D^0 \to K^-\pi^+$	99.983 ± 0.004
$D^0 \to K^-\pi^+\pi^0$	99.981 ± 0.004
$D^0 \to K^-\pi^+\pi^+\pi^-$	99.974 ± 0.004
$D^+ \to K^-\pi^+\pi^+$	99.969 ± 0.004
$D^+ \to K^-\pi^+\pi^+\pi^0$	$100^{+0}_{-0.000}$
$D^+ \to K^0_S\,\pi^+$	$100^{+0}_{-0.000}$
$D^+ \to K^0_S\,\pi^+\pi^0$	$100^{+0}_{-0.002}$
$D^+ \to K^0_S\,\pi^+\pi^+\pi^-$	99.996 ± 0.002
$D^+ \to K^+K^-\pi^+$	99.998 ± 0.002

6.6 $|\Delta E|$ Requirement

ΔE is defined as the difference between the measured energy of the D candidate and beam energy. Any discrepancy in detector resolution between data and Monte Carlo simulations can cause systematic bias. To estimate this effect, we

apply a wider ΔE cut, i.e. $2 \times \Delta E$, for both data and Monte Carlo samples. Then we calculate the ratio of yields (or efficiences for Monte Carlo) between the standard ΔE cut and $2 \times \Delta E$ cut. For single tag events, we choose the maximum value of the ratios (Data/MC) among charge-conjugate mode from Table B.4 and use the difference between these values and 1 as the systematic uncertainty, as shown in Table 6.5. For the double tag events we assign a conservative uncertainty 1.0% for the diagonal double tags, and $\sqrt{2}\cdot$ 0.5% for all non-diagonal double tags in the branching fraction fitter.

Table 6.5: Systematic uncertainty of ΔE cuts. The Ratios are taken from the max of the value in Table B.4, and the systematics are the difference between the Ratio and 1.

Mode	Ratio (Data/MC)	Syst (%)
$\overline{D}^0 \to K^+\pi^-$	1.001 ± 0.001	0.1
$\overline{D}^0 \to K^+\pi^-\pi^0$	0.998 ± 0.000	0.2
$\overline{D}^0 \to K^+\pi^-\pi^-\pi^+$	0.998 ± 0.001	0.2
$D^- \to K^+\pi^-\pi^-$	1.001 ± 0.001	0.1
$D^+ \to K^-\pi^+\pi^+\pi^0$	1.002 ± 0.001	0.2
$D^+ \to K^0_S\,\pi^+$	1.000 ± 0.001	0.0
$D^+ \to K^0_S\,\pi^+\pi^0$	1.004 ± 0.001	0.4
$D^- \to K^0_S\,\pi^-\pi^-\pi^+$	1.012 ± 0.001	1.2
$D^+ \to K^+K^-\pi^+$	0.998 ± 0.002	0.2

6.7 Background Shape

The systematic uncertainty of background shape (ARGUS function) in single tag yields is estimated by using alternative ARGUS parameters. To get reasonable alternatives, we select events in low and high ΔE sidebands based on the ΔE requirements for each decay mode. Then we fit the $M_{\rm BC}$ distributions of these sideband events with an ARGUS function as shown in Figures A.11 and A.12 for low and high ΔE sidebands respectively. Once we obtain the ARGUS parameters, we use them to fit single tag events within the normal ΔE region. We choose the maximum difference among the shifts of the yields for each mode and use these values for the systematic uncertainty (see Table B.5).

6.8 Final State Radiation

FSR is simulated by PHOTOS in both the signal Monte Carlo and the generic Monte Carlo simulations. In the simulations, the reduction of double tag efficiencies due to FSR is approximately a factor of two larger than the reduction of single tag efficiencies due to FSR. The accuracy of the FSR simulation has been verified to 8% of itself using $J/\psi \to \mu^+\mu^-$ decays [44, 45]. Base on the study by he Heavy Flavor Averaging Group (HFAG) [46], we assign uncertainties of ±25% of the FSR correction to the efficiency difference in Table B.6 as the uncertainty in each mode. This uncertainty is correlated across all modes.

6.9 Event Topology

If the Monte Carlo does not correctly simulate global features of an event, i.e., the event topology, it is possible for the efficiency derived from the Monte Carlo to differ from the real efficiency, even if the Monte Carlo models component features such as track- and π^0-level efficiency correctly. We will evaluate and check the sources of such error in the following subsections.

6.9.1 Resonant Substructure

If the Monte Carlo simulation includes an incorrect resonant substructure for three- and four-body decay modes, the momentum distribution of the final state particles will be distorted. As the particle detection efficiency depends on the momentum distribution, the resonant substructure can have an effect on the average efficiency for the D reconstruction. To extract a systematic uncertainty on the efficiencies due to these effects, we obtain the effective efficiency as a function of momentum for each of the daughter particles in a given mode from Monte Carlo, then unweight the observed momentum distribution in generic Monte Carlo and data for each daughter. This gives an effective overall efficiency for that data sample. The comparison plots between data and Monte Carlo to determine this systematic uncertainty are shown in Figures A.13 – A.19. The systematic uncertainties for each mode are shown in Table 6.6 in which we take the maximum value for each mode.

For $D^+ \to K^+K^-\pi^+$ mode, we use a more conservative method [47] to determine the systematic uncertainty. The data/MC comparisons for mass distribu-

Table 6.6: Resonant substructure systematic uncertainties.

Mode	dau1(%)	dau2(%)	dau3(%)	dau4(%)	max (%)
$D^0 \to K^-\pi^+$	–	–	–	–	–
$D^0 \to K^-\pi^+\pi^0$	0.58	0.09	0.19	–	0.58
$D^0 \to K^-\pi^+\pi^+\pi^-$	1.3	0.12	0.58	0.16	1.3
$D^+ \to K^-\pi^+\pi^+$	0.53	0.23	0.21	–	0.53
$D^+ \to K^-\pi^+\pi^+\pi^0$	0.94	0.43	0.19	0.12	0.94
$D^+ \to K^0_S\,\pi^+$	–	–	–	–	–
$D^+ \to K^0_S\,\pi^+\pi^0$	0.42	0.23	0.39	–	0.42
$D^+ \to K^0_S\,\pi^+\pi^+\pi^-$	0.62	0.22	0.41	0.13	0.62
$D^+ \to K^+K^-\pi^+$	0.62	1.63	0.01	–	1.63

tions are shown in Figure 6.1. We divide the signal Monte Carlo sample into three subsets: $\phi\pi^+$, $\overline{K}^{*0}K^+$, and phase-space (this represents more than 95% for the total sample). Then calculate the efficiency for each subset and compare with the normal efficiency (see Table 6.7). We therefore assign the maximum difference 5.82% error for this mode.

Table 6.7: Resonant substructure systematic uncertainties for decay mode $D^+ \to K^+K^-\pi^+$. Here "Eff" stands for the normal efficiency from the signal MC, "PHSP" is phase-space.

Mode	Eff(%)	$\phi\pi^+$(%)	$\overline{K}^{*0}K^+$(%)	PHSP(%)	max-diff(%)
$D^+ \to K^+K^-\pi^+$	42.73 ± 0.21	43.68 ± 0.38	45.21 ± 0.37	40.52 ± 0.33	5.80
$D^- \to K^-K^+\pi^-$	42.47 ± 0.20	42.84 ± 0.37	44.94 ± 0.36	40.84 ± 0.33	5.82

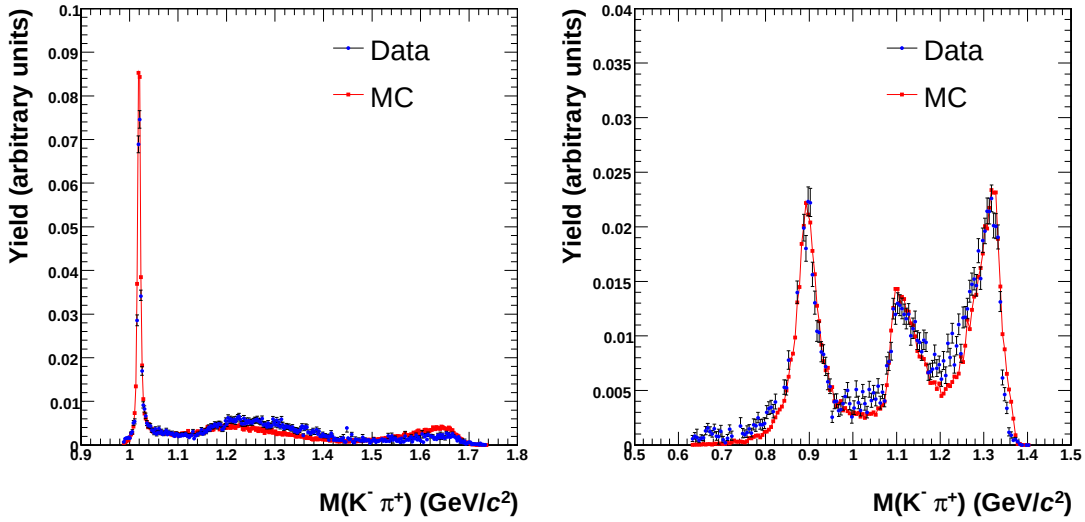

Figure 6.1: Background-subtracted mass distributions for K^-K^+ (left) and $K^-\pi^+$ (right) in $D^+ \to K^+K^-\pi^+$. Blue points are data and red points connected by lines are signal MC.

6.9.2 Track and π^0-finding Efficiencies

The track and π^0-finding efficiencies exhibit some dependence on the decay mode of the other side, as the other side contributes to charged and neutral multiplicity in the event, which in turn affects finding efficiencies. The Monte Carlo shows that there can be changes in kaon or pion reconstruction efficiencies of a few percent when comparing the extreme situations of the other side being all-neutral or being a 4-prong decay. To evaluate such discrepancy in our analysis, we re-weight events based on the generator-level number of tracks and the number of π^0's on the other side, where the weight variations are set to be three times larger than the discrepancies according to [48].

The results are shown in Table 6.8. The largest change due to the track reweighting is 0.26% in the $D^+ \to K^0_S\pi^+\pi^+\pi^-$ efficiency, and all modes show reduced efficiency when the mean track multiplicity increases, and increased ef-

Table 6.8: Effects on efficiency of reweighting the multiplicity distribution of the other side. Values are $\delta\epsilon/\epsilon$.

Mode	Track +	Track −	π^0 +	π^0 −
$D^0 \to K^-\pi^+$	−0.0004	+0.0002	+0.0005	−0.0001
$D^0 \to K^-\pi^+\pi^0$	+0.0014	−0.0013	−0.0048	+0.0041
$D^0 \to K^-\pi^+\pi^+\pi^-$	−0.0011	+0.0003	+0.0002	+0.0000
$D^+ \to K^-\pi^+\pi^+$	−0.0012	−0.0002	+0.0002	−0.0001
$D^+ \to K^-\pi^+\pi^+\pi^0$	+0.0016	−0.0012	−0.0029	+0.0027
$D^+ \to K^0_S\,\pi^+$	+0.0006	−0.0004	−0.0001	+0.0001
$D^+ \to K^0_S\,\pi^+\pi^0$	+0.0003	−0.0006	−0.0018	+0.0019
$D^+ \to K^0_S\,\pi^+\pi^+\pi^-$	−0.0026	+0.0026	+0.0004	−0.0004
$D^+ \to K^+K^-\pi^+$	+0.0025	+0.0000	+0.0000	−0.0001

ficiency when the mean decreases. Under a π^0 multiplicity shift, the only modes to show significant change are π^0 modes (which is to be expected). The largest such change is 0.48% for $D^0 \to K^-\pi^+\pi^0$. As the sizes of the multiplicity shifts are designed to be about three times larger than the observed discrepancies, so these translate to relative shifts of $O(0.2\%)$, which we choose not to include as a systematic uncertainty.

6.9.3 Multiple Candidates Rate

If there is more than one acceptable candidate for a particular D single tag decay, we choose the one with the smallest $|\Delta E|$ for the $M_{\rm BC}$ fit. As the true candidate is not guaranteed to have the smallest $|\Delta E|$, this choice is not 100% accurate. The

probability of wrong choice depends on two factors: the probability of multiple candidate rates ($\mathcal{R}$) and the probability of choosing the wrong candidate ($\mathcal{P}$). If $\mathcal{R}$ differs between data and Monte Carlo events and $\mathcal{P}$ is non-zero, then the signal efficiencies measured in Monte Carlo simulations are systematically biased.

We define F to be the fraction of the reconstructed single tag yield that originates from multiple-candidate events. We also introduce ϵ_s and ϵ_m, for signal efficiencies in single- and multiple-candidate events, respectively. The total single tag efficiency ϵ can be expressed as:

$$\frac{1}{\epsilon} = \frac{1-F}{\epsilon_s} + \frac{F}{\epsilon_m}. \tag{6.6}$$

Then we assume no data/MC discrepancies for ϵ_s and ϵ_m, and only consider the shift in efficiency between data and Monte Carlo caused by F:

$$\Delta\epsilon = \epsilon_{\rm MC} - \epsilon_{\rm data} = (F_{\rm data} - F_{\rm MC}) \times (\epsilon_s - \epsilon_m) \times \frac{\epsilon_{\rm MC}\epsilon_{\rm data}}{\epsilon_s \epsilon_m}. \tag{6.7}$$

For small F, $\epsilon \approx \epsilon_s$, so the fractional efficiency bias is

$$\frac{\Delta\epsilon}{\epsilon_{\rm MC}} \approx (F_{\rm data} - F_{\rm MC})\left(\frac{\epsilon_s}{\epsilon_m} - 1\right) = \left(\frac{F_{\rm data}}{F_{\rm MC}} - 1\right)\left(\frac{\epsilon_s}{\epsilon_{\rm MC}} - 1\right), \tag{6.8}$$

where we have used

$$\epsilon_m = \frac{F_{\rm MC}\epsilon_{\rm MC}\epsilon_s}{\epsilon_s - (1 - F_{\rm MC})\epsilon_{\rm MC}}. \tag{6.9}$$

Thus, a bias in efficiency appears only if both $F_{\rm MC} \neq F_{\rm data}$ and $\epsilon_s \neq \epsilon_m$. Since the size of bias is limited by the value of $|F_{\rm MC} - F_{\rm data}|$, we take the smaller of the central values of $|F_{\rm MC} - F_{\rm data}|$ and $|\Delta\epsilon/\epsilon_{\rm MC}|$ as the systematic uncertainty if this value is larger than than 0.2%. The results are shown in Table 6.9.

Table 6.9: The fraction of the total yield in multiple candidate events in data and Monte Carlo, the estimated efficiency change due to this effect, and the final systematic uncertainty used for this mode. The Error is taken from the smaller of the central values of $|F_{\rm MC} - F_{\rm data}|$ and $|\Delta\epsilon/\epsilon_{\rm MC}|$, if it is less than 0.2% we assign no systematic error.

Mode	$F_{\rm data}$ (%)	$F_{\rm MC}$ (%)	$F_{\rm MC} - F_{\rm data}$ (%)	$\Delta\epsilon/\epsilon_{\rm MC}$ (%)	Error (%)
$D^0 \to K^-\pi^+$	0.05 ± 0.01	0.05 ± 0.00	−0.00 ± 0.01	0.01 ± 0.03	0
$D^0 \to K^-\pi^+\pi^0$	13.97 ± 0.08	15.52 ± 0.02	1.55 ± 0.08	−0.74 ± 0.09	0.7
$D^0 \to K^-\pi^+\pi^+\pi^-$	7.25 ± 0.06	7.22 ± 0.01	−0.03 ± 0.06	0.01 ± 0.03	0
$D^+ \to K^-\pi^+\pi^+$	0.87 ± 0.02	0.76 ± 0.00	−0.10 ± 0.02	−0.04 ± 0.06	0
$D^+ \to K^-\pi^+\pi^+\pi^0$	15.05 ± 0.20	14.35 ± 0.04	−0.70 ± 0.20	0.24 ± 0.09	0.2
$D^+ \to K^0_S\pi^+$	0.99 ± 0.06	0.75 ± 0.01	−0.24 ± 0.06	−0.65 ± 2.28	0.2
$D^+ \to K^0_S\pi^+\pi^0$	12.34 ± 0.17	12.72 ± 0.03	0.38 ± 0.18	−0.09 ± 0.06	0
$D^+ \to K^0_S\pi^+\pi^+\pi^-$	17.75 ± 0.27	17.63 ± 0.05	−0.12 ± 0.27	0.06 ± 0.15	0
$D^+ \to K^+K^-\pi^+$	1.51 ± 0.11	1.50 ± 0.02	−0.01 ± 0.11	0.03 ± 0.22	0

6.10 Summary

We summarize the systematic uncertainties for each mode in Table 6.10. The "Background shape" uncertainties are applied to individual yields and efficiencies propagate to all branching fractions. Except the sources marked by asterisk in the last three row in the table, other uncertainties are correlated and coherent across all modes. To simplify the table layout, the double DCSD interference for neutral double tag is kept separately in Table 6.2.

Table 6.10: Contributions, in percent, to the uncertainty on each single tag efficiency-corrected yield, enumerated by source. The "Bkgd shape" uncertainties are applied to individual yields and efficiencies propagate to all branching fractions of the same charge via their dependence on $N_{D^0\bar{D}^0}$ or $N_{D^+D^-}$. Other uncertainties are correlated and, except for those marked by asterisks (*), are coherent across all modes.

Source	$K\pi$	$K\pi\pi^0$	$K\pi\pi\pi$	$K\pi\pi$	$K\pi\pi\pi^0$	$K^0_S\pi$	$K^0_S\pi\pi^0$	$K^0_S\pi\pi\pi$	$KK\pi$
Bkgd shape	0.38	1.10	0.76	0.40	3.05	0.77	1.53	1.22	0.82
Signal shape	0.40	0.50	0.51	0.34	0.48	0.39	0.48	0.55	0.54
Tracking	0.9	0.9	1.5	1.2	1.2	0.3	0.3	0.9	1.5
Eff - K^0_S	–	–	–	–	–	0.8	0.8	0.8	–
Eff - π^0	–	1.3	–	–	1.5	–	1.3	–	–
PID - $\pi^\pm$	0.25	0.25	0.75	0.5	0.5	0.25	0.25	0.75	0.25
PID - $K^\pm$	0.3	0.3	0.3	0.3	0.3	–	–	–	0.6
Lepton veto	0.1	–	–	–	–	–	–	–	–
FSR	0.8	0.4	0.7	0.5	0.2	0.4	0.2	0.5	0.3
$\lvert\Delta E\rvert$ (*)	0.1	0.2	0.2	0.1	0.2	0.0	0.4	1.2	0.2
Substructure (*)	–	0.58	1.3	0.53	0.94	–	0.42	0.62	5.82
Mult. cand. (*)	0	0.7	0	0	0.2	0.2	0	0	0

CHAPTER 7

RESULTS AND CONCLUSION

7.1 Branching Fractions Fits

To extract the branching fractions for the nine modes, as well as $N_{D^0\overline{D}^0}$ and $N_{D^+D^-}$, we perform a single least-squares fit that takes the measured data yields and efficiencies as input. The fitter forms a χ^2 estimator from the 18 single tag and 45 double tag modes and minimizes it while accounting for both the statistical and systematic uncertainties associated with the input measurements. In addition, the fitter corrects the yields by taking into account the background contribution for both internal and external types as we discussed in Chapter Peaking Backgrounds. The validation of the fitter with toy Monte Carlo simulations has been shown to produce unbiased results with correct error matrices [49, 50].

7.2 Generic Monte Carlo Validation

To validate the performance of the branching fraction fit, as well as our entire analysis procedure, we measure the branching fractions in generic Monte Carlo events. The χ^2 of the fit is 57.5 for 52 degrees of freedom, corresponding to a confidence level of 27.9%. The measured branching fractions and $D\overline{D}$ yields are all within 1.5 standard deviations of the input values, as shown in Table 7.1. The overall χ^2 of the difference between the fit results and the Monte Carlo inputs, accounting for the correlations among the fit parameters, is 13.6 for 11 degrees of freedom, corresponding to a confidence level of 25.7%. Since the

generic Monte Carlo sample has three times more events than our data, the statistical uncertainty in the test is smaller than we will find in data. So, we consider the agreement between measured and generated branching fractions is a confirmation of the integrity of our entire analysis procedure.

Table 7.1: Results of the fit to generic Monte Carlo. No systematic effects are included. Fractional uncertainties are given in parentheses. The agreement between the input and fitted values has an overall confidence level of 25.7%.

Parameters	Input value	Fitted value	Difference
$N_{D^0\bar{D}^0}$	9.797×10^6	$(9.754 \pm 0.056) \times 10^6$ (0.6%)	-0.8σ
$\mathcal{B}(D^0 \to K^-\pi^+)$	0.0383	0.03845 ± 0.00021 (0.6%)	$+0.7\sigma$
$\mathcal{B}(D^0 \to K^-\pi^+\pi^0)$	0.139	0.13984 ± 0.00078 (0.6%)	$+1.1\sigma$
$\mathcal{B}(D^0 \to K^-\pi^+\pi^+\pi^-)$	0.07867	0.07908 ± 0.00045 (0.6%)	$+0.9\sigma$
$N_{D^+D^-}$	7.346×10^6	$(7.410 \pm 0.043) \times 10^6$ (0.6%)	$+1.5\sigma$
$\mathcal{B}(D^+ \to K^-\pi^+\pi^+)$	0.09	0.08931 ± 0.00049 (0.6%)	-1.4σ
$\mathcal{B}(D^+ \to K^-\pi^+\pi^+\pi^0)$	0.06812	0.06811 ± 0.00044 (0.6%)	0.0σ
$\mathcal{B}(D^+ \to K^0_S\,\pi^+)$	0.01445	0.01430 ± 0.00010 (0.7%)	-1.5σ
$\mathcal{B}(D^+ \to K^0_S\,\pi^+\pi^0)$	0.05425	0.05451 ± 0.00039 (0.7%)	$+0.7\sigma$
$\mathcal{B}(D^+ \to K^0_S\,\pi^+\pi^+\pi^-)$	0.03582	0.03586 ± 0.00025 (0.7%)	$+0.2\sigma$
$\mathcal{B}(D^+ \to K^+K^-\pi^+)$	0.01493	0.01486 ± 0.00011 (0.7%)	-0.7σ

7.3 Data Results

The results of the branching fraction fit for the 818 pb^{-1} data are shown in Table 7.2, where we have listed both statistical and systematical errors. We also compute various ratios of branching fractions with respect to the two "reference"

modes as shown in Table 7.3. The χ^2 of the fit is 49.1 for 52 degrees of freedom, corresponding to a confidence level of 58.8%. The correlation matrix for the 11 fit parameters is shown in Table B.7. The residuals for the single and double tag yields are listed in Tables B.8 and B.9 respectively.

The large systematic uncertainty in the mode $D^+ \to K^+K^-\pi^+$ is mainly due to the more conservative approach we adopted when evaluating the resonant substructure uncertainties for this mode, as described in Section 6.9.1.

Table 7.2: Results of the fit to 818 pb^{-1} data. The uncertainties quoted are statistical and systematic, respectively. Fractional uncertainties are also listed in separate columns.

Parameter	Fitted value	Fractional error	
		Stat.(%)	Syst.(%)
$N_{D^0\bar{D}^0}$	$(2.986 \pm 0.014 \pm 0.061) \times 10^6$	0.5	2.1
$\mathcal{B}(D^0 \to K^-\pi^+)$	$(3.906 \pm 0.021 \pm 0.062)\%$	0.5	1.6
$\mathcal{B}(D^0 \to K^-\pi^+\pi^0)$	$(14.859 \pm 0.074 \pm 0.334)\%$	0.5	2.3
$\mathcal{B}(D^0 \to K^-\pi^+\pi^+\pi^-)$	$(8.242 \pm 0.043 \pm 0.164)\%$	0.5	2.0
$N_{D^+D^-}$	$(2.388 \pm 0.014 \pm 0.045) \times 10^6$	0.6	1.9
$\mathcal{B}(D^+ \to K^-\pi^+\pi^+)$	$(9.157 \pm 0.059 \pm 0.125)\%$	0.6	1.4
$\mathcal{B}(D^+ \to K^-\pi^+\pi^+\pi^0)$	$(6.100 \pm 0.045 \pm 0.142)\%$	0.7	2.3
$\mathcal{B}(D^+ \to K^0_S\,\pi^+)$	$(1.552 \pm 0.013 \pm 0.028)\%$	0.8	1.8
$\mathcal{B}(D^+ \to K^0_S\,\pi^+\pi^0)$	$(7.123 \pm 0.053 \pm 0.172)\%$	0.7	2.4
$\mathcal{B}(D^+ \to K^0_S\,\pi^+\pi^+\pi^-)$	$(3.012 \pm 0.027 \pm 0.076)\%$	0.9	2.5
$\mathcal{B}(D^+ \to K^+K^-\pi^+)$	$(1.019 \pm 0.011 \pm 0.061)\%$	1.0	6.0

Given the measured number of $D\overline{D}$ events and the integrated luminosity for $\psi(3770)$, i.e., $\int \mathcal{L}\,dt = 818.1 \pm 8.2$ pb^{-1} [28], we can calculate the $e^+e^- \to D\overline{D}$ cross

Table 7.3: Branching fraction ratios from the fit to 818 pb^{-1}. The uncertainties quoted are statistical and systematic, respectively.

Parameter	Fitted value	Fractional error	
		Stat.(%)	Syst.(%)
$\mathcal{B}(D^0 \to K^-\pi^+\pi^0)/\mathcal{B}(K^-\pi^+)$	$3.804 \pm 0.022 \pm 0.074$	0.6	1.9
$\mathcal{B}(D^0 \to K^-\pi^+\pi^+\pi^-)/\mathcal{B}(K^-\pi^+)$	$2.110 \pm 0.013 \pm 0.031$	0.6	1.5
$\mathcal{B}(D^+ \to K^-\pi^+\pi^+\pi^0)/\mathcal{B}(K^-\pi^+\pi^+)$	$0.666 \pm 0.006 \pm 0.014$	0.9	2.2
$\mathcal{B}(D^+ \to K^0_S\,\pi^+)/\mathcal{B}(K^-\pi^+\pi^+)$	$0.169 \pm 0.002 \pm 0.002$	1.1	1.1
$\mathcal{B}(D^+ \to K^0_S\,\pi^+\pi^0)/\mathcal{B}(K^-\pi^+\pi^+)$	$0.778 \pm 0.007 \pm 0.017$	0.9	2.2
$\mathcal{B}(D^+ \to K^0_S\,\pi^+\pi^+\pi^-)/\mathcal{B}(K^-\pi^+\pi^+)$	$0.329 \pm 0.004 \pm 0.007$	1.2	2.0
$\mathcal{B}(D^+ \to K^+K^-\pi^+)/\mathcal{B}(K^-\pi^+\pi^+)$	$0.111 \pm 0.002 \pm 0.006$	1.4	5.8

sections, as listed in Table 7.4.

Table 7.4: Production cross sections for $e^+e^- \to D\overline{D}$ and the ratio of D^+D^- to $D^0\overline{D}^0$ cross sections. The uncertainties are statistical and systematic, respectively. The charged and neutral cross sections have a correlation coefficient of 0.85 stemming from systematic uncertainties and from the common use of the luminosity measurement.

Quantity	Value
$\sigma(e^+e^- \to D^0\bar{D}^0)$	$(3.650 \pm 0.017 \pm 0.083)$ nb
$\sigma(e^+e^- \to D^+D^-)$	$(2.920 \pm 0.018 \pm 0.062)$ nb
$\sigma(e^+e^- \to D\bar{D})$	$(6.570 \pm 0.025 \pm 0.142)$ nb
$\sigma(e^+e^- \to D^+D^-)/\sigma(e^+e^- \to D^0\bar{D}^0)$	$0.800 \pm 0.006 \pm 0.008$

7.4 Conclusion

Using a sample of 818 pb^{-1} of $e^+e^- \to D\overline{D}$ data obtained with the CLEO-c detector at $E_{\rm cm}$ = 3.774 GeV, we have measured branching fractions for three hadronic D^0 decays and six D^+ decays as shown in Table 7.2. With the measured number of $D\overline{D}$ events, we also obtained cross sections as listed in Table 7.4. The comparison of the branching fractions with PDG 2004 [10] and the previous 281 pb^{-1} measurement [28] is shown in Figure 7.1.

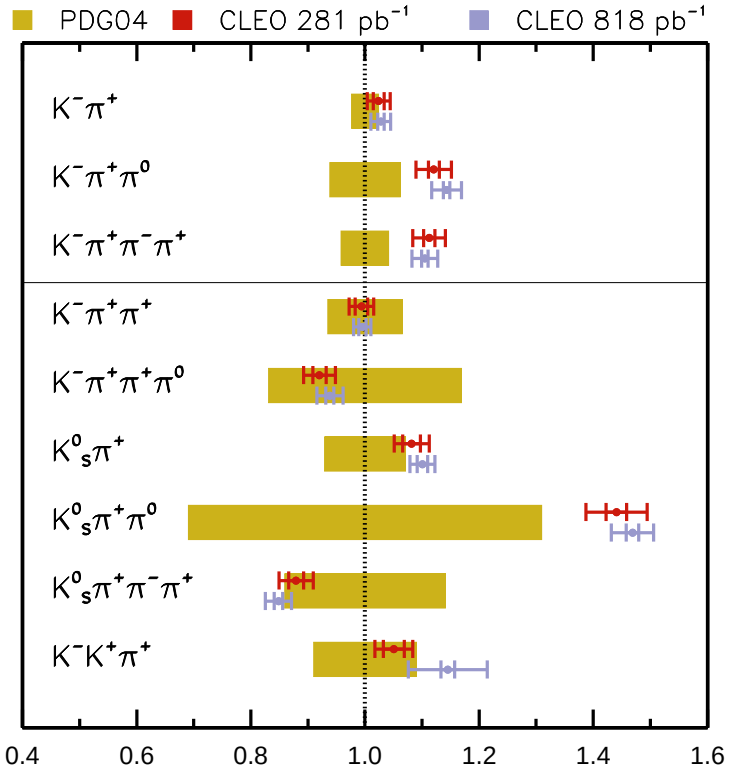

Figure 7.1: Comparison of branching fraction results with PDG 2004 [10] and previous 281 pb^{-1} measurement [28].

APPENDIX A

FIGURES

A.1 Analysis Procedure

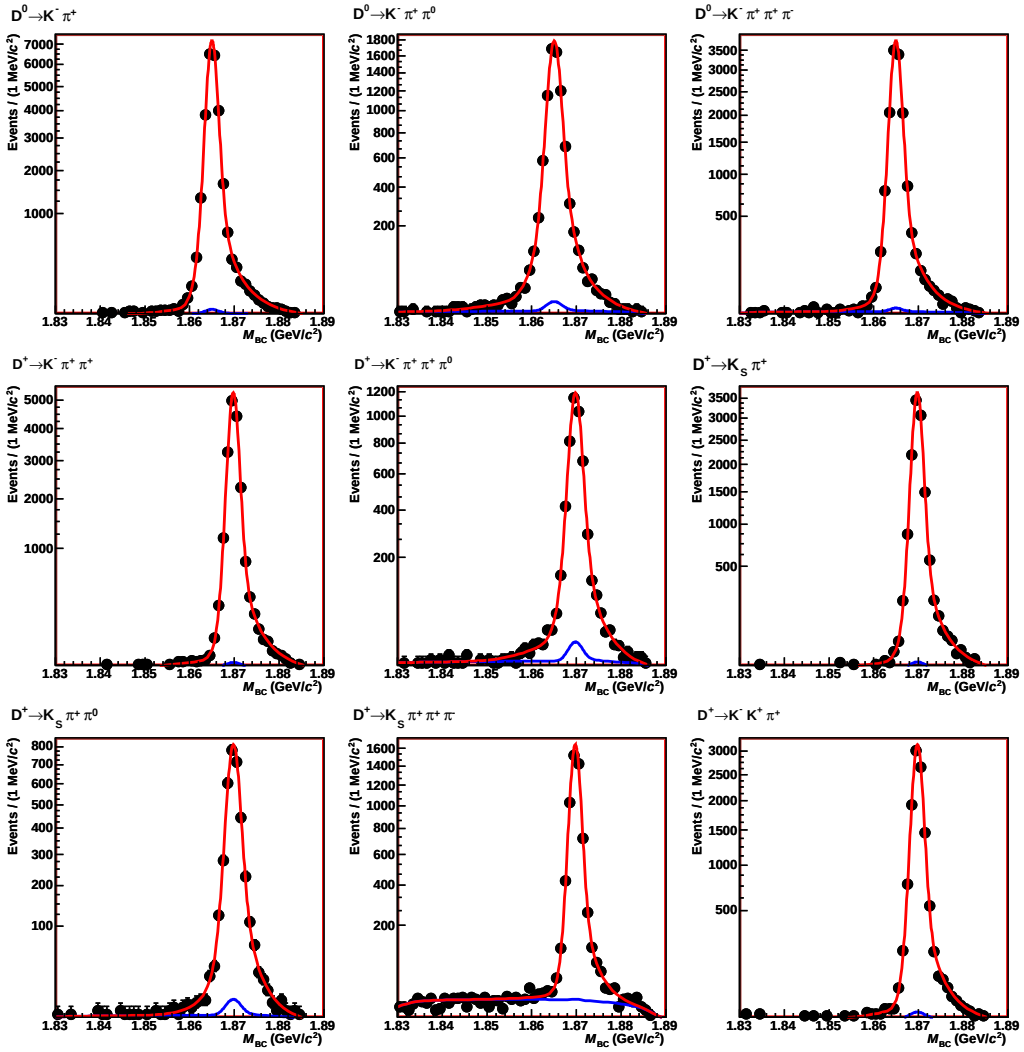

Figure A.1: Momentum resolutions fits for double tag in signal Monte Carlo with square-root scale. From top left to buttom right: $D^0 \to K^-\pi^+$, $D^0 \to K^-\pi^+\pi^0$, $D^0 \to K^-\pi^+\pi^+\pi^-$, $D^+ \to K^-\pi^+\pi^+$, $D^+ \to K^-\pi^+\pi^+\pi^0$, $D^+ \to K^0_S\,\pi^+$, $D^+ \to K^0_S\,\pi^+\pi^0$, $D^+ \to K^0_S\,\pi^+\pi^+\pi^-$, and $D^+ \to K^+K^-\pi^+$.

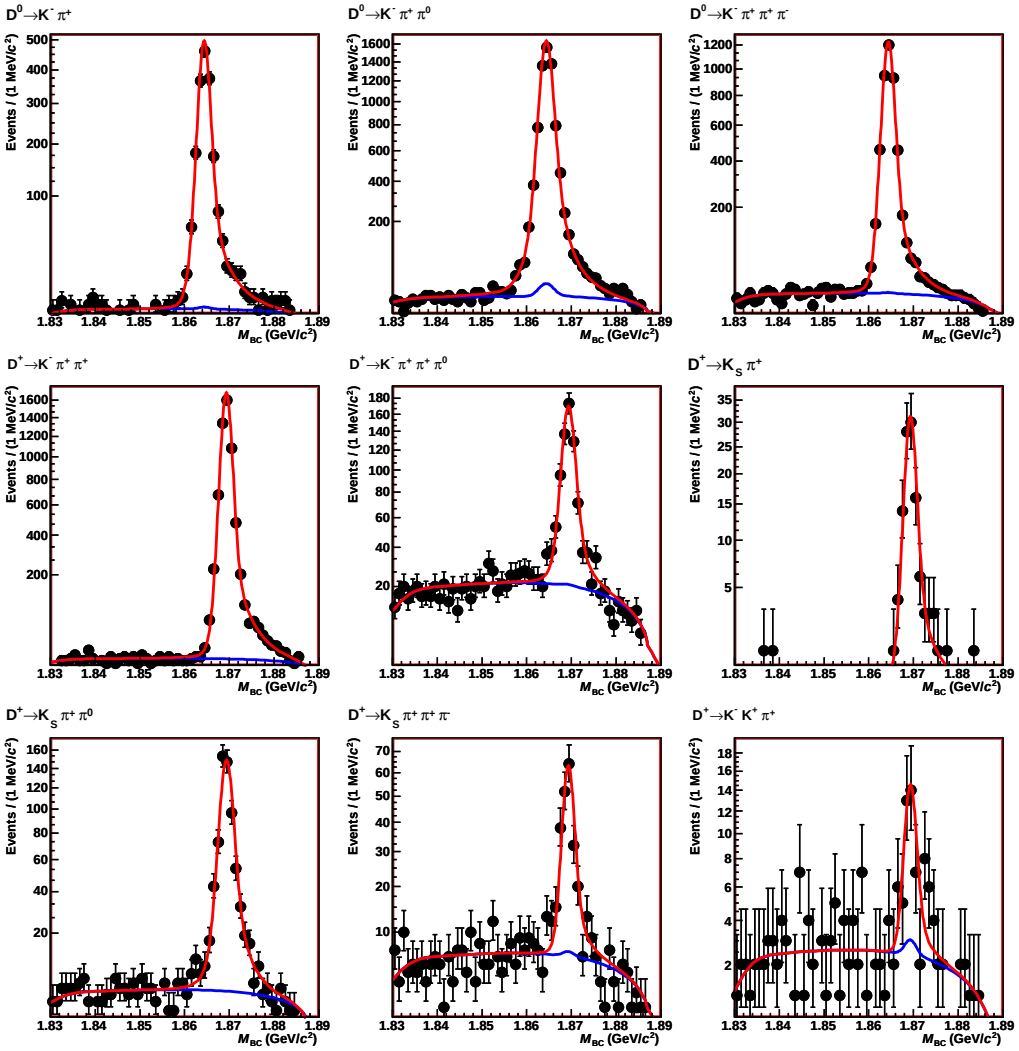

Figure A.2: Selected fits for double tags in data with square-root scale. For demonstration purpose, we only show the charge-conjugate modes here. From top left to bottom right: $D^0 \to K^-\pi^+$, $D^0 \to K^-\pi^+\pi^0$, $D^0 \to K^-\pi^+\pi^+\pi^-$, $D^+ \to K^-\pi^+\pi^+$, $D^+ \to K^-\pi^+\pi^+\pi^0$, $D^+ \to K^0_S\,\pi^+$, $D^+ \to K^0_S\,\pi^+\pi^0$, $D^+ \to K^0_S\,\pi^+\pi^+\pi^-$, and $D^+ \to K^+K^-\pi^+$.

A.2 Peaking Backgrounds

A.3 Systematic Uncertainties

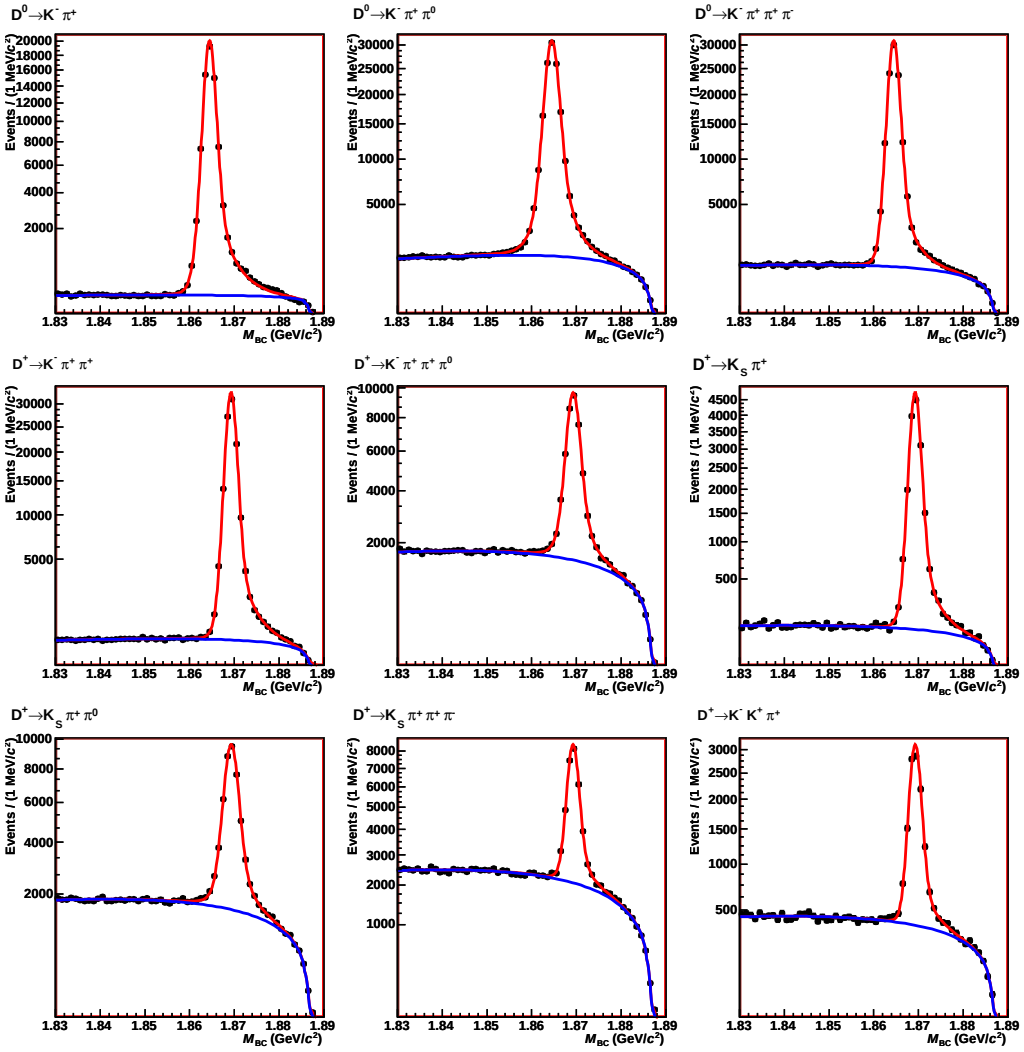

Figure A.3: Selected fits for single tag in data with square-root scale. From top left to bottom right: $D^0 \to K^-\pi^+$, $D^0 \to K^-\pi^+\pi^0$, $D^0 \to K^-\pi^+\pi^+\pi^-$, $D^+ \to K^-\pi^+\pi^+$, $D^+ \to K^-\pi^+\pi^+\pi^0$, $D^+ \to K^0_S\,\pi^+$, $D^+ \to K^0_S\,\pi^+\pi^0$, $D^+ \to K^0_S\,\pi^+\pi^+\pi^-$, and $D^+ \to K^+K^-\pi^+$.

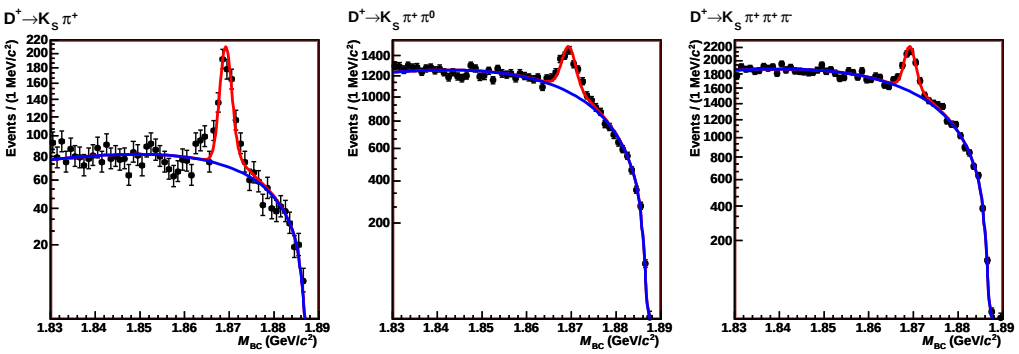

Figure A.4: $M_{\rm BC}$ fitting for K^0_S sideband in data withsquare-root scale. From left to right:$D^+ \to K^0_S\pi^+$, $D^+ \to K^0_S\pi^+\pi^0$, and $D^+ \to K^0_S\pi^+\pi^+\pi^-$. The momentum resolutions are set to the values obtained from the charge-conjugate double tag fits for these modes in data.

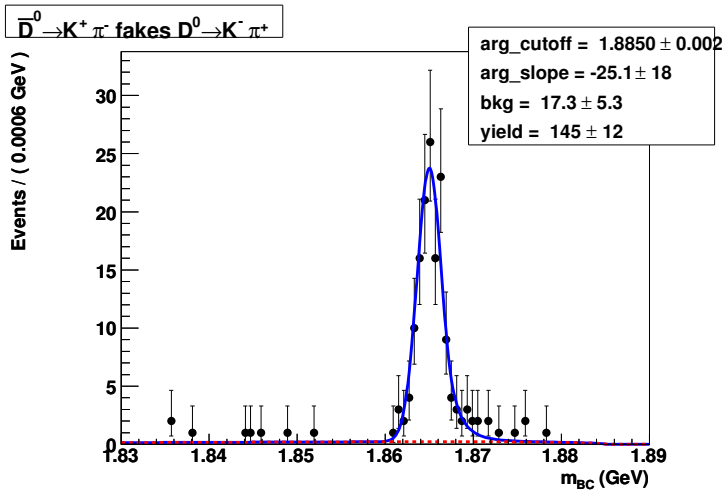

Figure A.5: $M_{\rm BC}$ fitting of particle swap background in $D^0 \to K^-\pi^+$ using signal Monte Carlo.

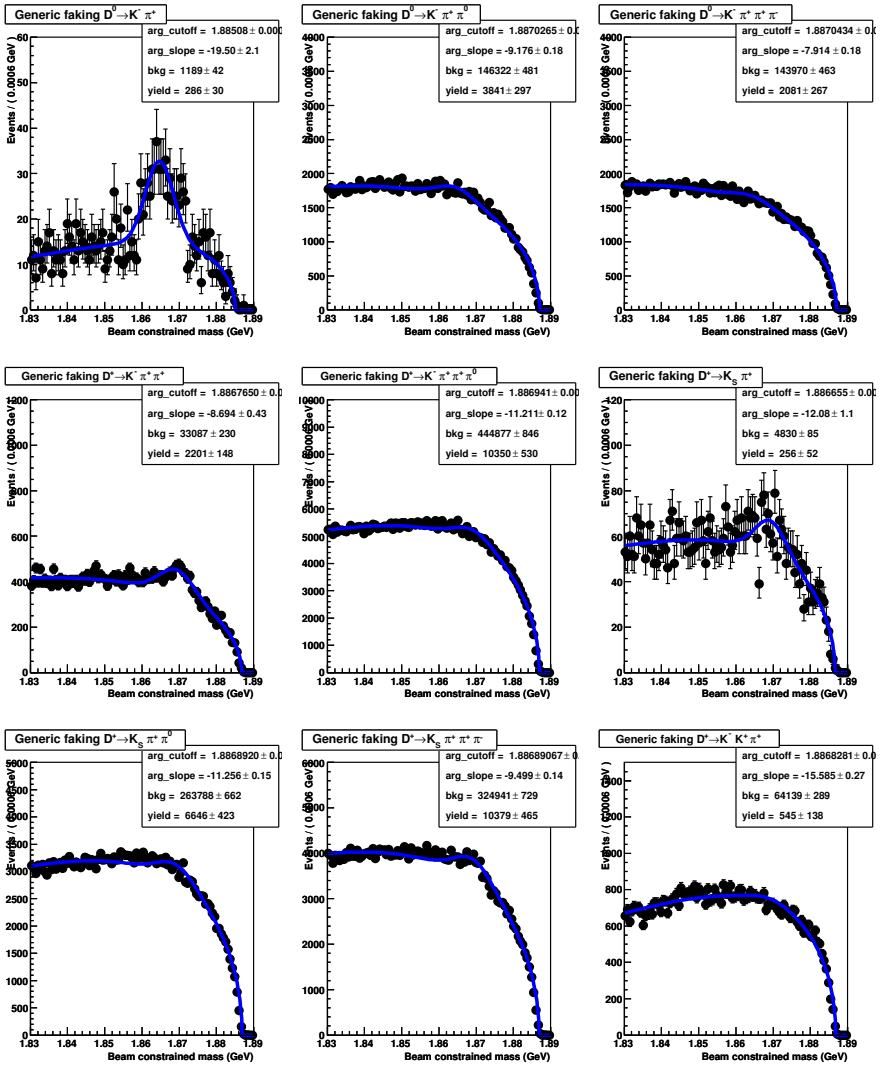

Figure A.6: $M_{\rm BC}$ spectra (in liner scale) of D candidates in generic Monte Carlo, with all of the background sources we account for are removed. The plots are fit to the sum of an ARGUS function and a Gaussian, constrained to the respective D masses and widths from the signal Monte Carlo. The largest peaking is in $D^0 \to K^-\pi^+$ where the ratio is less than 0.02%. There is no evidence of peaking background in other modes.

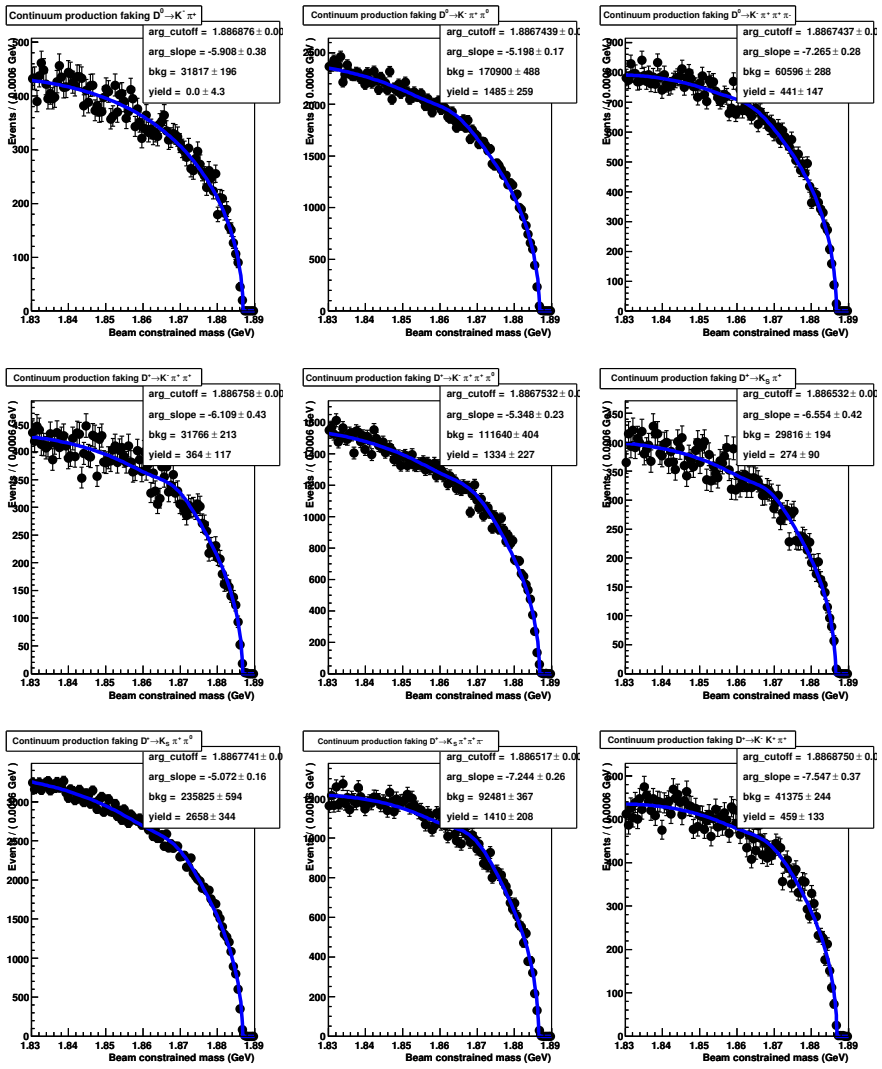

Figure A.7: $M_{\rm BC}$ spectra (in liner scale) of D candidates in continuum (non-$D\overline{D}$) Monte Carlo. The plots are fit to the sum of an ARGUS function and a Gaussian, constrained to the respective D masses and widths from the signal Monte Carlo. There is no evidence of peaking background in any of the modes.

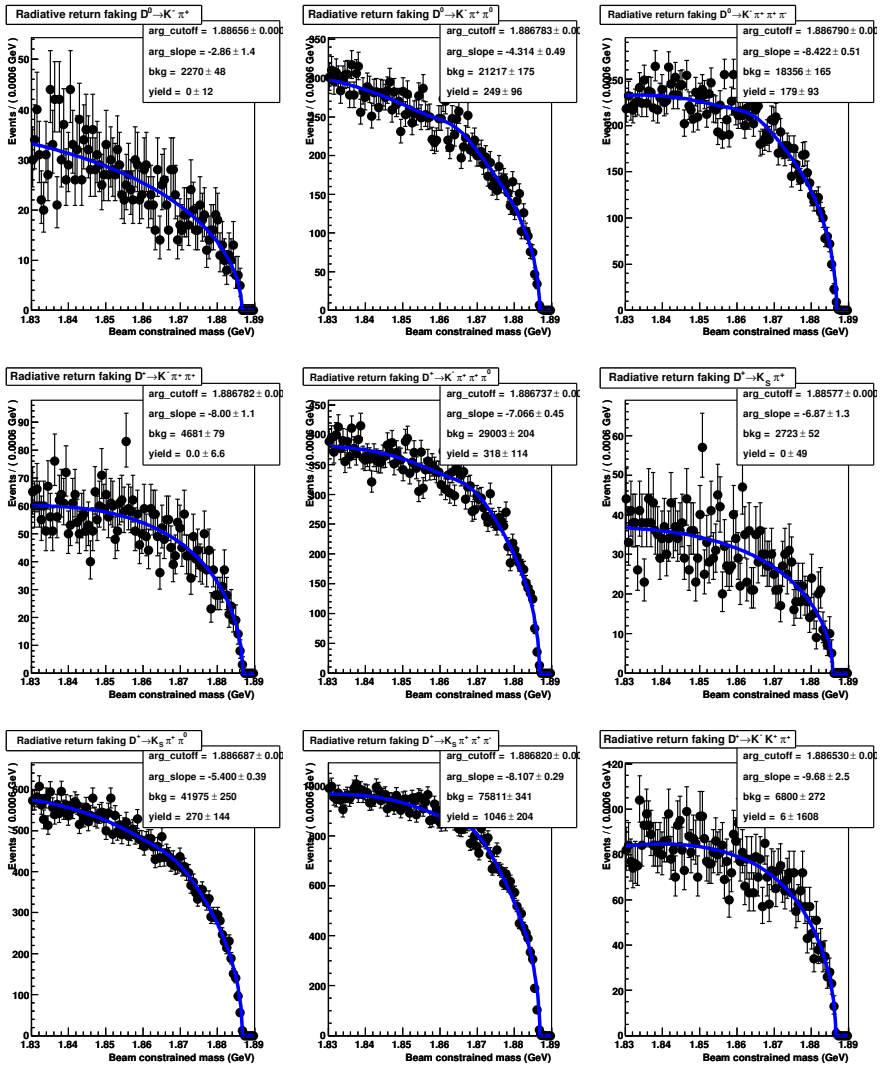

Figure A.8: $M_{\rm BC}$ spectra (in liner scale) of D candidates in radiative return Monte Carlo. The plots are fit to the sum of an ARGUS function and a Gaussian, constrained to the respective D masses and widths from the signal Monte Carlo. There is no evidence of peaking background in any of the modes.

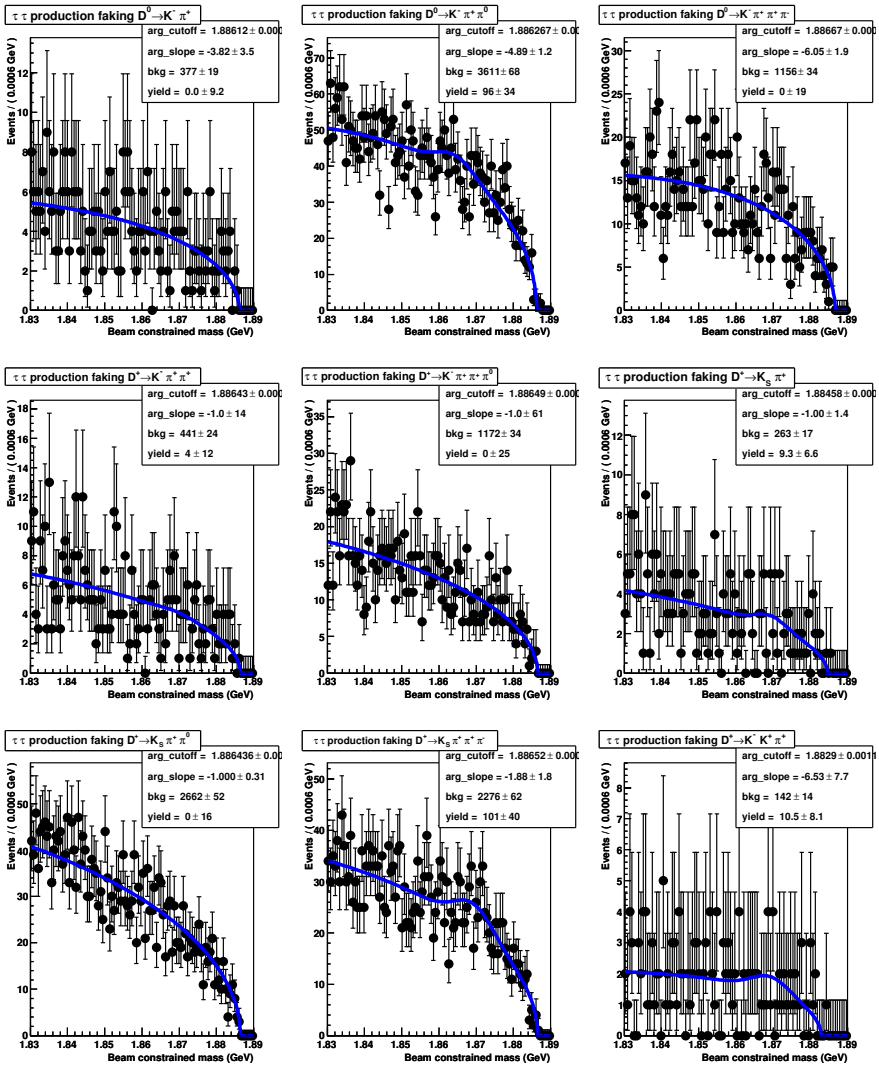

Figure A.9: $M_{\rm BC}$ spectra (in liner scale) of D candidates in τ-pair Monte Carlo. The plots are fit to the sum of an ARGUS function and a Gaussian, constrained to the respective D masses and widths from the signal Monte Carlo. There is no evidence of peaking background in any of the modes.

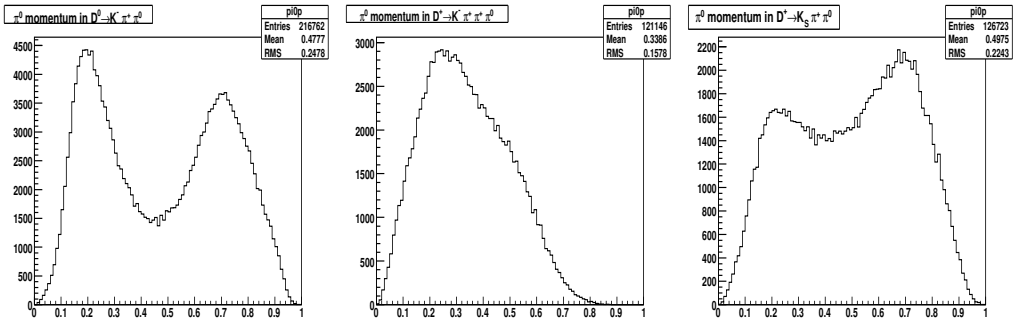

Figure A.10: π^0 momentum distribution in data. From left to right are: $D^0 \to K^-\pi^+\pi^0$, $D^+ \to K^-\pi^+\pi^+\pi^0$, and $D^+ \to K^0_S\,\pi^+\pi^0$.

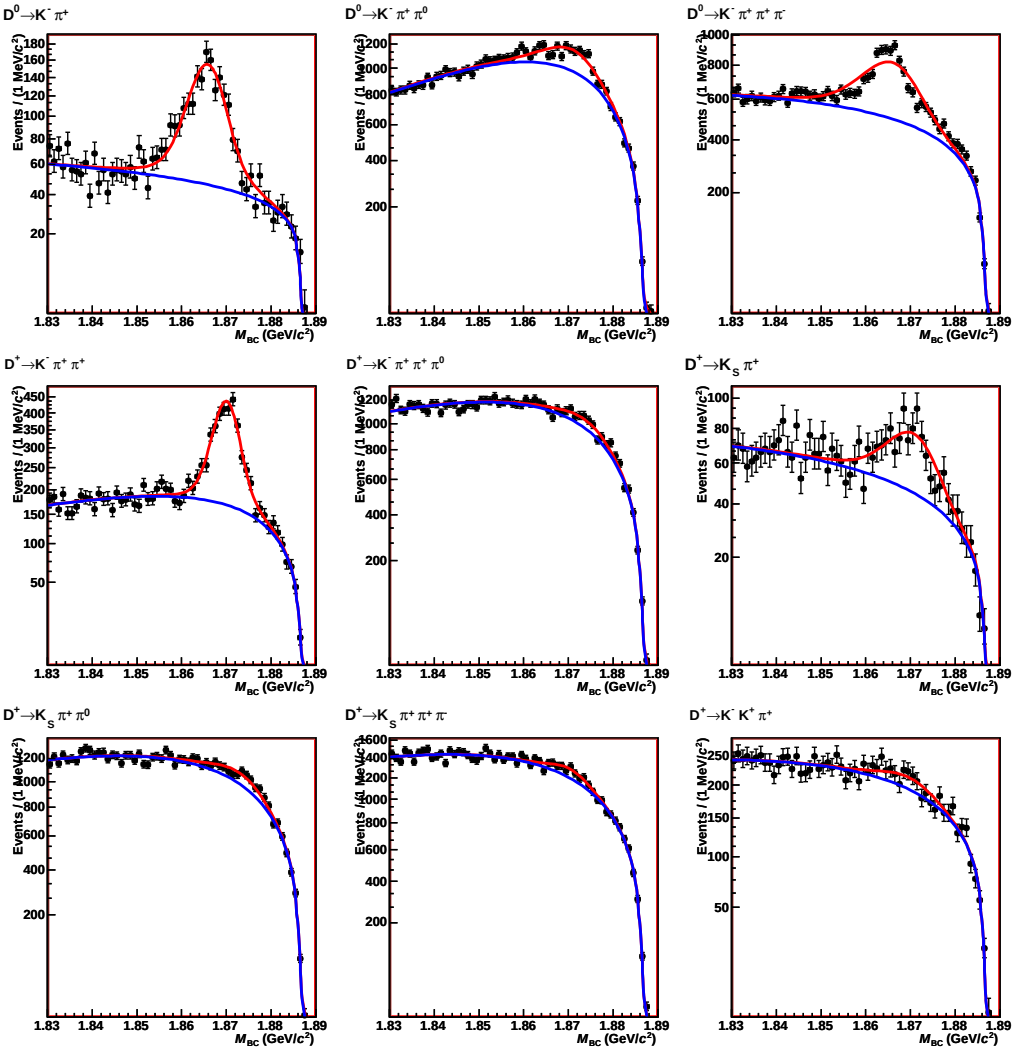

Figure A.11: Fits for low ΔE sideband single tags in data,square-root scale. From top left to bottom right: $D^0 \to K^-\pi^+$, $D^0 \to K^-\pi^+\pi^0$, $D^0 \to K^-\pi^+\pi^+\pi^-$, $D^+ \to K^-\pi^+\pi^+$, $D^+ \to K^-\pi^+\pi^+\pi^0$, $D^+ \to K^0_S\,\pi^+$, $D^+ \to K^0_S\,\pi^+\pi^0$, $D^+ \to K^0_S\,\pi^+\pi^+\pi^-$, and $D^+ \to K^+K^-\pi^+$.

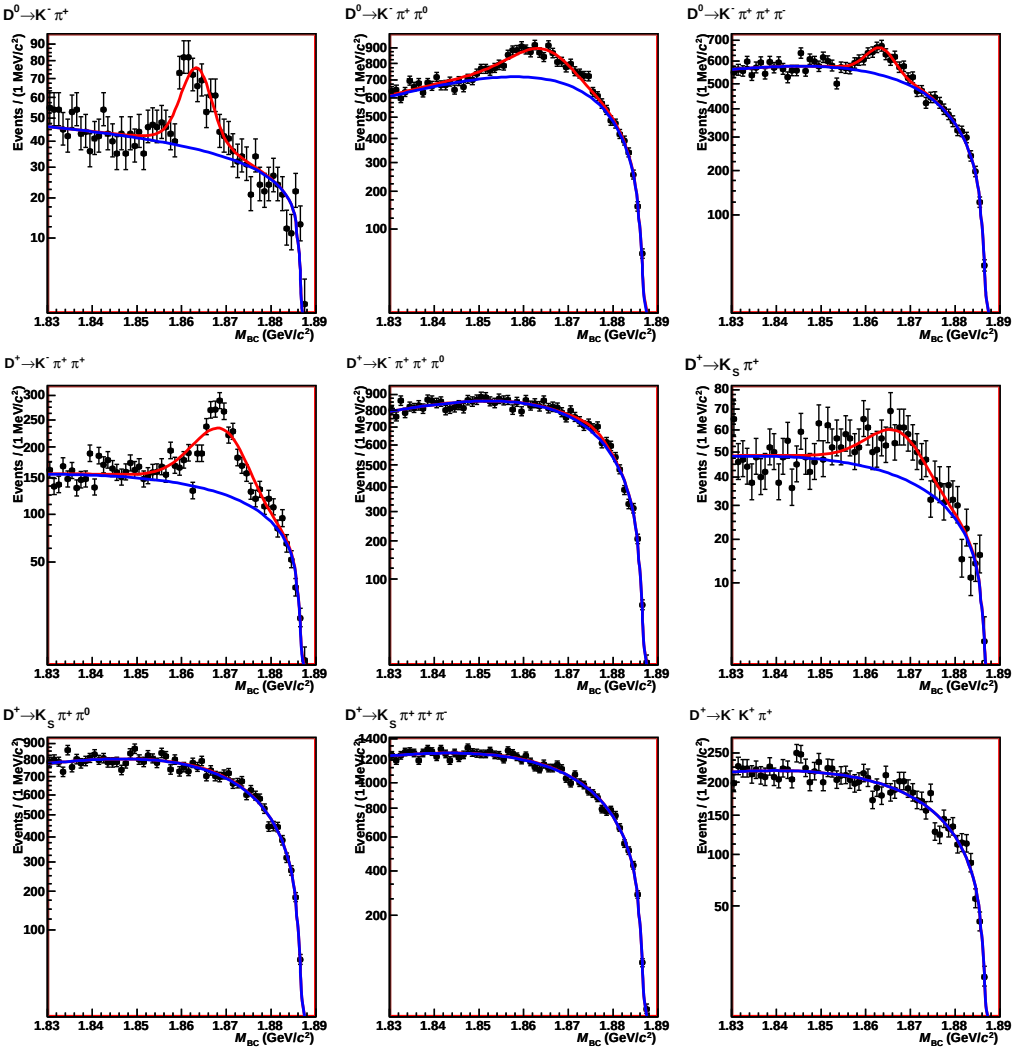

Figure A.12: Fits for high ΔE sideband single tags in data,square-root scale. From top left to bottom right: $D^0 \to K^-\pi^+$, $D^0 \to K^-\pi^+\pi^0$, $D^0 \to K^-\pi^+\pi^+\pi^-$, $D^+ \to K^-\pi^+\pi^+$, $D^+ \to K^-\pi^+\pi^+\pi^0$, $D^+ \to K^0_S\,\pi^+$, $D^+ \to K^0_S\,\pi^+\pi^0$, $D^+ \to K^0_S\,\pi^+\pi^+\pi^-$, and $D^+ \to K^+K^-\pi^+$.

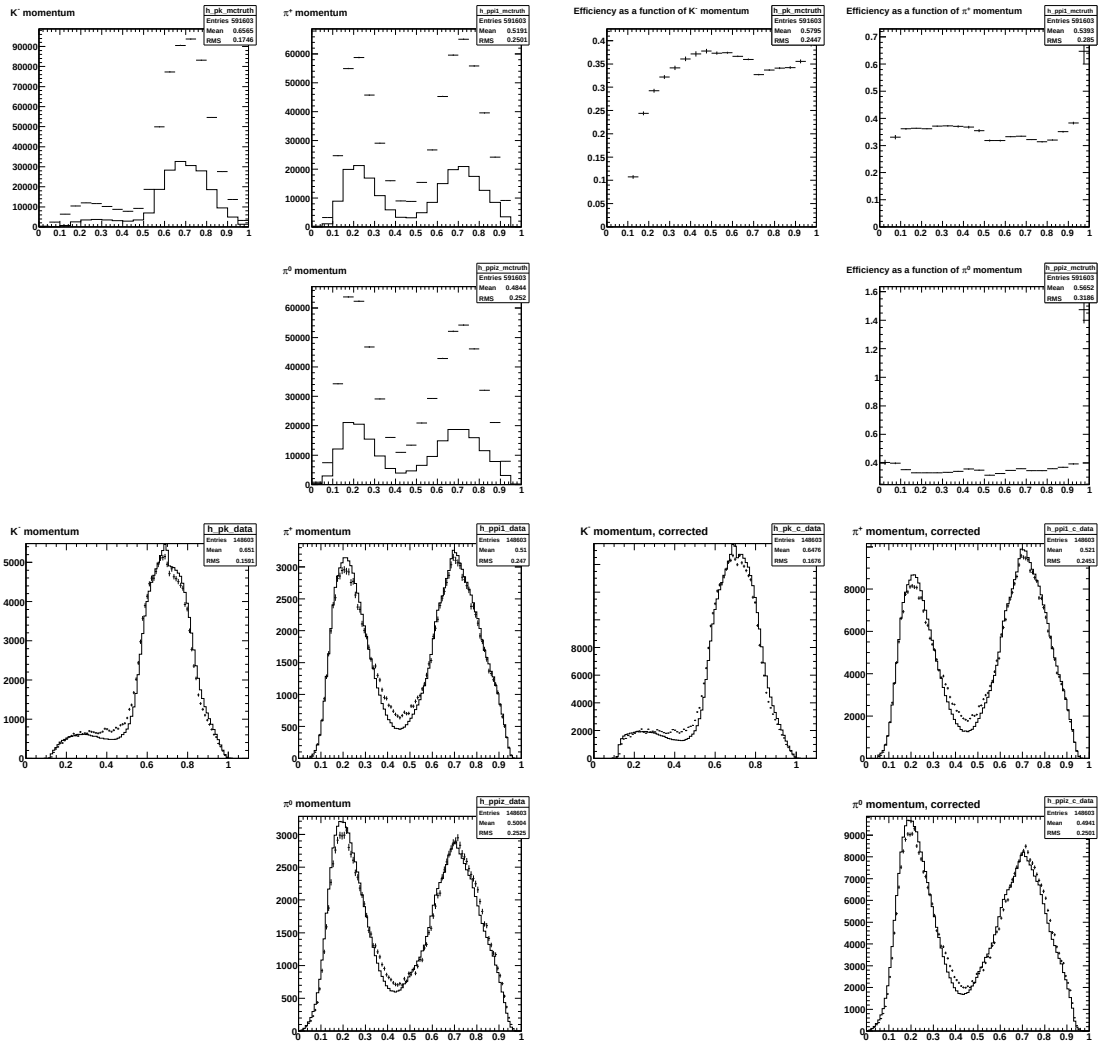

Figure A.13: Plots comparing track momentum spectra in data and MC for $D^0 \to K^-\pi^+\pi^0$. The top left three plots show the MC truth (points) and fully-reconstructed (histograms) spectra in MC. The top right three plots show the effective efficiency as a function of the momentum of each daughter particle. The bottom left three plots compare the momentum distribution for the three D^0 decay products in data (points) and MC(histograms). The bottom right three plots show the same momentum spectra after correcting bin-by-bin for efficiency.

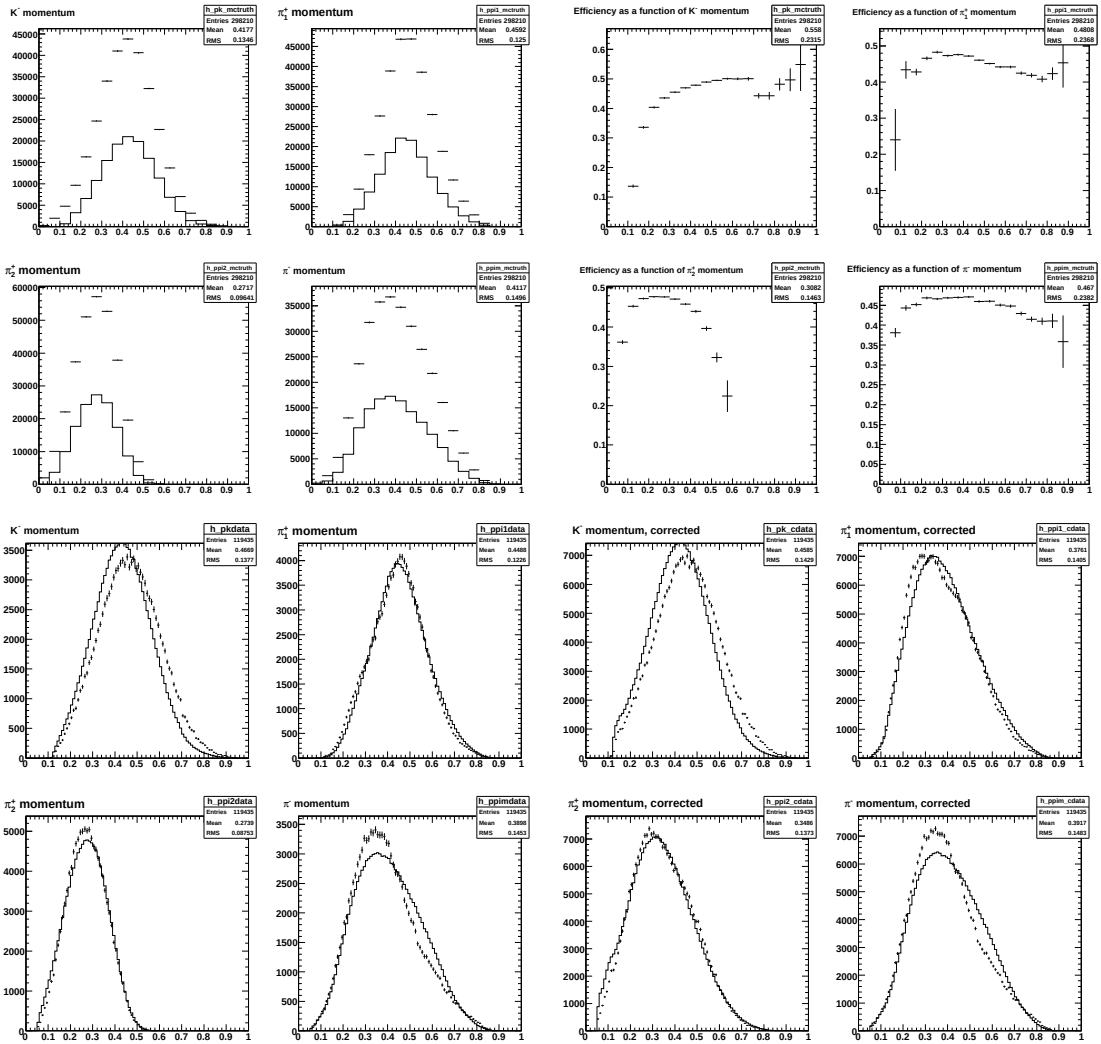

Figure A.14: Plots comparing track momentum spectra in data and MC for $D^0 \to K^-\pi^+\pi^+\pi^-$. ($\pi_1^+$ is the higher-momentum pion and π_2^+ the lower.) The top left four plots show the MC truth (points) and fully-reconstructed (histograms) spectra in MC. The top right four plots show the effective efficiency as a function of the momentum of each daughter particle. The bottom left four plots compare the momentum distribution for the four D^0 decay products in data (points) and MC(histograms). The bottom right four plots show the same momentum spectra after correcting bin-by-bin for efficiency.

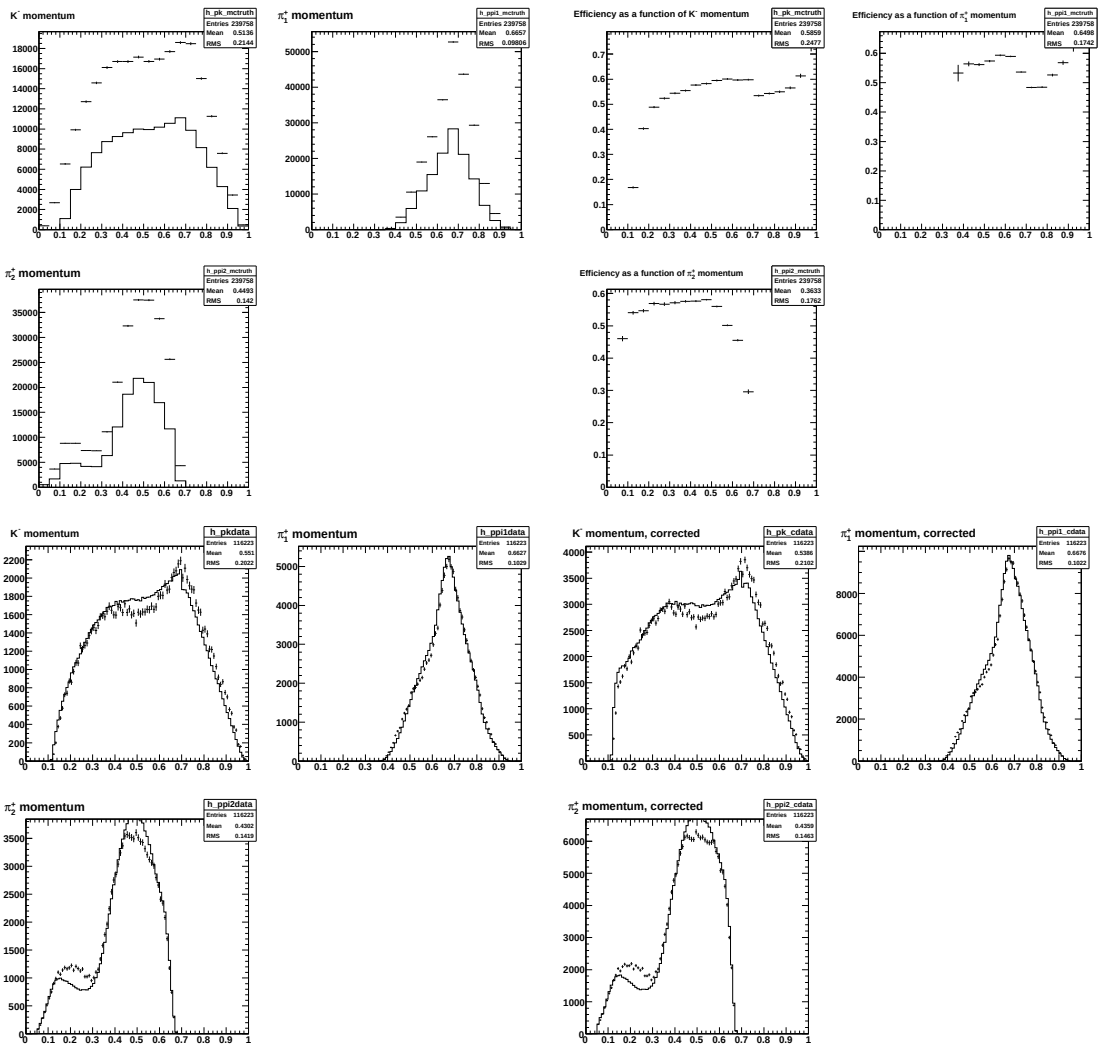

Figure A.15: Plots comparing track momentum spectra in data and MC for $D^+ \to K^-\pi^+\pi^+$. (π_1^+ is the higher-momentum pion and π_2^+ the lower.) The top left three plots show the MC truth (points) and fully-reconstructed (histograms) spectra in MC. The top right three plots show the effective efficiency as a function of the momentum of each daughter particle. The bottom left three plots compare the momentum distribution for the three D^+ decay products in data (points) and MC(histograms). The bottom right three plots show the same momentum spectra after correcting bin-by-bin for efficiency.

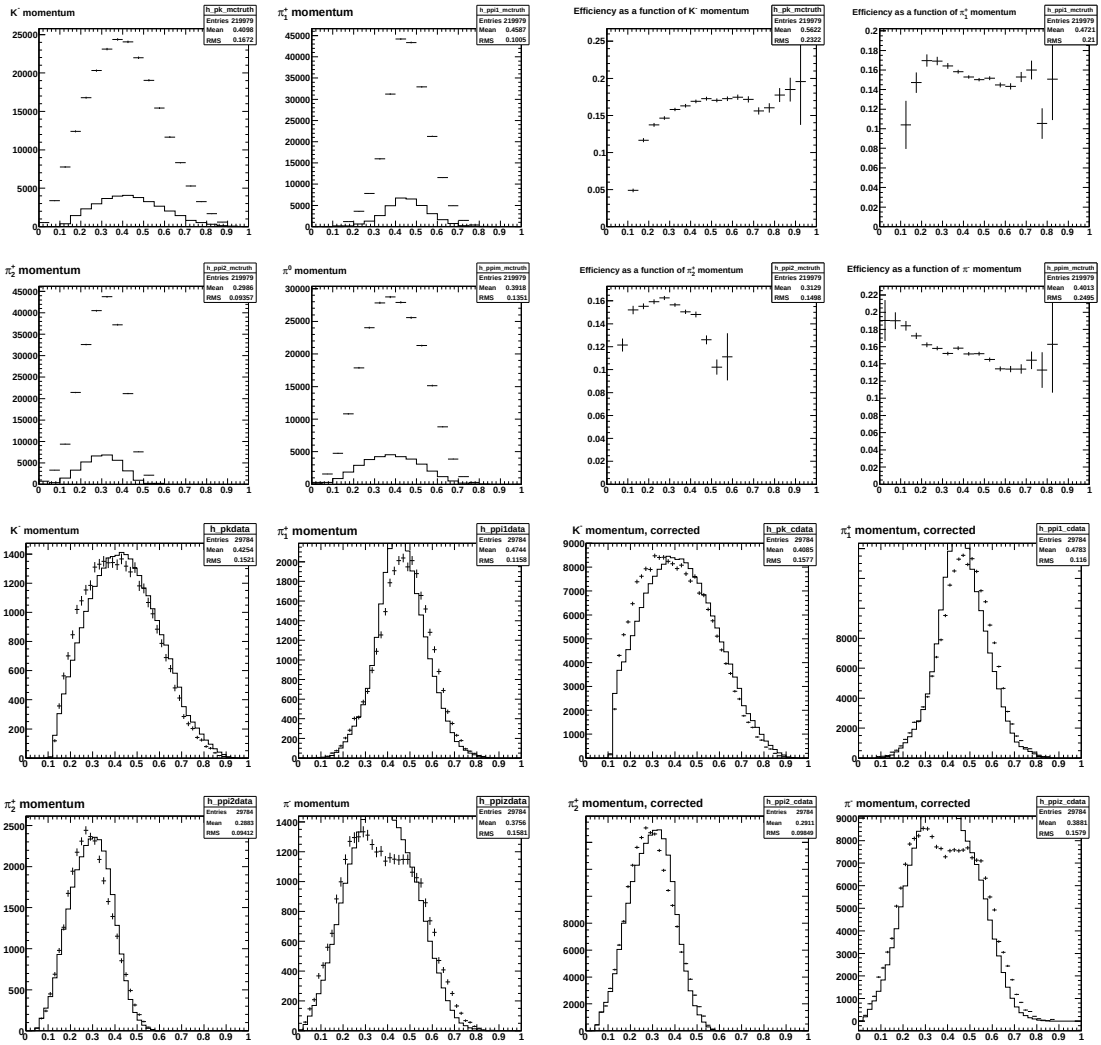

Figure A.16: Plots comparing track momentum spectra in data and MC for $D^+ \to K^-\pi^+\pi^+\pi^0$. ($\pi_1^+$ is the higher-momentum pion and π_2^+ the lower.) The top left four plots show the MC truth (points) and fully-reconstructed (histograms) spectra in MC. The top right four plots show the effective efficiency as a function of the momentum of each daughter particle. The bottom left four plots compare the momentum distribution for the four D^+ decay products in data (points) and MC(histograms). The bottom right four plots show the same momentum spectra after correcting bin-by-bin for efficiency.

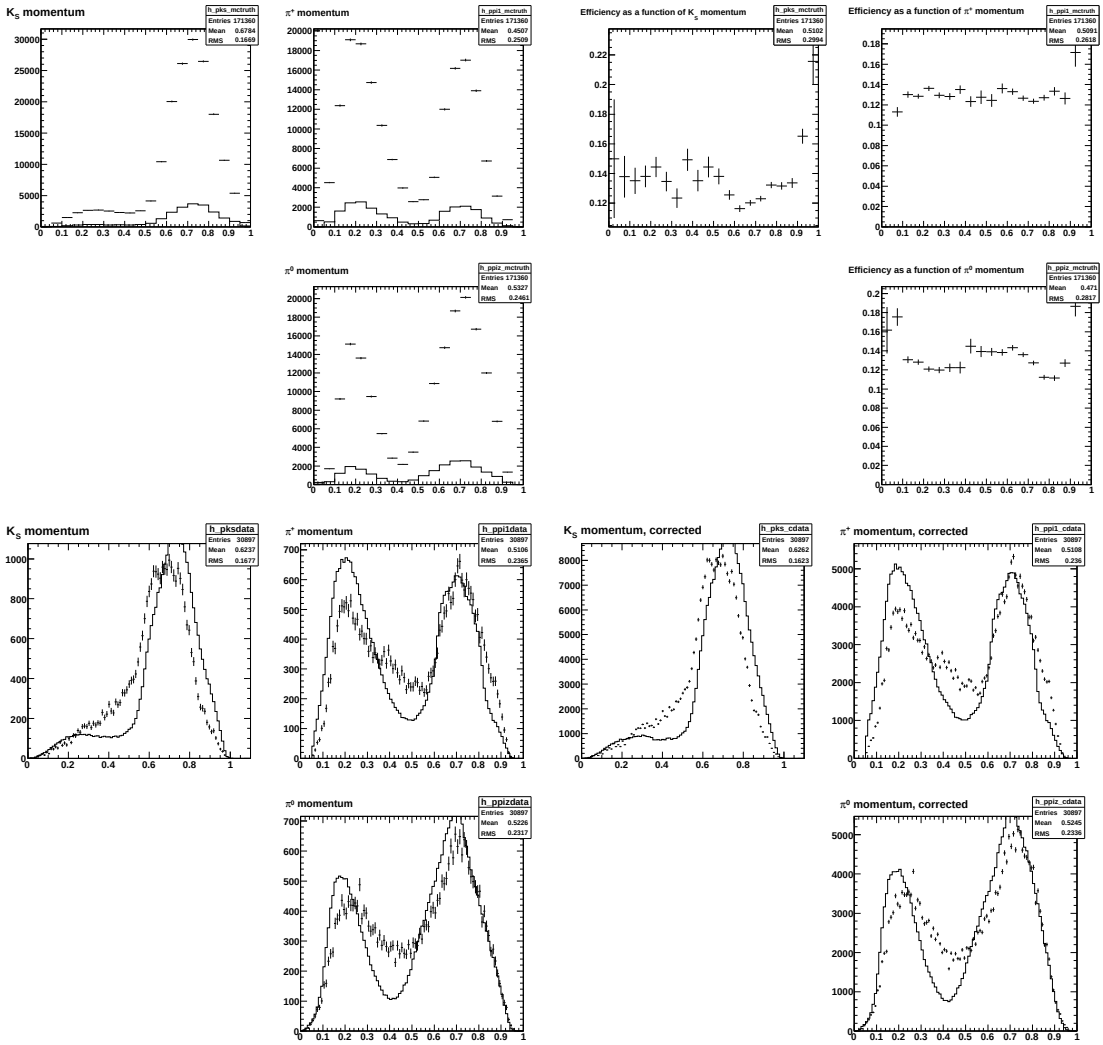

Figure A.17: Plots comparing track momentum spectra in data and MC for $D^+ \to K^0_S \pi^+ \pi^0$. The top left three plots show the MC truth (points) and fully-reconstructed (histograms) spectra in MC. The top right three plots show the effective efficiency as a function of the momentum of each daughter particle. The bottom left three plots compare the momentum distribution for the three D^+ decay products in data (points) and MC(histograms). The bottom right three plots show the same momentum spectra after correcting bin-by-bin for efficiency.

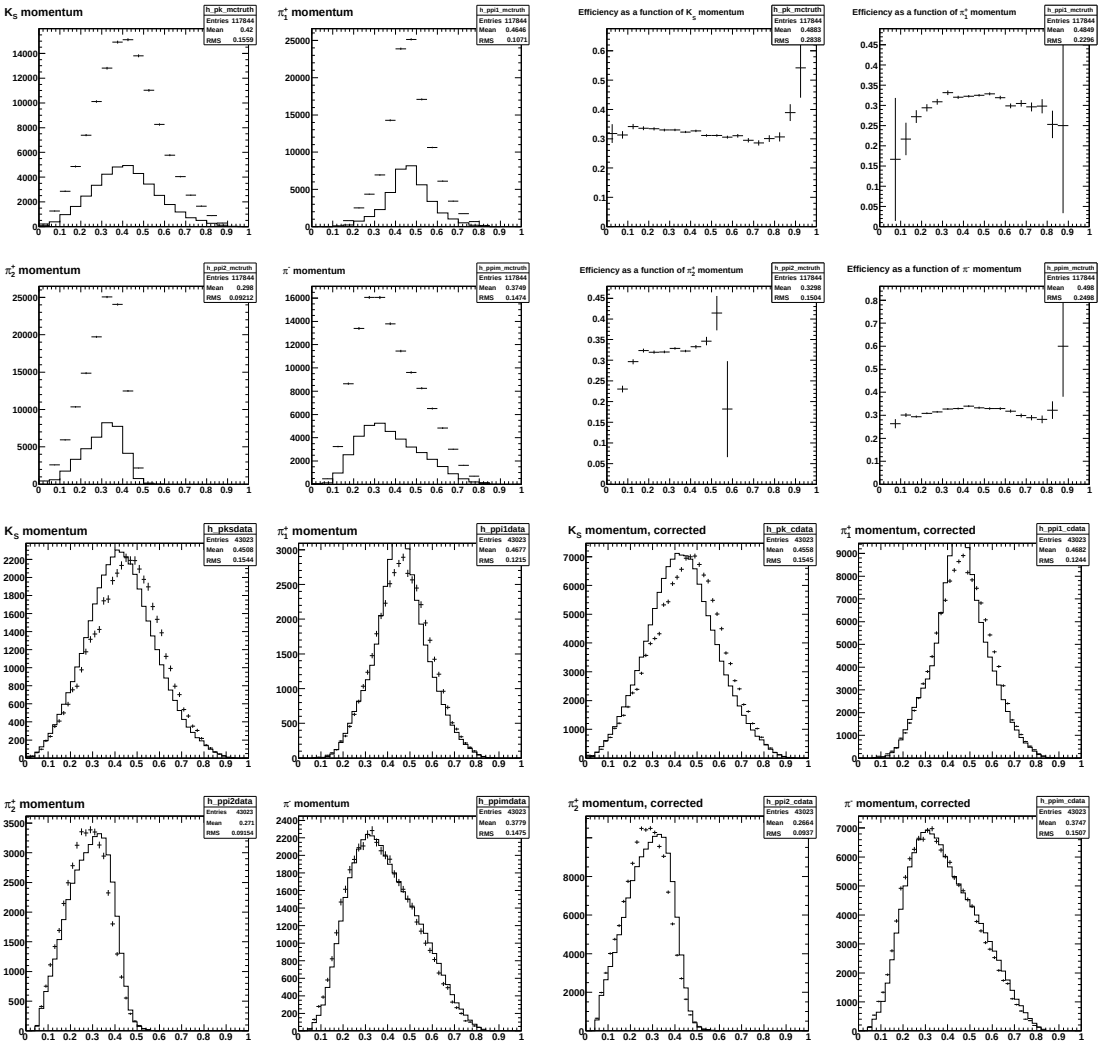

Figure A.18: Plots comparing track momentum spectra in data and MC for $D^+ \to K^0_S \pi^+ \pi^- \pi^+$. ($\pi_1^+$ is the higher-momentum pion and π_2^+ the lower.) The top left four plots show the MC truth (points) and fully-reconstructed (histograms) spectra in MC. The top right four plots show the effective efficiency as a function of the momentum of each daughter particle. The bottom left four plots compare the momentum distribution for the four D^+ decay products in data (points) and MC(histograms). The bottom right four plots show the same momentum spectra after correcting bin-by-bin for efficiency.

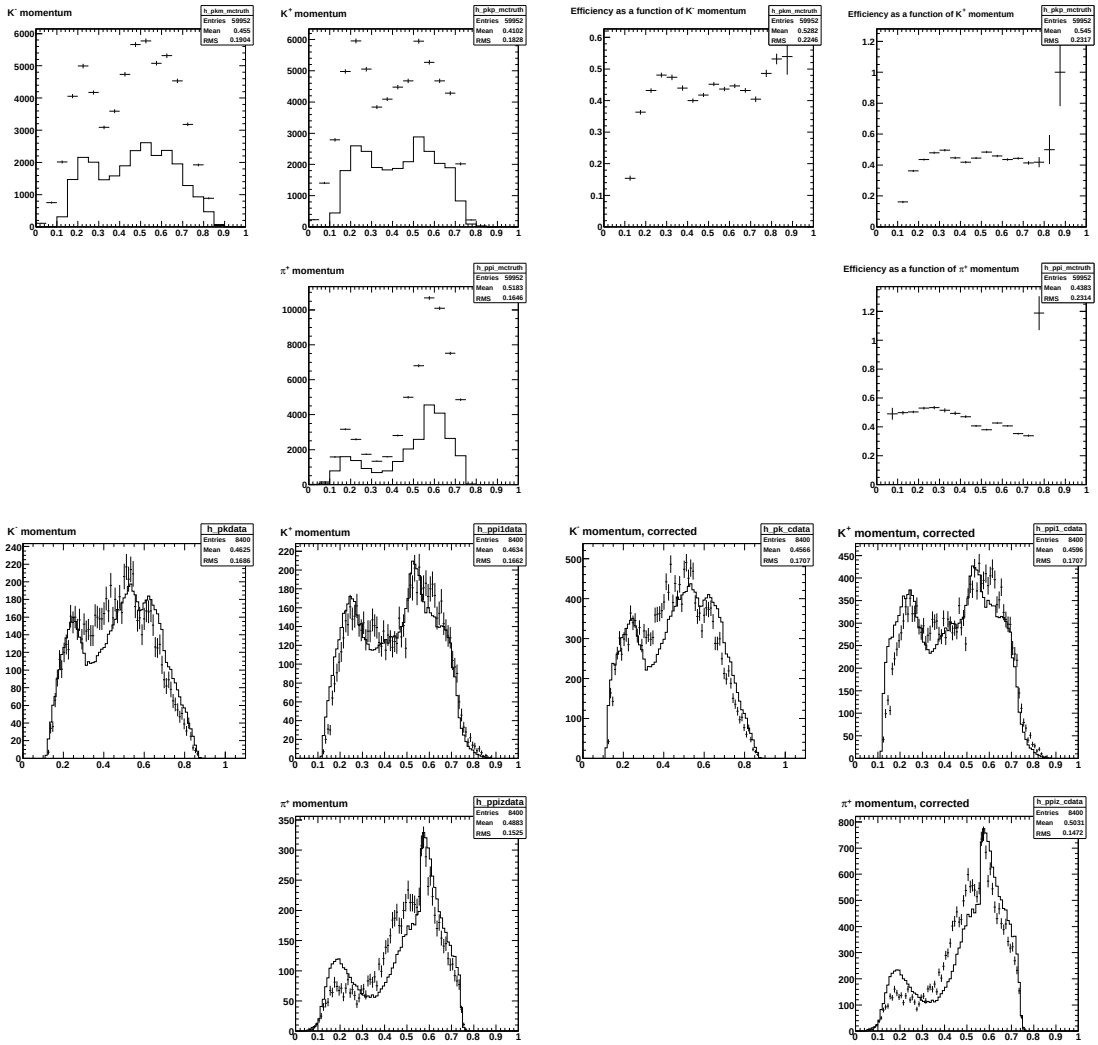

Figure A.19: Plots comparing track momentum spectra in data and MC for $D^+ \to K^+K^-\pi^+$. The top left three plots show the MC truth (points) and fully-reconstructed (histograms) spectra in MC. The top right three plots show the effective efficiency as a function of the momentum of each daughter particle. The bottom left three plots compare the momentum distribution for the three D^+ decay products in data (points) and MC(histograms). The bottom right three plots show the same momentum spectra after correcting bin-by-bin for efficiency.

APPENDIX B

TABLES

Table B.1: Single tag yields with different mass of $\psi(3770)$.

Mode	Yield			max-diff
	M = 3771.9 MeV	M = 3772.4 MeV	M = 3772.9 MeV	(%)
$D^0 \to K^-\pi^+$	75284 ± 282	75177 ± 281	75079 ± 282	0.14
$\overline{D}^0 \to K^+\pi^-$	75691 ± 283	75584 ± 282	75487 ± 282	0.14
$D^0 \to K^-\pi^+\pi^0$	144968 ± 438	144710 ± 439	144467 ± 438	0.18
$\overline{D}^0 \to K^+\pi^-\pi^0$	146064 ± 441	145798 ± 441	145548 ± 440	0.18
$D^0 \to K^-\pi^+\pi^+\pi^-$	114450 ± 366	114222 ± 366	114005 ± 366	0.20
$\overline{D}^0 \to K^+\pi^-\pi^-\pi^+$	114988 ± 367	114759 ± 368	114540 ± 367	0.20
$D^+ \to K^-\pi^+\pi^+$	116690 ± 353	116545 ± 354	116405 ± 353	−0.12
$D^- \to K^+\pi^-\pi^-$	117978 ± 355	117831 ± 356	117690 ± 356	−0.12
$D^+ \to K^-\pi^+\pi^+\pi^0$	36887 ± 258	36813 ± 260	36745 ± 260	0.20
$D^- \to K^+\pi^-\pi^-\pi^0$	37220 ± 260	37143 ± 261	37073 ± 262	0.21
$D^+ \to K^0_S\pi^+$	16870 ± 137	16844 ± 137	16820 ± 137	0.15
$D^- \to K^0_S\pi^-$	17112 ± 138	17087 ± 138	17065 ± 138	0.14
$D^+ \to K^0_S\pi^+\pi^0$	38407 ± 263	38329 ± 262	38257 ± 262	0.20
$D^- \to K^0_S\pi^-\pi^0$	38702 ± 263	38626 ± 263	38555 ± 262	0.20
$D^+ \to K^0_S\pi^+\pi^+\pi^-$	23769 ± 226	23706 ± 224	23649 ± 225	0.26
$D^- \to K^0_S\pi^-\pi^-\pi^+$	23972 ± 227	23909 ± 225	23851 ± 225	0.26
$D^+ \to K^+K^-\pi^+$	10140 ± 124	10115 ± 123	10091 ± 123	−0.24
$D^- \to K^-K^+\pi^-$	10090 ± 124	10066 ± 123	10042 ± 122	−0.24

Table B.2: Single tag yields with different width of $\psi(3770)$.

Mode	Yield			max-diff
	Γ = 22.7 MeV	Γ = 25.2 MeV	Γ = 27.2 MeV	(%)
$D^0 \to K^-\pi^+$	74908 ± 282	75177 ± 281	75412 ± 282	−0.36
$\overline{D}^0 \to K^+\pi^-$	75314 ± 282	75584 ± 282	75819 ± 283	−0.36
$D^0 \to K^-\pi^+\pi^0$	144073 ± 438	144710 ± 439	145339 ± 441	0.44
$\overline{D}^0 \to K^+\pi^-\pi^0$	145146 ± 440	145798 ± 441	146440 ± 443	−0.45
$D^0 \to K^-\pi^+\pi^+\pi^-$	113697 ± 366	114222 ± 366	114726 ± 367	−0.46
$\overline{D}^0 \to K^+\pi^-\pi^-\pi^+$	114233 ± 367	114759 ± 368	115264 ± 368	−0.46
$D^+ \to K^-\pi^+\pi^+$	116212 ± 353	116545 ± 354	116852 ± 354	−0.29
$D^- \to K^+\pi^-\pi^-$	117497 ± 355	117831 ± 356	118140 ± 356	−0.28
$D^+ \to K^-\pi^+\pi^+\pi^0$	36669 ± 259	36813 ± 260	36956 ± 261	0.39
$D^- \to K^+\pi^-\pi^-\pi^0$	36993 ± 261	37143 ± 261	37292 ± 262	−0.41
$D^+ \to K^0_S\pi^+$	16788 ± 137	16844 ± 137	16896 ± 138	−0.33
$D^- \to K^0_S\pi^-$	17034 ± 138	17087 ± 138	17137 ± 138	−0.31
$D^+ \to K^0_S\pi^+\pi^0$	38171 ± 264	38329 ± 262	38482 ± 266	−0.41
$D^- \to K^0_S\pi^-\pi^0$	38471 ± 265	38626 ± 263	38777 ± 266	−0.40
$D^+ \to K^0_S\pi^+\pi^+\pi^-$	23597 ± 224	23706 ± 224	23814 ± 226	−0.46
$D^- \to K^0_S\pi^-\pi^-\pi^+$	23798 ± 225	23909 ± 225	24018 ± 227	0.46
$D^+ \to K^+K^-\pi^+$	10069 ± 124	10115 ± 123	10160 ± 124	−0.46
$D^- \to K^-K^+\pi^-$	10020 ± 123	10066 ± 123	10109 ± 124	−0.46

Table B.3: Single tag yields with different R.

Mode	Yield			max-diff
	R = 8.7 GeV^{-1}	R = 12.7 GeV^{-1}	R = 16.7 GeV^{-1}	(%)
$D^0 \to K^-\pi^+$	75090 ± 282	75177 ± 281	75211 ± 282	−0.12
$\overline{D}^0 \to K^+\pi^-$	75497 ± 282	75584 ± 282	75618 ± 283	−0.12
$D^0 \to K^-\pi^+\pi^0$	144534 ± 438	144710 ± 439	144790 ± 439	−0.12
$\overline{D}^0 \to K^+\pi^-\pi^0$	145620 ± 440	145798 ± 441	145879 ± 441	−0.12
$D^0 \to K^-\pi^+\pi^+\pi^-$	114105 ± 366	114222 ± 366	114276 ± 366	−0.10
$\overline{D}^0 \to K^+\pi^-\pi^-\pi^+$	114643 ± 367	114759 ± 368	114812 ± 367	−0.10
$D^+ \to K^-\pi^+\pi^+$	116395 ± 353	116545 ± 354	116625 ± 354	−0.13
$D^- \to K^+\pi^-\pi^-$	117681 ± 355	117831 ± 356	117912 ± 356	−0.13
$D^+ \to K^-\pi^+\pi^+\pi^0$	36758 ± 260	36813 ± 260	36840 ± 260	−0.15
$D^- \to K^+\pi^-\pi^-\pi^0$	37086 ± 261	37143 ± 261	37172 ± 261	−0.15
$D^+ \to K^0_S\pi^+$	16821 ± 137	16844 ± 137	16856 ± 138	−0.14
$D^- \to K^0_S\pi^-$	17065 ± 138	17087 ± 138	17100 ± 138	−0.13
$D^+ \to K^0_S\pi^+\pi^0$	38271 ± 262	38329 ± 262	38358 ± 262	−0.15
$D^- \to K^0_S\pi^-\pi^0$	38568 ± 262	38626 ± 263	38655 ± 263	−0.15
$D^+ \to K^0_S\pi^+\pi^+\pi^-$	23671 ± 224	23706 ± 224	23723 ± 226	−0.15
$D^- \to K^0_S\pi^-\pi^-\pi^+$	23874 ± 224	23909 ± 225	23925 ± 226	−0.15
$D^+ \to K^+K^-\pi^+$	10100 ± 124	10115 ± 123	10122 ± 123	−0.15
$D^- \to K^-K^+\pi^-$	10050 ± 123	10066 ± 123	10072 ± 123	−0.15

Table B.4: Ratios of single tag data yields and efficiencies with the standard ΔE cuts (Yield1 and eff1) to those with $2 \times \Delta E$ cuts (Yield2 and eff2). Data/MC = (Yield1/Yield2)/(eff1/eff2).

Mode	Yield1/Yield2	eff1/eff2	Data/MC
$D^0 \to K^-\pi^+$	0.9850 ± 0.0005	0.9848 ± 0.0003	1.000 ± 0.001
$\overline{D}^0 \to K^+\pi^-$	0.9850 ± 0.0004	0.9842 ± 0.0004	1.001 ± 0.001
$D^0 \to K^-\pi^+\pi^0$	0.9879 ± 0.0003	0.9910 ± 0.0002	0.997 ± 0.000
$\overline{D}^0 \to K^+\pi^-\pi^0$	0.9896 ± 0.0003	0.9914 ± 0.0002	0.998 ± 0.000
$D^0 \to K^-\pi^+\pi^+\pi^-$	0.9759 ± 0.0005	0.9790 ± 0.0004	0.997 ± 0.001
$\overline{D}^0 \to K^+\pi^-\pi^-\pi^+$	0.9766 ± 0.0005	0.9781 ± 0.0004	0.998 ± 0.001
$D^+ \to K^-\pi^+\pi^+$	0.9783 ± 0.0004	0.9801 ± 0.0004	0.998 ± 0.001
$D^- \to K^+\pi^-\pi^-$	0.9815 ± 0.0004	0.9801 ± 0.0004	1.001 ± 0.001
$D^+ \to K^-\pi^+\pi^+\pi^0$	0.9914 ± 0.0006	0.9892 ± 0.0004	1.002 ± 0.001
$D^- \to K^+\pi^-\pi^-\pi^0$	0.9885 ± 0.0007	0.9896 ± 0.0004	0.999 ± 0.001
$D^+ \to K^0_S\,\pi^+$	0.9833 ± 0.0010	0.9833 ± 0.0004	1.000 ± 0.001
$D^- \to K^0_S\,\pi^-$	0.9782 ± 0.0012	0.9832 ± 0.0004	0.995 ± 0.001
$D^+ \to K^0_S\,\pi^+\pi^0$	0.9877 ± 0.0007	0.9841 ± 0.0006	1.004 ± 0.001
$D^- \to K^0_S\,\pi^-\pi^0$	0.9830 ± 0.0009	0.9839 ± 0.0006	0.999 ± 0.001
$D^+ \to K^0_S\,\pi^+\pi^+\pi^-$	0.9822 ± 0.0012	0.9824 ± 0.0007	1.000 ± 0.001
$D^- \to K^0_S\,\pi^-\pi^-\pi^+$	0.9911 ± 0.0009	0.9795 ± 0.0007	1.012 ± 0.001
$D^+ \to K^+K^-\pi^+$	0.9848 ± 0.0015	0.9868 ± 0.0007	0.998 ± 0.002
$D^- \to K^-K^+\pi^-$	0.9849 ± 0.0015	0.9871 ± 0.0007	0.998 ± 0.002

Table B.5: Single tag yields with fixed ARGUS parameters of $\psi(3770)$.

Mode	Yield			max-diff
	ARGUS Low	Std	ARGUS High	(%)
$D^0 \to K^-\pi^+$	75463 ± 280	75177 ± 281	75453 ± 280	0.38
$\overline{D}^0 \to K^+\pi^-$	75870 ± 280	75584 ± 282	75860 ± 280	0.38
$D^0 \to K^-\pi^+\pi^0$	143119 ± 423	144710 ± 439	144169 ± 424	−1.10
$\overline{D}^0 \to K^+\pi^-\pi^0$	144180 ± 425	145798 ± 441	145246 ± 426	−1.11
$D^0 \to K^-\pi^+\pi^+\pi^-$	115079 ± 361	114222 ± 366	114252 ± 361	0.75
$\overline{D}^0 \to K^+\pi^-\pi^-\pi^+$	115626 ± 362	114759 ± 368	114790 ± 362	0.76
$D^+ \to K^-\pi^+\pi^+$	116580 ± 350	116545 ± 354	117010 ± 350	0.40
$D^- \to K^+\pi^-\pi^-$	117867 ± 352	117831 ± 356	118306 ± 352	0.40
$D^+ \to K^-\pi^+\pi^+\pi^0$	35833 ± 242	36813 ± 260	35692 ± 242	−3.05
$D^- \to K^+\pi^-\pi^-\pi^0$	36152 ± 243	37143 ± 261	36010 ± 243	−3.05
$D^+ \to K^0_S\,\pi^+$	16973 ± 136	16844 ± 137	16862 ± 136	0.77
$D^- \to K^0_S\,\pi^-$	17212 ± 136	17087 ± 138	17105 ± 136	0.73
$D^+ \to K^0_S\,\pi^+\pi^0$	37807 ± 249	38329 ± 262	37737 ± 248	−1.54
$D^- \to K^0_S\,\pi^-\pi^0$	38105 ± 249	38626 ± 263	38035 ± 249	−1.53
$D^+ \to K^0_S\,\pi^+\pi^+\pi^-$	23439 ± 213	23706 ± 224	23415 ± 213	−1.23
$D^- \to K^0_S\,\pi^-\pi^-\pi^+$	23641 ± 214	23909 ± 225	23617 ± 214	−1.22
$D^+ \to K^+K^-\pi^+$	10198 ± 120	10115 ± 123	10145 ± 120	0.82
$D^- \to K^-K^+\pi^-$	10148 ± 120	10066 ± 123	10095 ± 120	0.81

Table B.6: Single tag efficiencies with and without FSR in signal Monte Carlo.

Mode	Eff without FSR(%)	Eff with FSR(%)	Ratio
$D^0 \to K^-\pi^+$	67.00 ± 0.12	65.17 ± 0.11	1.028 ± 0.002
$\overline{D}^0 \to K^+\pi^-$	67.89 ± 0.12	65.88 ± 0.11	1.031 ± 0.002
$D^0 \to K^-\pi^+\pi^0$	35.78 ± 0.07	35.28 ± 0.07	1.014 ± 0.001
$\overline{D}^0 \to K^+\pi^-\pi^0$	36.11 ± 0.07	35.62 ± 0.07	1.014 ± 0.001
$D^0 \to K^-\pi^+\pi^+\pi^-$	48.05 ± 0.10	46.82 ± 0.09	1.026 ± 0.001
$\overline{D}^0 \to K^+\pi^-\pi^-\pi^+$	48.39 ± 0.10	47.19 ± 0.09	1.025 ± 0.002
$D^+ \to K^-\pi^+\pi^+$	56.04 ± 0.11	54.92 ± 0.10	1.020 ± 0.001
$D^- \to K^+\pi^-\pi^-$	56.28 ± 0.11	55.17 ± 0.10	1.020 ± 0.001
$D^+ \to K^-\pi^+\pi^+\pi^0$	28.32 ± 0.11	28.13 ± 0.10	1.007 ± 0.002
$D^- \to K^+\pi^-\pi^-\pi^0$	28.46 ± 0.11	28.21 ± 0.10	1.009 ± 0.002
$D^+ \to K^0_S\pi^+$	46.39 ± 0.11	45.63 ± 0.10	1.017 ± 0.001
$D^- \to K^0_S\pi^-$	46.11 ± 0.11	45.33 ± 0.10	1.017 ± 0.001
$D^+ \to K^0_S\pi^+\pi^0$	24.07 ± 0.11	23.95 ± 0.11	1.005 ± 0.001
$D^- \to K^0_S\pi^-\pi^0$	24.25 ± 0.11	24.10 ± 0.11	1.006 ± 0.001
$D^+ \to K^0_S\pi^+\pi^+\pi^-$	32.84 ± 0.15	32.29 ± 0.14	1.017 ± 0.003
$D^- \to K^0_S\pi^-\pi^-\pi^+$	33.22 ± 0.15	32.60 ± 0.14	1.019 ± 0.003
$D^+ \to K^+K^-\pi^+$	43.25 ± 0.14	42.73 ± 0.21	1.012 ± 0.002
$D^- \to K^-K^+\pi^-$	43.03 ± 0.14	42.47 ± 0.20	1.013 ± 0.002

Table B.7: Correlation matrix for the fitted parameters including systematic uncertainties in data. The parameter order matches that in Table 7.2. The last row contains the global correlation coefficients.

1.00	−0.80	−0.49	−0.48	0.81	−0.48	−0.32	−0.60	−0.40	−0.32	−0.08
	1.00	0.52	0.65	−0.60	0.60	0.33	0.56	0.35	0.37	0.11
		1.00	0.36	−0.40	0.36	0.67	0.34	0.67	0.23	0.07
			1.00	−0.35	0.49	0.27	0.38	0.24	0.32	0.09
				1.00	−0.71	−0.38	−0.77	−0.49	−0.44	−0.14
					1.00	0.38	0.67	0.41	0.49	0.17
						1.00	0.33	0.62	0.24	0.08
							1.00	0.54	0.54	0.13
								1.00	0.36	0.08
									1.00	0.09
										1.00
0.95	0.91	0.81	0.68	0.94	0.87	0.73	0.84	0.79	0.58	0.18

Table B.8: Residuals on efficiency-corrected and background-subtracted single tag yields including systematics from the fit to data.

Mode	Residual
$D^0 \to K^-\pi^+$	-131 ± 1696
$\overline{D}^0 \to K^+\pi^-$	-783 ± 1694
$D^0 \to K^-\pi^+\pi^0$	-1218 ± 11005
$\overline{D}^0 \to K^+\pi^-\pi^0$	-2166 ± 10999
$D^0 \to K^-\pi^+\pi^+\pi^-$	-1718 ± 6209
$\overline{D}^0 \to K^+\pi^-\pi^-\pi^+$	-2484 ± 6205
$D^+ \to K^-\pi^+\pi^+$	-2177 ± 3609
$D^- \to K^+\pi^-\pi^-$	-792 ± 3611
$D^+ \to K^-\pi^+\pi^+\pi^0$	-3496 ± 5654
$D^- \to K^+\pi^-\pi^-\pi^0$	-2628 ± 5675
$D^+ \to K^0_S\,\pi^+$	-401 ± 592
$D^- \to K^0_S\,\pi^-$	381 ± 596
$D^+ \to K^0_S\,\pi^+\pi^0$	-822 ± 4626
$D^- \to K^0_S\,\pi^-\pi^0$	-505 ± 4625
$D^+ \to K^0_S\,\pi^+\pi^+\pi^-$	284 ± 2169
$D^- \to K^0_S\,\pi^-\pi^-\pi^+$	212 ± 2162
$D^+ \to K^+K^-\pi^+$	-62 ± 1527
$D^- \to K^-K^+\pi^-$	-34 ± 1527

Table B.9: Residuals on efficiency-corrected and background-subtracted double tag yields including systematics from the fit to data.

Mode	Residual
$D^0 \to K^-\pi^+\ \overline{D}^0 \to K^+\pi^-$	-34 ± 1527
$D^0 \to K^-\pi^+\ \overline{D}^0 \to K^+\pi^-\pi^0$	-159 ± 134
$D^0 \to K^-\pi^+\ \overline{D}^0 \to K^+\pi^-\pi^-\pi^+$	-47 ± 515
$D^0 \to K^-\pi^+\pi^0\ \overline{D}^0 \to K^+\pi^-$	178 ± 298
$D^0 \to K^-\pi^+\pi^0\ \overline{D}^0 \to K^+\pi^-\pi^0$	532 ± 519
$D^0 \to K^-\pi^+\pi^0\ \overline{D}^0 \to K^+\pi^-\pi^-\pi^+$	-700 ± 2786
$D^0 \to K^-\pi^+\pi^+\pi^-\ \overline{D}^0 \to K^+\pi^-$	-70 ± 1201
$D^0 \to K^-\pi^+\pi^+\pi^-\ \overline{D}^0 \to K^+\pi^-\pi^0$	-132 ± 296
$D^0 \to K^-\pi^+\pi^+\pi^-\ \overline{D}^0 \to K^+\pi^-\pi^-\pi^+$	-123 ± 1202

Continue on the next page ...

Table B.9 continued:

Mode	Residual
$D^+ \to K^-\pi^+\pi^+$ $D^- \to K^+\pi^-\pi^-$	484 ± 482
$D^+ \to K^-\pi^+\pi^+$ $D^- \to K^+\pi^-\pi^-\pi^0$	159 ± 473
$D^+ \to K^-\pi^+\pi^+$ $D^- \to K^0_S\,\pi^-$	99 ± 135
$D^+ \to K^-\pi^+\pi^+$ $D^- \to K^0_S\,\pi^-\pi^0$	932 ± 552
$D^+ \to K^-\pi^+\pi^+$ $D^- \to K^0_S\,\pi^-\pi^-\pi^+$	-280 ± 280
$D^+ \to K^-\pi^+\pi^+$ $D^- \to K^-K^+\pi^-$	-83 ± 168
$D^+ \to K^-\pi^+\pi^+\pi^0$ $D^- \to K^+\pi^-\pi^-$	-455 ± 467
$D^+ \to K^-\pi^+\pi^+\pi^0$ $D^- \to K^+\pi^-\pi^-\pi^0$	326 ± 567
$D^+ \to K^-\pi^+\pi^+\pi^0$ $D^- \to K^0_S\,\pi^-$	182 ± 158
$D^+ \to K^-\pi^+\pi^+\pi^0$ $D^- \to K^0_S\,\pi^-\pi^0$	-337 ± 612
$D^+ \to K^-\pi^+\pi^+\pi^0$ $D^- \to K^0_S\,\pi^-\pi^-\pi^+$	244 ± 311
$D^+ \to K^-\pi^+\pi^+\pi^0$ $D^- \to K^-K^+\pi^-$	-9 ± 157
$D^+ \to K^0_S\,\pi^+$ $D^- \to K^+\pi^-\pi^-$	-59 ± 132
$D^+ \to K^0_S\,\pi^+$ $D^- \to K^+\pi^-\pi^-\pi^0$	159 ± 157
$D^+ \to K^0_S\,\pi^+$ $D^- \to K^0_S\,\pi^-$	-58 ± 53
$D^+ \to K^0_S\,\pi^+$ $D^- \to K^0_S\,\pi^-\pi^0$	-127 ± 180
$D^+ \to K^0_S\,\pi^+$ $D^- \to K^0_S\,\pi^-\pi^-\pi^+$	-114 ± 95
$D^+ \to K^0_S\,\pi^+$ $D^- \to K^-K^+\pi^-$	1 ± 52
$D^+ \to K^0_S\,\pi^+\pi^0$ $D^- \to K^+\pi^-\pi^-$	-772 ± 537
$D^+ \to K^0_S\,\pi^+\pi^0$ $D^- \to K^+\pi^-\pi^-\pi^0$	502 ± 626
$D^+ \to K^0_S\,\pi^+\pi^0$ $D^- \to K^0_S\,\pi^-$	-195 ± 178
$D^+ \to K^0_S\,\pi^+\pi^0$ $D^- \to K^0_S\,\pi^-\pi^0$	394 ± 753
$D^+ \to K^0_S\,\pi^+\pi^0$ $D^- \to K^0_S\,\pi^-\pi^-\pi^+$	102 ± 363
$D^+ \to K^0_S\,\pi^+\pi^0$ $D^- \to K^-K^+\pi^-$	-226 ± 174
$D^+ \to K^0_S\,\pi^+\pi^+\pi^-$ $D^- \to K^+\pi^-\pi^-$	43 ± 281
$D^+ \to K^0_S\,\pi^+\pi^+\pi^-$ $D^- \to K^+\pi^-\pi^-\pi^0$	-309 ± 297
$D^+ \to K^0_S\,\pi^+\pi^+\pi^-$ $D^- \to K^0_S\,\pi^-$	-23 ± 98
$D^+ \to K^0_S\,\pi^+\pi^+\pi^-$ $D^- \to K^0_S\,\pi^-\pi^0$	43 ± 360
$D^+ \to K^0_S\,\pi^+\pi^+\pi^-$ $D^- \to K^0_S\,\pi^-\pi^-\pi^+$	-124 ± 200
$D^+ \to K^0_S\,\pi^+\pi^+\pi^-$ $D^- \to K^-K^+\pi^-$	-38 ± 95
$D^+ \to K^+K^-\pi^+$ $D^- \to K^+\pi^-\pi^-$	-89 ± 168
$D^+ \to K^+K^-\pi^+$ $D^- \to K^+\pi^-\pi^-\pi^0$	16 ± 153
$D^+ \to K^+K^-\pi^+$ $D^- \to K^0_S\,\pi^-$	-51 ± 49
$D^+ \to K^+K^-\pi^+$ $D^- \to K^0_S\,\pi^-\pi^0$	187 ± 189
$D^+ \to K^+K^-\pi^+$ $D^- \to K^0_S\,\pi^-\pi^-\pi^+$	-9 ± 96
$D^+ \to K^+K^-\pi^+$ $D^- \to K^-K^+\pi^-$	-9 ± 53

BIBLIOGRAPHY

[1] C. Rubbia, Rev. Mod. Phys. **57**, 699 (1985).

[2] N. Cabibbo, Phys. Rev. Lett. **10**, 531 (1963).

[3] S. L. Glashow, J. Iliopoulos, *et al.*, Phys. Rev. **D2**, 1285 (1970).

[4] J. J. Aubert, U. Becker, *et al.*, Phys. Rev. Lett. **33**, 1404 (1974).

[5] J. E. Augustin, A. M. Boyarski, *et al.*, Phys. Rev. Lett. **33**, 1406 (1974).

[6] M. Kobayashi and T. Maskawa, Prog. Theor. Phys. **49**, 652 (1973).

[7] S. W. Herb, D. C. Hom, *et al.*, Phys. Rev. Lett. **39**, 252 (1977).

[8] F. Abe and H. Akimoto (CDF Collaboration), Phys. Rev. Lett. **74**, 2626 (1995).

[9] L.-L. Chau, Physics Reports **95**, 1 (1983).

[10] S. Eidelman *et al.* (Particle Data Group), Phys. Lett. B **592**, 1 (2004).

[11] G. Goldhaber, F. M. Pierre, *et al.*, Phys. Rev. Lett. **37**, 255 (1976).

[12] I. Peruzzi, M. Piccolo, *et al.*, Phys. Rev. Lett. **37**, 569 (1976).

[13] M. Artuso, F. Azfar, *et al.* ((CLEO Collaboration)), Phys. Rev. Lett. **80**, 3193 (1998).

[14] R. Barate, D. Buskulic, *et al.*, Physics Letters B **403**, 367 (1997), ISSN 0370-2693.

[15] R. Balest, K. Cho, *et al.*, Phys. Rev. Lett. **72**, 2328 (1994).

[16] J. Adler, J. J. Becker, *et al.*, Physics Letters B **196**, 107 (1987), ISSN 0370-2693, URL http://www.sciencedirect.com/science/article/pii/0370269387916856.

[17] R. M. Baltrusaitis *et al.* (MARK-III Collaboration), Phys. Rev. Lett. **56**, 2140 (1986).

[18] J. Adler *et al.* (MARK-III Collaboration), Phys. Rev. Lett. **60**, 89 (1988).

[19] K. Berkelman, *A Personal History of Cesr and Cleo: The Cornell Electron Storage Ring and Its Main Particle Detector Facility* (World Scientific Pub Co Inc, 2004).

[20] CLEO-c/CESR-c Taskforces & CLEO-c Collaboration, Cornell LEPP preprint CLNS 01/1742 (2001), (unpublished).

[21] M. Artuso *et al.*, Nucl. Instrum. Methods A **554**, 147 (2005).

[22] Y. Kubota *et al.* (CLEO Collaboration), Nucl. Instrum. Methods A **320**, 66 (1992).

[23] K. Nakamura *et al.* (Particle Data Group), J. Phys. **G37**, 075021 (2010).

[24] W. M. Yao *et al.* (Particle Data Group), J. Phys. G **33**, 1 (2006).

[25] D. J. Lange, Nucl. Instrum. Methods A **462**, 152 (2001).

[26] R. Brun *et al.*, GEANT 3.21, CERN Program Library Long Writeup W5013 (unpublished) 1993.

[27] C. Amsler *et al.* (Particle Data Group), Phys. Lett. **B667**, 1 (2008).

[28] S. Dobbs *et al.* (CLEO), Phys. Rev. **D76**, 112001 (2007).

[29] H. Albrecht *et al.* (ARGUS Collaboration), Phys. Lett. B **241**, 278 (1990).

[30] A. Ryd, CLEO CBX **05-06** (2005).

[31] W. Verkerke and D. Kirkby (2003), for documentation and source code, see http://roofit.sourceforge.net/, arXiv:physics/0306116 [physics.data-an].

[32] I. I. Y. Bigi and H. Yamamoto, Phys. Lett. B **349**, 363 (1995).

[33] B. Aubert (BABAR Collaboration), Phys. Rev. Lett. **97**, 221803 (2006), hep-ex/0608006.

[34] P. L. Frabetti *et al.* (E687 Collaboration), Phys. Lett. B **346**, 199 (1995).

[35] Q. He *et al.* (CLEO Collaboration), Phys. Rev. Lett. **95**, 121801 (2005).

[36] D. M. Asner and W. M. Sun, Phys. Rev. D **73**, 034024 (2006).

[37] D. M. Asner and W. M. Sun, Phys. Rev. D **77**, 019901 (2008).

[38] D. M. Asner, B. Golob, *et al.*, http://www.slac.stanford.edu/xorg/hfag/charm/FPCP10/results_mix+cpv.html (14 November 2010).

[39] N. Lowrey *et al.* (CLEO Collaboration), Phys. Rev. D **80**, 031105 (2009).

[40] S. Stroiney *et al.*, CLEO CBX **2008-040** (2008).

[41] S. Stroiney *et al.*, CLEO CBX **2008-041** (2008).

[42] L. Fields and R. Patterson, CLEO CBX **2008-029** (2008).

[43] D. Cassel *et al.*, CLEO CBX **05-07** (2005).

[44] B. K. Heltsley and H. C. Mahlke, CLEO CBX **04-14** (2004).

[45] B. K. Heltsley and H. C. Mahlke, CLEO CBX **04-16** (2004).

[46] D. Asner *et al.* (Heavy Flavor Averaging Group) (2010), arXiv:1010.1589v2 [hep-ex].

[47] P. Onyisi, Ph.D. thesis, Cornell University (2008).

[48] Q. He, E. Thorndike, *et al.*, CLEO CBX **2011-002** (2005).

[49] W. M. Sun, CLEO CBX **04-36** (2004).

[50] W. M. Sun, Nucl. Instrum. Methods A **556**, 325 (2006).